Title : will be set by the publisher
Editors : will be set by the publisher
EAS Publications Series, Vol. ?, 2009

STELLAR WIND MECHANISMS AND INSTABILITIES

Stan Owocki[1]

Abstract. I review driving mechanisms for stellar winds, using first the example of the coronal, pressure-driven solar wind, but then focussing mainly on radiation-pressure driven winds from hot, luminous stars. For the latter, I review the central role of line-opacity as a coupling between matter and radiation, emphasizing how the Doppler shift of an accelerating wind outflow exposes the strong line opacity to a substantial continuum flux, and thus allows the line force to sustain the outward acceleration against gravity. Through the CAK formalism that assumes a power-law distribution of line-opacity, I derive the mass loss rate and wind velocity law, and discuss how these are altered by various refinements like a finite-disk correction, ionization variations in opacity, and a non-zero sound speed. I also discuss how multiline scattering in Wolf-Rayet (WR) winds can allow them to exceed the single scattering limit, for which the wind and radiative momenta are equal. Through a time-dependent perturbation analysis, I show how the line-driving leads to a fast, inward "Abbott-wave" mode for long wavelength perturbations, and a strong Line-Deshadowing-Instability at short wavelengths, summarizing also 1D and 2D numerical simulations of the nonlinear evolution of this instability. I next discuss how rapid stellar rotation alters the latitudinal variation of mass loss and flow speed, and how this depends on treatment of gravity darkening, nonradial line forces, and "bi-stability" shifts in ionization. Finally, I conclude with a discussion of the large mass loss epochs of Luminous Blue Variable (LBV) stars, and how these might be modeled via super-Eddington, continuum driving moderated by the "porosity" associated with extensive spatial structure.

[1] Bartol Research Institute, University of Delaware, Newark, DE 19716 USA

DOI: (will be inserted later)

Contents

1 Introduction

One of the great astronomical discoveries of the latter half of the past century was the realization that nearly all stars lose mass through a more or less continuous surface outflow called a "stellar wind". While it was long apparent that stars could eject material in dramatic outburts like novae or supernovae, the concept of continuous mass loss in the relatively quiescent phases of a star's evolution stems in large part from the direct *in situ* detection by interplanetary spacecraft of a high-speed, supersonic outflow from the sun. This was dubbed the solar "wind", in part to distinguish it from the subsonic solar "breeze" solutions which were once posited for the solar coronal expansion, and which still might have relevance for stars other than the sun. For the solar wind, the overall rate of mass loss is quite modest, roughly $10^{-14} M_\odot$/yr, which, even if maintained over the sun's entire main sequence lifetime of ca. 10^{10} year, would imply a cumulative loss of only a quite negligible 0.01% of its initial mass. By contrast, other stars – and indeed even the sun in its later evolutionary stage as a red giant – can have winds that over time substantially reduce the star's mass, with important consequences for the star's evolution and ultimate fate. More generally, the associated input of mass, momentum, and energy into the interstellar medium can have significant consequences, forming visually striking nebulae and wind blown "bubbles", and even playing a role in bursts of new star formation that can influence the overall structure and evolution of the parent galaxy. In recent years the general concept of a continuous "wind" has even been extended to describe outflows with a diverse range of conditions and scales, ranging from stellar accretion disks to whole galaxies.

This broad general importance of stellar winds motivates a need to develop a sound, physical understanding of the processes involved in wind mass loss. While there exist several reviews and even books [most notably the fine *Introduction to Stellar Winds* by Lamers and Cassinelli (1999)], my own experience is that for many students and researchers in astrophysics there still remain significant confusion and misconceptions about key physical issues, which in my view are too often shrouded by subtle mathematical arguments regarding "critical points", "regularity conditions", etc. While such mathematical discussions have their place in deriving specific wind solutions, an overall theme here is to focus more directly on the *forces* and *energies* involved. In particular, a key general issue is to identify the outward force(s) that can overcome the inward gravitational force that holds material onto a nearly hydrostatic stellar surface, and thereby lift and accelerate the outermost layers into a sustained outflow through which material ultimately escapes entirely the star's gravitational potential.

As detailed below, the specific driving mechanisms vary with the various types of stellar wind. The solar wind is often characterized as thermally or *pressure driven*, with the key outward force to overcome gravity stemming from the gas pressure gradient associated with the high-temperature solar corona. By contrast, the much stronger winds from more massive, brighter, hotter stars (spectral type O and B) are understood to be *radiation driven*, with the main outward force

arising the line scattering of the star's radiative momentum flux. These two types of winds are probably the best understood, and as such will constitute a major focus of my review here. The other important class of stellar winds from late-type stars – either in their early, pre-main-sequence phases or in their evolved, post-main-sequences as a red giant or asymptotic giant branch star – are not as well understood; partly for this reason, but also because I personally have less experience in them, these types of winds will not be discussed here.

The next section (§2) provides a general groundwork for the specific discussions of the gas-pressure-driven solar wind (§3). The following four sections focus in detail on the line-driven winds of hot-stars, beginning with the standard CAK (Castor, Abbott, KIein 1975) theory for steady, spherically symmetric outflow from OB stars(§4), followed by an extension to include multi-line scattering in the application to the much denser winds of Wolf-Rayet stars (§5), and then examining the nature and consequences of the strong, instrinsic 'line-deshadowing instability' (§6) in generating small-scale, turbulent structure. We then (§7) examine the effect of stellar rotation on the latitudinal distribution of line-driven mass loss. We conclude (§8) with a discussion of the Eddington limit, including recent ideas about instabilities that can occur when a star approaches or exceeds this limit, and how this can lead to a strong continuum-driven mass loss applicable to the Luminous Blue Variables phase of massive star evolution.

2 General Equations and Formalism for Stellar Wind Mass Loss

2.1 Hydrostatic Equilibrium in the Atmospheric Base of any Wind

A stellar wind outflow draws mass from the large reservoir of the star at its base. In the star's atmosphere the mass density ρ becomes so high that the net mass flux density ρv for the overlying steady wind requires only a very slow net drift speed v, much below the local sound speed a. In this nearly static region, the gravitational acceleration $\mathbf{g}_{grav}$ acting on the mass density ρ is closely balanced by a pressure gradient ∇P,

$$\nabla P = \rho \mathbf{g}_{grav} \,, \tag{2.1}$$

a condition known as *hydrostatic equilibrium*. In luminous stars, this pressure can include significant contributions from the stellar radiation, but for now let us assume (as is applicable for the sun and other cool stars) it is set by the ideal gas law

$$P = \rho k T/\mu = \rho a^2 \,. \tag{2.2}$$

The latter equality introduces the isothermal sound speed, defined by $a \equiv \sqrt{kT/\mu}$, with T the temperature, μ the mean atomic weight, and k Boltmann's constant.

From eqns. (2.1) and (2.2), let us next identify the characteristic pressure scale height

$$H \equiv \frac{P}{|\nabla P|} = \frac{a^2}{|g_{grav}|} \,. \tag{2.3}$$

In the simple ideal case of an isothermal atmosphere with constant sound speed a, this represents the scale for exponential stratification of density and pressure with height z

$$\frac{P(z)}{P_*} = \frac{\rho(z)}{\rho_*} = e^{-z/H} \,, \tag{2.4}$$

where the asterisk subscripts denote values at some reference height at the stellar surface. In practice the temperature variations in an atmosphere are gradual enough that quite generally both pressure and density very nearly follow such an exponential stratification.

As a typical example, in the solar photosphere $T \approx 6000$ K and $\mu \approx 10^{-24}$ g, yielding a sound speed $a \approx 9$ km/s. For the solar surface gravity $g_{grav} = GM_\odot/R_\odot^2 \approx 2.7 \times 10^4\ cm/s^2$, this gives a pressure scale height of $H \approx 300$ km, which is very much less than the solar radius $R_\odot \approx 700,000$ km. This implies a sharp edge to the visible solar photosphere, with the emergent spectrum well described by a planar atmospheric model fixed by just two parameters – typically effective temperature and gravity– and not dependent on the actual solar radius.

This relative smallness of the atmospheric scale height is a key general characteristic of static stellar atmospheres, common to all but the most extremely extended giant stars. In general, for stars with mass M_*, radius R_* and surface temperature T_*, the ratio of scale height to radius can be written in terms of the

ratio of the associated sound speed a_* to surface escape speed $v_{esc} \equiv \sqrt{2GM_*/R_*}$,

$$\frac{H_*}{R_*} = \frac{2a_*^2}{v_{esc}^2} \equiv 2s_* \,. \tag{2.5}$$

One recurring theme of this review is that the value of this ratio is also of direct relevance to stellar winds. The parameter $s_* \equiv (a_*/v_{esc})^2$ characterizes roughly (i.e. within an order unity factor 3) the ratio between the gas internal energy and the gravitational escape energy. For the solar photosphere, $s_* \approx 2.2 \times 10^{-4}$, and even for very hot stars with an order of magnitude higher photospheric temperature, this parameter is still quite small, $s_* \sim 10^{-3}$.

As discussed further in §3, for the multi-million-degree temperature of the solar corona, this parameter is much closer to unity, and that is a key factor in the capacity for the thermal gas pressure to drive the outward coronal expansion that is the solar wind. But as a prelude to considering the specific details of this solar coronal expansion, let us first establish the general equations governing a generic stellar wind.

2.2 General Flow Conservation Equations

To generalize from hydrostatic balance, let us now consider a case wherein the vector sum of volume forces acting on a fluid is not zero, and thus leads via Newton's Second Law to a net acceleration

$$\frac{d\mathbf{v}}{dt} = \frac{\partial \mathbf{v}}{\partial t} + \mathbf{v} \cdot \nabla \mathbf{v} = -\frac{\nabla P}{\rho} - \frac{GM_*}{r^2}\hat{\mathbf{r}} + \mathbf{g}_x \,. \tag{2.6}$$

Here $\mathbf{v}$ is the flow velocity, $\mathbf{g}_x$ is some, yet-unspecified force-per-unit-mass, and we've now written the gravity in terms of its standard dependence on gravitation constant G, stellar mass M_*, and radius r, with $\hat{\mathbf{r}}$ a unit radial vector.

The density and velocity are related through the mass conservation relation

$$\frac{\partial \rho}{\partial t} + \nabla \cdot \rho \mathbf{v} = 0 \,. \tag{2.7}$$

Conservation of energy takes the form

$$\frac{\partial e}{\partial t} + \nabla \cdot e\mathbf{v} = -P\,\nabla \cdot \mathbf{v} - \nabla \cdot \mathbf{F}_c + Q_x \,, \tag{2.8}$$

where for an ideal gas with ratio of specific heats γ, the internal energy e is related to the pressure through

$$P = \rho a^2 = (\gamma - 1)e \,. \tag{2.9}$$

On the right-hand-side of eqn. (2.8), Q_x represents some still unspecified, net volumetric heating or cooling, while $\mathbf{F}_c$ is the conductive heat flux density, taken classically to depend on the temperature as

$$\mathbf{F}_c = K_o T^{5/2}\,\nabla T \,, \tag{2.10}$$

where for electron conduction the coefficient $K_o = 5.6 \times 10^{-7}\, erg/s/cm/K^{7/2}$ (Spitzer 1962).

Collectively, eqns. (2.6)-(2.9) represent the general equations for a potentially time-dependent, multi-dimensional flow.

2.3 Steady, Spherically Symmetric Wind Expansion

In application to stellar winds, first-order models are commonly based on the simplifying approximations of steady-state ($\partial/\partial t = 0$), spherically symmetric, radial outflow ($\mathbf{v} = v\hat{r}$). The mass conservation requirement (2.7) then can then be used to define a constant overall mass loss rate

$$\dot{M} \equiv 4\pi\rho v r^2 \,. \tag{2.11}$$

Using this and the ideal gas law to eliminate the density in the pressure gradient term then gives for the radial equation of motion

$$\left(1 - \frac{a^2}{v^2}\right) v \frac{dv}{dr} = -\frac{GM_*}{r^2} + \frac{2a^2}{r} + \frac{da^2}{dr} + g_x \tag{2.12}$$

In general, evaluation of the sound speed terms requires simultaneous solution of the corresponding, steady-state form for the flow energy, eqn. (2.8), using also the equation of state eqn. (2.9). But in practice, this is only of central importance for proper modelling of the pressure-driven expansion of a high-temperature (million degree) corona, as discussed in §3 for the solar wind.

For stars without such a corona, any wind typically remains near or below the stellar photospheric temperature T_*, which as noted above implies a sound speed a_* that is much less than the surface escape speed v_{esc}. This in turn implies that the sound-speed terms on the right-hand-side of eqn. (2.12) are quite negligible, of order $s_* \equiv a_*^2/v_{esc}^2 \sim 10^{-3}$ smaller than the gravity near the stellar surface. These terms are thus of little dynamical importance in determining the overall wind properties, like the mass loss rate or velocity law (see §4). However, it is still often convenient to retain the sound-speed term on the left-hand-side, since this allows for a smooth mapping of the wind model onto a hydrostatic atmosphere through a subsonic wind base.

In general, to achieve a supersonic flow with a net outward acceleration, eqn. (2.12) shows that the net forces on the right-hand-side must be positive. For coronal winds, this occurs by the sound-speed terms becoming bigger than gravity. For other stellar winds, overcoming gravity requires the additional body force represented by g_x, for example from radiation (§4).

2.4 Energy Requirements of a Spherical Wind Outflow

In addition to these force or momentum conditions for a wind outflow, it is instructive to identify explicitly the general energy requirements. Combining the momentum and internal energy equations for steady, spherical expansion, we can

integrate to obtain the *total energy* change from the base stellar radius R_* to some given radius r

$$\dot{M}\left[\frac{v^2}{2} - \frac{GM_*}{r} + \frac{\gamma}{\gamma-1}\frac{P}{\rho}\right]_{R_*}^{r} = \int_{R_*}^{r}\left(\dot{M}g_x + 4\pi r'^2 Q_x\right)dr' - 4\pi\left[r'^2 F_c\right]_{R_*}^{r} . \tag{2.13}$$

On the left-hand-side, the terms represent the kinetic energy, gravitational potential energy, and internal enthalpy. To balance this, on the right-hand-side are the work from the force g_x, the net volumetric heating Q_x, and the change in the conductive flux F_c. Even for the solar wind, the enthalpy term is generally much smaller than the larger of the kinetic or potential energy. Neglecting this term, evaluation at arbitrarily large radius $r \to \infty$ thus yields the approximate requirement for the total energy-per-unit-mass

$$\frac{v_\infty^2}{2} + \frac{v_{esc}^2}{2} \approx \int_{R_*}^{\infty}\left(g_x + 4\pi r'^2 Q_x/\dot{M}\right)dr' + \frac{4\pi R_*^2 F_{c*}}{\dot{M}} \tag{2.14}$$

where F_{c*} is the conductive heat flux density at the coronal base, and we have assumed the outer heat flux vanishes asymptotically far from the star. This equation emphasizes that a key general requirement for a wind is to supply the combined kinetic plus potential energy. For stellar winds, this typically occurs through the direct work from the force g_x. For the solar wind, it occurs through a combination of the volume heating and thermal conduction, as we next discuss.

3 Coronal Expansion and Solar Wind

3.1 Reasons for Hot Corona

As in other relatively cool stars, the existence in the sun of a strong near-surface convection zone is understood to provide a source of mechanical energy to heat the upper atmosphere and thereby *reverse* the vertical decrease of temperature of the photosphere. From photospheric values characterized by the effective temperature $T_{eff} \approx 6000$ K, the temperature declines to a minimum $T_{min} \approx 4000$ K, but then rises through a layer (the chromosphere) extending over many scale heights to about $10,000$ K. Above this, it then jumps sharply across a narrow *transition region* of less than scale height, to values in the *corona* of order a *million* degrees! The high pressure associated with this high temperature eventually leads to the outward coronal expansion that is the solar wind. But to provide a basis for a dynamical discussion of this wind, it is first helpful to examine more carefully the underlying reasons for the sudden jump to coronal temperatures.

3.1.1 Temperature Runaway for Exponential Atmosphere

Let us begin by considering the energy balance (2.8) for a strictly steady-state ($\partial/\partial t = 0$), static ($v = 0$) medium

$$\frac{\partial e}{\partial t} = 0 = Q_x - \nabla \cdot \mathbf{F}_c \,. \tag{3.1}$$

For the moment, let us also ignore conduction, but consider that there is a local source of mechanical heating associated with dissipation of some generic wave energy flux F_E over some damping length λ_d. To maintain a steady state with no net heating, assume this energy deposition is balanced by radiative cooling, taken to follow the usual optically thin scaling (e.g. Cox and Tucker 1969; Raymond, Cox, and Smith 1976),

$$Q_x = \frac{F_E}{\lambda_d} - n_H n_e \Lambda(T) = 0 \,, \tag{3.2}$$

where $\Lambda(T)$ is the optically thin cooling function, plotted schematically in figure 1. The overall scaling with the product of the hydrogen and electron number densities, n_H and n_e, reflects the fact that the radiative cooling arises from collional excitation of ions by electrons, for some assumed abundance of ion species per hydrogen atom.

Consider then the nature of this energy balance within a hydrostatically stratified atmosphere, for which all the densities are declining *exponentially* in height z, with a scale height $H \ll R_*$. If the damping is linked to material absorption, it might scale inversely with density, but even so cooling would still scale with one higher power of density. Using eqn. (3.2), we thus find the radiative cooling function needs to increase exponentially with height

$$\Lambda[T(z)] \sim \frac{F_E}{\lambda_d \, \rho^2} \sim F_E \, e^{+z/H} \,. \tag{3.3}$$

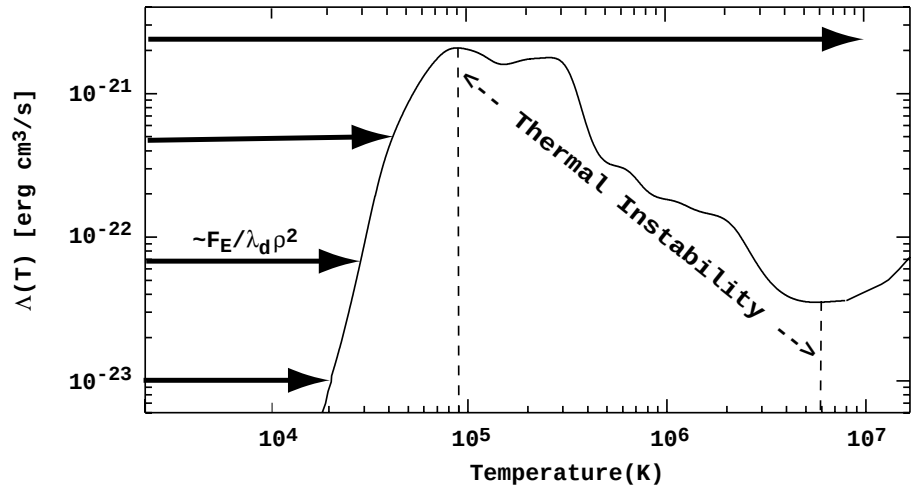

Fig. 1. Radiative cooling function $\Lambda(T)$ plotted vs. temperature T on a log-log scale. The arrows from the left represent the density-scaled rate of energy deposition, which increases with the exponential decrease in density with height. At the point where this scaled heating exceeds the maximum of the cooling function, the radiative equilibrium temperature jumps to a much higher value, in excess of 10^7 K.

As illustrated in figure 1, for any finite wave flux this required increase will lead to a steadily higher temperture until, upon reaching the local maximum of the cooling function at a temperature of ca. 10^5 K, a radiative balance can no longer be maintained without a drastic jump to very much higher temperature, above 10^7 K.

This *thermal instability* is the direct consequence of the decline in cooling efficiency above 10^5 K, which itself is an intrinsic property of radiative cooling, resulting from the progressive ionization of those ion stages that have the bound electrons needed for line emission. The characteristic number density at which runaway occurs can be estimated as

$$n_{run} \approx \sqrt{\frac{F_E}{\lambda_d \Lambda_{max}}} \approx 3.8 \times 10^7 \, cm^{-3} \sqrt{\frac{F_5 R_\odot}{\lambda_h}} \tag{3.4}$$

where $\Lambda_{max} \approx 10^{-21} \, erg \, cm^3/s$ is the maximum of the cooling function [see figure 1]. The latter equality evaluates the scaling in terms of typical solar values for damping length $\lambda_d \approx R_\odot$ and wave energy flux density $F_5 = F_E/10^5 erg/cm^2/s$. This is roughly comparable to the inferred densities at the base of the solar corona, i.e. just above the top of the transition region. Alternatively, if the damping is itself the result of material absorption of the energy flux with some given cross section σ, then $\lambda_d = 1/(n\sigma)$, and we obtain for the runaway density

$$n_{run} \approx \frac{F_E \sigma}{\Lambda_{max}} \approx 10^8 \, cm^{-3} \, F_5 \sigma_{-18} \, , \tag{3.5}$$

where $\sigma_{-18} \equiv \sigma/10^{-18}\, cm^2$.

A general point here is that any finite level of external heating will, for such an exponentially stratified, hydrostatic atmosphere, have a density at which radiative cooling will not be able to balance the heating, thus leading to a high temperature runaway.

3.1.2 Coronal Heating with a Conductive Thermostat

In practice, the outcome of this temperature runaway of radiative cooling tends to be tempered by conduction of heat back into the cooler, denser atmosphere. Instead of the tens of million degrees needed for purely radiative restabilization, the resulting characteristic coronal temperature is "only" a few million degrees. To see this temperature scaling, consider a simple model in which the upward energy flux F_E through a base radius R_* is now balanced at each coronal radius r purely by downward conduction

$$4\pi R_*^2 F_E = 4\pi r^2 K_o T^{5/2} \frac{dT}{dr}\,. \tag{3.6}$$

Integration between the base radius R_* and an assumed energy deposition radius R_d yields a characteristic peak coronal temperature

$$T \approx \left[\frac{7}{2}\frac{F_E}{K_o}\frac{R_d - R_*}{R_d/R_*}\right]^{2/7} \approx 2\times 10^6\, K\, F_5^{2/7}\,, \tag{3.7}$$

where the latter scaling applies for a solar coronal case with $R_* = R_\odot$ and $R_d = 2R_\odot$. This is in good general agreement with observational diagnostics of coronal electron temperature, which typically give values near 2 MK.

However, recent observations (Kohl *et al.* 1999; Cranmer *et al.* 1999) of the "coronal hole" regions thought to be the source of high-speed solar wind suggest that the temperature of *protons* can be significantly higher, about $4-5$ MK. Coronal holes are very lower density regions wherein the collisional energy coupling between electrons and protons can be insufficient to maintain a common temperature. For complete decoupling, an analogous conductive model would then require that energy added to the proton component must be balanced by its *own* thermal conduction. But because of the higher mass and thus lower thermal speed, proton conductivity is reduced by the root of the electron/proton mass ratio, $\sqrt{m_e/m_p} \approx 43$, relative to the standard electron value used above. Application of this reduced proton conductivity in eqn. (3.7) thus yields a proton temperature scaling

$$T_p \approx 5.8\times 10^6\, K\, F_5^{2/7}\,, \tag{3.8}$$

where now $F_5 = F_{Ep}/10^5\, erg/cm^2/s$, with F_{Ep} the base energy flux associated with proton heating. Eqn. (3.8) matches better with the higher inferred proton temperature in coronal holes, but more realistically, modelling the proton energy balance in such regions must also account for the energy losses associated with coronal expansion into the solar wind (see §3.3).

3.1.3 Outward Extension of High Coronal Temperature by Conduction

Since the thermal conductivity increases with temperature as $T^{5/2}$, the high characteristic coronal temperature also implies a strong *outward* conduction flux F_c. For a conduction-dominated energy balance, this conductive heat flux has almost zero divergence,

$$\nabla \cdot \mathbf{F}_c = \frac{1}{r^2} \frac{d(r^2 K_o T^{5/2}(dT/dr))}{dr} \approx 0\,. \tag{3.9}$$

Upon double integration, this gives a temperature that declines only slowly outward from its coronal maximum, i.e. as $T \sim r^{-2/7}$.

The overall point thus is that, once a coronal base is heated to a very high temperature, thermal conduction should tend to extend that high temperature outward to quite large radii.

3.1.4 Pressure Extension of Spherical, Hydrostatic Corona

This radially extended high temperature of a corona has important implications for the dynamical viability of maintaining a hydrostatic stratification. First, for such high temperature, eqn. (2.5) shows that ratio of scale height to radius is no longer very small. For example, for the typical solar coronal temperature of 2 MK, the scale height is about 15% of the solar radius. In considering a possible hydrostatic stratification for the solar corona, it is thus now important to take explicit account of the radial decline in gravity,

$$\frac{d\ln P}{dr} = -\frac{GM_*}{a^2 r^2}\,. \tag{3.10}$$

Motivated by the above conduction-dominated temperature scaling $T \sim r^{-2/7}$, let us consider a slightly more general model for which the temperature has a power-law radial decline, $T/T_* = a^2/a_*^2 = (r/R_*)^{-q}$. Integration of eqn. (3.10) then yields

$$\frac{P(r)}{P_*} = \exp\left(\frac{R_*}{H_*(1-q)}\left[\left(\frac{R_*}{r}\right)^{1-q} - 1\right]\right)\,, \tag{3.11}$$

where $H_* \equiv a_*^2 R_*^2/GM_*$. A key difference from the exponential stratification of a nearly planar photosphere (cf. eqn. 2.4) is that the pressure now approaches a *finite* value at large radii $r \to \infty$,

$$\frac{P_\infty}{P_*} = e^{-R_*/H_*(1-q)} = e^{-14/T_6(1-q)}\,, \tag{3.12}$$

where the latter equality applies for solar parameters, with T_6 the coronal base temperature in units of 10^6 K. This gives $\log(P_*/P_\infty) \approx 6/T_6/(1-q)$.

To place this in context, we note that a combination of observational diagnostics give $\log(P_{TR}/P_{ISM}) \approx 12$ for the ratio between the pressure in the transition region base of the solar corona and that in the interstellar medium. This implies that a hydrostatic corona could only be contained by the interstellar medium if

$(1-q)T_6 < 0.5$. Specifically, for the conduction-dominated temperature index $q = 2/7$, we require $T_6 < 0.7$. Since this is well below the observational range $T_6 \approx 1.5 - 3$, the implication is that a conduction-dominated corona cannot remain hydrostatic, but must undergo a continuous expansion, known of course as the solar wind.

However, it is important to emphasize here that this classical and commonly cited argument for the "inevitability" of the solar coronal expansion depends crucially on *extending* a high temperature at the coronal base far outward. For example, a base temperature in the observed range $T_6 = 1.5 - 3$ would still allow a hydrostatic match to the interstellar medium pressure if the temperature were to decline with just a somewhat bigger power index $q = 2/3 - 5/6$.

In classical models, the strong heat conduction of electrons is envisioned as providing the necessary energy flux to maintain this high temperature. But modern measurements of the solar corona now suggest that the temperature of protons (and other ions) is actually much higher ($T_p > 4$ MK) than of electrons ($T_e \approx 1.5$ MK), implying that they are thermally decoupled, and thus that electron conduction cannot be a mechanism for maintaining a high proton temperature. But before examining this issue further through a discussion of the coronal energy balance (§3.3), let us first examine wind solutions for the idealized cases of an isothermal or polytropic coronal expansion.

ASIDE: For a polytropic case $P \sim \rho^\alpha$, hydrostatic equilibrium in a spherical corona integrates to

$$\frac{P(r)}{P_*} = \left[1 - \frac{\alpha-1}{\alpha}\,\frac{R_*}{H_*}\left(1-\frac{R_*}{r}\right)\right]^{\alpha/(\alpha-1)} = \left[1 - \frac{28}{5T_6}\,\left(1-\frac{R_\odot}{r}\right)\right]^{5/2}\,, \quad (3.13)$$

where the latter equality applies to the solar case with $\alpha = \gamma = 5/3$, as appropriate for an adiabatic, monotonic gas. Note that this now reaches a *zero* pressure at a finite radius

$$R_{P=0} = \frac{R_*}{1 - \frac{\gamma}{\gamma-1}\,\frac{H_*}{R_*}} = \frac{R_\odot}{1 - 5T_6/28}\,. \quad (3.14)$$

Only for very high coronal base temperatures, i.e. $T_6 > 28/5 = 5.6$ in the solar case, is the asymmptotic pressure finite, $P_\infty > 0$. This represents a circumstance in which the base scale height becomes comparable to the stellar radius, i.e. $H_*/R_* > (\gamma-1)/\gamma = 2/5$. It also means that the total internal energy (i.e. enthalpy) $a^2\gamma/(1-\gamma) = (5/2)kT/\mu$ exceeds the gravitational binding energy GM_*/R_*, implying that the gas has sufficient energy to escape without any extended heating. This thus represent an adiabatic "escape temperature" for a corona.

But a key point is that even heating to temperatures of order a million degrees does not imply a need for pressure-driven coronal expansion if there is no addition of energy to keep the gas from remaining adiabatic.

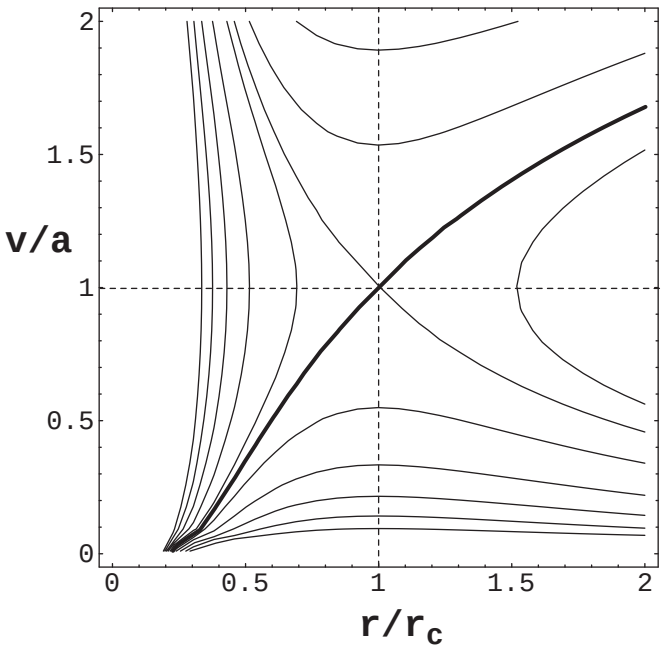

Fig. 2. Solution topolgy for an isothermal coronal wind, plotted via contours of the integral solution (3.17) with various integration constants C, as a function of the ratio of flow speed to sound speed v/a, and the radius over critical radius r/r_s. The heavy curve drawn for the contour with $C = -3$ represents the transonic solar wind solution.

3.2 Solar Wind Models

3.2.1 Isothermal Solutions

These problems with maintaining a hydrostatic corona motivate consideration of dynamical wind solutions. A particularly simple example is that of an *isothermal*, steady-state, spherical wind, for which the equation of motion [from eqn. (2.12), without external driving ($g_x = 0$) or sound-speed gradient ($da^2/dr = 0$)] becomes

$$\left(1 - \frac{a^2}{v^2}\right) v \frac{dv}{dr} = \frac{2a^2}{r} - \frac{GM_*}{r^2}\,, \tag{3.15}$$

Recall that this uses the ideal gas law for the pressure $P = \rho a^2$, and eliminates the density through the steady-state mass continuity; it thus leaves *unspecified* the constant overall mass loss rate $\dot{M} \equiv 4\pi\rho v r^2$.

The right-hand-side of eqn. (3.15) has a zero at the critical radius

$$r_c = \frac{GM_*}{2a^2}\,. \tag{3.16}$$

At this radius, the left-hand-side must likewise vanish, either through a zero velocity gradient $dv/dr = 0$, or through a sonic flow speed $v = a$. Direct integration of eqn. (3.15) yields the general solution

$$F(r,v) \equiv \frac{v^2}{a^2} - \ln \frac{v^2}{a^2} - 4 \ln \frac{r}{r_c} - \frac{4r_c}{r} = C\,, \tag{3.17}$$

where C is an integration constant. Using a simple contour plot of $F(r,v)$ in the velocity-radius plane, figure 2 illustrates the full "solution topology" for an isothermal wind. Note for $C = -3$, two contours cross at the critical radius ($r = r_c$) with a sonic flow speed ($v = a$). The positive slope of these represents the standard solar wind solution, which is the only one that takes a subsonic flow near the surface into a supersonic flow at large radii.

Of the other initially subsonic solutions, those lying above the critical solution fold back and terminate with an infinite slope below the critical radius. Those lying below remain subsonic everywhere, peaking at the critical radius, but then declining to arbitrarily slow, very subsonic speeds at large radii. Because such subsonic "breeze" solutions follow a nearly *hydrostatic* stratification, they again have a large, finite asymptotic pressure that doesn't match the required interstellar boundary condition.

In contrast, for the solar wind solution the supersonic asymptotic speed means that, for any finite mass flux, the density, and thus the pressure, asymtotically approaches zero. To match a small, but finite interstellar medium pressure, the wind can undergo a shock jump transition onto one of the declining subsonic solutions lying above the decelerating critical solution.

Note that, since the density has scaled out of the controlling equation of motion (3.15), the wind mass loss rate $\dot{M} \equiv 4\pi\rho v r^2$ does not appear in this isothermal wind solution. An implicit assumption hidden in such an isothermal analysis is that, no matter how large the mass loss rate, there is some source of heating that counters the tendency for the wind to cool with expansion. As discussed below, determining the overall mass loss rate requires a model that specifies the location and overall level of this heating.

3.2.2 Temperature Sensitivity of Mass Loss Rate

This isothermal wind solution does nonetheless have some important implications for the *relative* scaling of the wind mass loss rate. To see this, note again that within the *subsonic* base region, the inertial term on the left side of eqn. (3.15) is relatively negligible, implying the subsonic stratification is nearly hydrostatic. Thus, neglecting the inertial term v^2/a^2 in the isothermal solution (3.17) for the critical wind case $C = -3$, we can solve approximately for the *surface* flow speed

$$v_* \equiv v(R_*) \approx a \left(\frac{r_c}{R_*}\right)^2 e^{3/2 - 2r_c/R_*}\,. \tag{3.18}$$

Here "surface" should really be interpreted to mean at the base the hot oorona, i.e. just above the chromosphere-corona transition region.

In the case of the sun, observations of transition region emission lines provide a quite tight empirical constraint on the gas *pressure* P_* at this near-surface coronal base of the wind. Using this and the ideal gas law to fix the associated base density $\rho_* = P_*/a^2$, we find that eqn. (3.18) implies a mass loss scaling

$$\dot{M} \equiv 4\pi\rho_* v_* R_*^2 \approx 56 \frac{P_*}{a} r_c^2 \, e^{-2r_c/R_*} \propto \frac{P_*}{T_6^{5/2}} \, e^{-14/T_6} \, . \tag{3.19}$$

With $T_6 \equiv T/10^6\, K$, the last proportionality applies for the solar case, and is intended to emphasize the steep, exponential dependence on the inverse temperature. For example, assuming a fixed pressure, increasing the coronal temperature from just one to two million degrees implies nearly a factor 200 increase in the mass loss rate!

Even more impressively, decreasing from such a 1 MK coronal temperature to the *photospheric* temperature $T \approx 6000$ K would decrease the mass loss rate by more than a *thousand orders of magnitude*! This reiterates quite strongly that thermally driven mass loss is completely untenable at photospheric temperatures.

The underlying reason for this temperature sensitivity stems from the exponential stratification of the subsonic coronal density between the base and sonic/critical radius r_c. From eqns. (2.5) and 3.16) we see in fact that this critical radius is closely related to the ratio of the base scale height to stellar radius

$$\frac{r_c}{R_*} = \frac{R_*}{2H} = \frac{v_{esc}^2}{4a^2} \, , \tag{3.20}$$

where the latter equality also recalls the link with the ratio of sound speed to surface escape speed. Application in eqn. (3.19) shows that the argument of the exponential factor simply represents the number of base scale heights within a critical radius.

In situ measurements by interplanetary spacecraft show that solar wind mass flux is actually quite constant, varying only by about a factor of 2-4. In conjunction with the predicted scalings like (3.19), and the assumption of fixed based pressure derived from observed transition region emission, this relatively constant mass flux has been viewed as requiring a sensitive *fine tuning* of the coronal temperature.

But as we discuss below (§3.3), a more appropriate perspective is to view this temperature-sensitive mass loss as providing an effective "wind thermostat" for regulating the temperature resulting from coronal heating.

3.2.3 Polytropic Solutions

As a prelude to this further discussion of coronal heating and wind energy balance, let us next examine wind solutions for the somewhat more general case that the pressure follows a polytropic relation $P \sim \rho^\alpha$, where the polytropic index α can range from the $\alpha = 1$ for the isothermal case to the $\alpha = \gamma = 5/3$ for an adiabatic, monatomic gas. Returning to an explicit expression of the pressure gradient term,

the steady-state equation of motion is

$$v\frac{dv}{dr} = -\frac{GM_*}{r^2} - \frac{1}{\rho}\frac{dP}{dr}\,. \tag{3.21}$$

For the polytropic form for the pressure, this can again be integrated directly, now yielding the integration constant

$$E = \frac{v^2}{2} - \frac{GM_*}{r} + \frac{\alpha\, a^2}{\alpha - 1}\,, \tag{3.22}$$

where by the perfect gas law, $a^2 = P/\rho \sim \rho^{\alpha-1}$, with again a the (isothermal) sound speed.

In terms of a critical speed $v_c^2 \equiv GM_*/2r_c = \alpha a_c^2$, let us define a scaled speed $w = v/v_c$ and scaled radius $x = r/r_c$; using the steady mass conservation $\rho \sim 1/vr^2 \sim 1/wx^2$, we can then rewrite the energy integral in the dimensionless form

$$\epsilon = \frac{w^2}{4} - \frac{1}{x} + \frac{\left(wx^2\right)^{1-\alpha}}{2(\alpha-1)}\,, \tag{3.23}$$

where $\epsilon \equiv E/(GM_*/r_c)$. For $\alpha \gtrsim 1$, contour plots of ϵ in the $w - x$ plane give a solution topology very similar to the isothermal case $\alpha = 1$. The critical, transonic solution now corresponds to a contour with $\epsilon = (5 - 3\alpha)/4(\alpha - 1)$. Note that for the adiabatic case $\alpha = 5/3$, $\epsilon = 0$.

Figure 3 plots w vs. x for various critical solutons with various α. Note in particular that, for $\alpha = 3/2$, $w = 1$ ($v = v_c$) is a complete solution. For $\alpha > 3/2$, the speed at the base for this critical solution starts already a value greater than the critical speed v_c. For such cases, and in particular for the adiabatic case $\alpha = 5/3$, the critical solution does not have the required properties for a viable wind model, namely to become supersonic in the outer wind starting from a low speed at the stellar surface.

This again emphasizes (cf. end of §3.1.4) that a transonic wind expansion requires sustaining the high temperature against adiabatic cooling through some form of extended heating or energy addition.

3.3 Energy Balance of the Solar Corona and Wind

Let us now consider explicitly these energy requirements for a thermally driven coronal wind. For a purely thermally driven case, there is no direct external driving force, $g_x = 0$. Then from eqn. (2.13), the total energy change from a base radius R_* to a given radius r is

$$\dot{M}\left[\frac{v^2}{2} - \frac{v_{esc}^2}{2}\frac{R_*}{r} + \frac{\gamma a^2}{\gamma - 1}\right]_{R_*}^{r} = 4\pi\int_{R_*}^{r} r'^2 Q_x dr' + 4\pi\left[R_*^2 F_{c*} - r^2 F_c\right]\,. \tag{3.24}$$

Note that without the energy source terms on the right-hand-side, the square bracket term on the left-hand-side would be constant, representing then the adiabatic case of the above polytropic model, i.e. with $\alpha = \gamma$. The expression here of

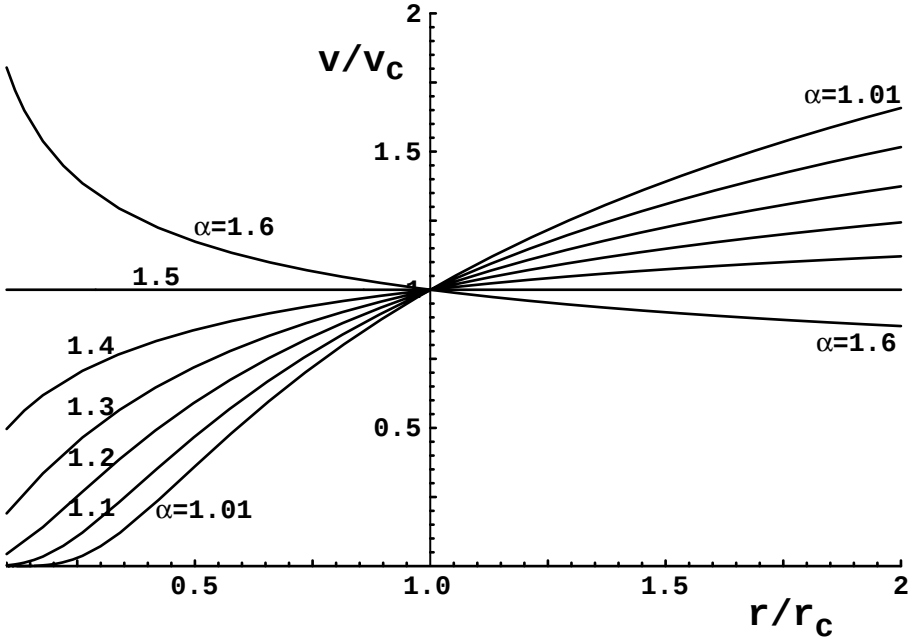

Fig. 3. Polytropic wind solutions, plotted as velocity over critical velocity v/v_c vs. radius over critical radius r/r_c for various polytropic indices in the range for nearly isothermal $\alpha = 1.01$ to nearly adiabatic $\alpha = 1.6$.

the gravitational and internal enthalpy in terms the associated escape and sound speed v_{esc} and a allows convenient comparison of the relative magnitudes of these with the kinetic energy term, $v^2/2$. For a typical coronal temperature of a few MK, $a^2 \ll v_{esc}^2$, implying that the gravitational term dominates in the subsonic, nearly static base (where $v \approx 0$). Far from the star, this gravitational term vanishes, and so for a supersonic solar wind the kinetic energy term dominates. As noted already in §2.4 (cf. eqn. 2.14), even for a thermally driven wind, we can thus effectively *ignore* the *enthalpy* term in the global wind energy balance,

$$E_w \equiv \dot{M}\left(\frac{v_\infty^2}{2} + \frac{v_{esc}^2}{2}\right) \approx 4\pi \int_{R_*}^{r} r'^2 Q_x dr' + 4\pi R_*^2 (F_{c*})\,. \tag{3.25}$$

Here F_{c*} is the conductive heat flux density at the coronal base, and we have assumed the outer heat flux vanishes asymptotically far from the star.

3.3.1 Coronal Heating with a Solar Wind Thermostat

Recalling the analysis in §3.1.2 of how conduction can balance the heating of a strictly a static corona, eqn. (3.25) now represents a generalization to account for

wind energy losses. To develop a general picture, let us assume that (as is often the case) the wind terminal speed is roughly equal to the surface escape speed, $v_\infty \approx v_{esc}$. Then the total wind energy required is

$$\dot{E}_w \approx \dot{M} \frac{2GM_*}{R_*} \,. \tag{3.26}$$

To estimate the mass loss rate, let us apply the isothermal scaling relation eqn. (3.19), which with eqn. (3.26) then gives an overall scaling of this wind energy loss with coronal temperature and pressure. Competing against this is the downward conduction flux, which powers the radiative losses of the underlying transition region, and thus sets the coronal base pressure

$$P_* \approx \frac{F_c}{u_T} \,, \tag{3.27}$$

where $u_T \approx 14$ km/s is a proportionality constant with units of speed (see, e.g. Leer, Hansteen, and Holzer 1998). Combining eqns. (3.19), (3.26), and (3.27), we find that the ratio of wind to conductive energy loss scales as

$$\frac{\dot{E}_w}{\dot{E}_c} = 17.8 \frac{a}{u_T} \left(\frac{r_c}{R_*}\right)^3 e^{-2r_c/R_*} = \frac{5\times 10^4}{T_6^{5/2}} e^{-14/T_6} \,, \tag{3.28}$$

where the latter equality applies to solar parameters. Evaluation indicates that conduction still dominates for temperatures below about 1.4 MK, but above this temperature, the wind dominates. For a relatively low base energy flux $F_E < 10^5\, erg/cm^2/s$, we thus expect the conductive loss scaling of §3.1.2 and eqn. (3.7) should apply. But for higher energy flux $F_E > 10^5\, erg/cm^2/s$, the steep increase in mass and energy loss associated with coronal expansion into the solar wind should provide an effective temperature regulation to the base corona.

In this sense, the problem of "fine-tuning" the coronal temperature to give the observed, relativey steady mass flux is resolved by a simple change of perspective, recognizing instead that for a fixed level of coronal heating, the temperature-sensitve mass and energy loss of the solar wind provides a very effective "thermostat" for the coronal temperature.

3.3.2 Extended Energy Addition and High-Speed Wind Streams

More quantitative analyses solve for the wind mass loss rate and velocity law in terms of some model for both the level and spatial distribution of energy addition into the corona and solar wind. The specific physical mechanisms for the heating are still a matter of investigation, but one quite crucial question regards the relative fraction of the total base energy flux deposited in the subsonic vs. supersonic portion of the wind. Models with an explicit energy balance generally confirm a close link between mass loss rate and energy addition to the subsonic base of coronal wind expansion. By contrast, in the supersonic region this mass flux is

essentially fixed, and so any added energy there tends instead to increase the energy-per-mass, as reflected in asymptotic flow speed v_∞.

A important early class of solar wind models assumed some localized deposition of energy very near the coronal base, with conduction then spreading that energy both downward into the underlying atmosphere and upward into the extended corona. As noted, the former can play a role in regulating the coronal base temperature (§§3.1.2 and 3.3.1), while the latter can play a role in maintaining the high coronal temperature needed for wind expansion (§3.1.3). Overall, such conduction models of solar wind energy tranport were quite successful in reproducing interplanetary measurements of the speed and mass flux of the "quiet", low-speed ($v_\infty \approx 350 - 400$ km/s) solar wind.

However, such models generally fail to explain the high-speed ($v_\infty \approx 700$ km/s) wind streams that are thought to emanate from solar "corona holes". Such coronal holes are regions where the solar magnetic field has an open configuration that, in constrast to the closed, nearly static coronal "loops", allows outward, radial expansion of the coronal gas. To explain the high speed streams, it seems that some substantial fraction of the mechanical energy propagating upward through coronal holes must not be dissipated as heat near the coronal base, but instead must reach upward into the supersonic wind, where it provides either a direct acceleration (e.g. via a wave pressure that gives a net outward g_x) or heating ($Q_x > 0$) that powers extended gas pressure acceleration to high speed.

Recent observations of such coronal hole regions from the SOHO satellite (Kohl *et al.* 1999; Cranmer *et al.* 1999) show temperatures of $T_p \approx 4 - 5$ MK for the protons, and perhaps as high as 100 MK for minor ion species like oxygen. The fact that such proton/ion temperatures are much higher than the ca. 2 MK inferred for electrons shows clearly that electron heat conduction does not play much role in extending the effect of coronal heating outward in such regions. The fundamental reasons for the differing temperature components are a topic of much current research; one promising model invokes ion-cyclotron-resonance damping of magnetohydrodynamics waves (Cranmer 2000).

In general, it seems clear that magnetic fields play a key role in the storage, transport, channelling, and dissipation of mechanical energy for coronal heating. Monitoring by orbiting coronagraphs show the corona to be highly structured and variable on a range of spatial and temporal scales, with a constant jostling of field guided loops, puntuated by sporadic flares and/or coronal mass ejection events associated with release of energy through magnetic reconnection. *In situ* measurements by interplanetary spacecraft show the resulting solar wind is likewise highly variable, sometimes as a result of temporal changes induced in the coronal source regions, and sometimes in the form of "coroting interaction regions" between slow- and high-speed solar wind streams emanating from different spatial region of the rotating solar surface.

Although a detailed discussion is beyond the present scope, such complexities should be kept in mind to provide proper context for the simple overview given here.

3.4 Summary for the Solar Wind

- The solar wind is driven by the gas pressure gradient of the high-temperature solar corona.
- The hot corona is the natural consequence of heating from mechanical energy generated in the solar convection zone. At low density radiative cooling cannot balance this heating, leading to a thermal runaway up to temperatures in excess of a million degrees, at which inward thermal conduction back into the atmosphere can again balance the heating.
- Outward thermal conduction can extend this high temperature well away from the coronal base.
- For such a hot, extended corona, hydrostatic stratification would lead to an asymptotic pressure that exceeds the interstellar value, thus requiring a net outward coronal expansion that becomes the supersonic solar wind.
- Because the wind mass flux is a sensitive function of the coronal temperature, the energy loss from wind expansion acts as an effective coronal thermostat.
- While the mass loss rate is thus set by energy deposition in the subsonic wind base, energy added to the supersonic region increases the flow speed.
- The high-speed wind streams that emanate from coronal holes require extended energy deposition. Coronal-hole observations showing the proton temperature significantly exceeds the electron temperature rule out electron heat conduction as the mechanism for providing the extended energy.
- Magnetic fields lead to extensive structure and variablity in the solar corona and wind.

4 Line-Driven Winds from OB-Stars

4.1 Overview and Comparision with the Solar Wind

Among the most massive stars – which tend also to be the hottest and most luminous – stellar winds can be very strong, with important consequences for both the star's own evolution, as well as for the surrounding interstellar medium. In contrast to the *gas*-pressure-driven solar wind, such hot-star winds are understood to be driven by the pressure of the star's emitted *radiation*.

The sun is a relatively low-mass, cool star with a surface temperature about 6000 K; but as discussed in §3 its wind arises from pressure-expansion of the very hot, million-degree solar corona, which is somehow superheated by the mechanical energy generated from convection in the sun's subsurface layers. By contrast, high-mass stars with much hotter surface temperatures (10,000-100,000 K) are thought to lack the strong convection zone needed to heat a circumstellar corona. Their stellar winds thus remain at temperatures comparable to the star's surface, and so lack the very high gas-pressure needed to drive an outward expansion against the stellar gravity. However such hot stars have a quite high radiative flux, since by the Stefan-Boltzmann law this scales as the fourth power of the surface temperature. It is the pressure of this *radiation* (not of the gas itself) that drives the wind expansion.

The typical flow speeds of hot-star winds – up to about 3000 km/s – are a factor few faster than the 400-700 km/s speed of the solar wind. But the inferred mass loss rates of hot stars greatly exceed – by up to a factor of a billion! – that of the sun. At the sun's current rate of mass loss, about $10^{-14} M_\odot/yr$, its mass would be reduced by only $\sim 0.01\%$ during its entire characteristic lifespan of 10 billion (10^{10}) years. By contrast, even during the comparitively much shorter, few million (10^6) year lifetime typical for a massive star, its wind mass loss at a rate of up to $10^{-5} M_\odot/yr$ can substantially reduce, by a factor of two or more, the original stellar mass of a few times $10 M_\odot$. Indeed, massive stars typically end up as "Wolf-Rayet" stars, which often appear to have completely lost their original envelope of hydrogen, leaving exposed at their surface the elements like carbon, nitrogen, and oxygen that were synthesized by nuclear processes in the stellar core. In addition to directly affecting the star's own evolution, hot-star winds often form "wind-blown bubbles" in nearby interstellar gas. Overall they represent a substantial contribution to the energy, momentum, and chemical enrichment of the interstellar medium in the Milky Way and other galaxies.

4.2 Radiative Acceleration

In terms of the general equation of motion (2.12) for a spherical symmetric, steady wind, the key term now is external acceleration g_x, which for hot-stars results from the absorption and scattering of the star's radiation. In its most general, vector

form, this radiative acceleration can be written as

$$\mathbf{g}_{rad} = \int_0^\infty d\nu \ \langle \kappa_\nu \, \hat{\mathbf{n}} I_\nu / c \rangle \ , \tag{4.1}$$

where κ_ν is the specific opacity (a.k.a. mass-absorption coefficient, or cross section per unit mass) for radiation of frequency ν and specific intensiy I_ν in a direction specified by the unit vector $\hat{\mathbf{n}}$. The angle brackets denote angle integration over all such directions. The division by the speed of light c converts the radiative energy to momentum. In general the opacity includes contributions from both continuum and line processes.

For a spherically symmetric wind with an isotropic opacity, eqn. (4.1) gives for the radial component of acceleration

$$g_{rad} = 2\pi \int_{-1}^{1} d\mu \, \mu \int_0^\infty d\nu \, \kappa_\nu \, I_\nu(\mu)/c = \int_0^\infty d\nu \, \kappa_\nu \, F_\nu / c \, . \tag{4.2}$$

where $\mu = \hat{\mathbf{n}} \cdot \hat{\mathbf{r}}$ is the radial projection of the photon direction $\hat{\mathbf{n}}$, and the latter equality introduces the radial energy flux F_ν. In principle, the radiative intensity I_ν and/or flux F_ν can depend in a complex, nonlocal way on the opacity κ_ν, and this presents a key challenge for computation of the radiative driving within hydrodynamic models of hot-star winds. The remainder of this subsection discusses various simplifications and approximations that allow estimation of the radiative acceleration from both lines and continuum in terms of strictly local conditions. Such local force expressions form the basis for the solution in §4.3 of the radial equal of motion to derive scalings for the mass loss rate and velocity law of hot-star winds.

4.2.1 Electron Scattering and the Eddington Limit

We begin by considering the particularly simple case of scattering by free electrons, which is a "gray", or frequency-independent, process. Since gray scattering cannot alter the star's total luminosity L_*, the radiative energy flux at any radius r is simply given by $F = L_*/4\pi r^2$, corresponding to a radiative *momentum* flux of $F/c = L_*/4\pi r^2 c$. For electron scattering in an ionized medium, the opacity is simply a constant given by $\kappa_e = \sigma_e/\mu_e$, where σ_e ($= 0.66 \times 10^{-24} cm^2$) is the classical Thompson cross-section, and the mean atomic mass per free electron is $\mu_e = 2m_H/(1+X)$, with m_H and X the mass and mass-fraction of hydrogen. This works out to a value $\kappa_e = 0.2(1+X) = 0.34 \ cm^2/g$, where the latter result applies for the standard (solar) hydrogen mass fraction $X = 0.72$. The product of this opacity and the radiative momentum flux yields the radiative acceleration (force-per-unit-mass) from free-electron scattering,

$$g_e(r) = \frac{\kappa_e L_*}{4\pi r^2 c}. \tag{4.3}$$

It is of interest to compare this with the star's gravitational acceleration, given by GM_*/r^2, where G is the gravitation constant, and M_* is the stellar mass. Since

both accelerations have the same $1/r^2$ dependence on radius, their ratio is spatially constant, fixed by the ratio of luminosity to mass,

$$\Gamma_e = \frac{\kappa_e L_*}{4\pi G M_* c}. \tag{4.4}$$

This ratio, sometimes called the Eddington parameter, thus has a characteristic value for each star. For the sun it is very small, of order 2×10^{-5}, but for hot, massive stars it is often within a factor of two below unity. As noted by Eddington, electron scattering thus represents a basal radiative acceleration that effectively counteracts the stellar gravity. The limit $\Gamma_e \rightarrow 1$ is known as the Eddington limit, for which the star would become gravitationally unbound.

It is certainly significant that hot stars with strong stellar winds have Γ_e only a factor two or so below this limit, since it suggests that only a modest additional opacity could succeed in fully overcoming gravity to drive an outflow. But it is important to realize that a stellar wind represents the outer envelope outflow from a nearly static, gravitationally bound base, and as such is not consistent with an *entire* star exceeding the Eddington limit. Rather the key requirement for a wind is that the driving force increase naturally from being smaller to larger than gravity at some radius near the stellar surface. We next describe how the force from *line*-scattering is ideally suited for just such a spatial modulation. (In §8, we examine how the "porosity" of a spatially structured medium can provide an analogous modulation for continuum-driven mass loss.)

4.2.2 The Doppler-Shifted Resonance of Line-Scattering

When an electron is bound into one of the discrete energy levels of an atom, its scattering of radiation is primarily with photons of just the right energy to induce shuffling with another discrete level. The process is called line-scattering, because it often results in the appearance of narrowly defined lines in a star's energy spectrum. At first glance, it may seem unlikely that such line-scattering could be effective in driving mass loss, simply because the opacity only interacts with a small fraction of the available stellar flux. But there are two key factors that work to make line-scattering in fact the key driving mechanism for hot-star winds.

The first is the *resonant* nature of line-scattering. The binding of an electron into discrete energy levels of an atom represents a kind of resonance cavity that can greatly amplify the interaction cross section with photons of just the right energy to induce transition among the levels. The effect is somewhat analogous to blowing into a whistle vs. just into open air. Like the sound of whistle, the response occurs at a well-tuned frequency, and has a greatly enhanced strength. Relative to free-electron scattering, the overall amplification factor for a broad-band, untuned radiation source is set by the *quality* of the resonance, $Q \approx \nu_o/A$, where ν_o is the line frequency and A is decay rate of the excited state. For quantum mechanically allowed atomic transitions, this can be very large, of order 10^7. Thus, even though only a very small fraction ($\sim 10^{-4}$) of electrons in a hot-star atmosphere are bound

into atoms, illumination of these atoms by an *unattenuated* (i.e., optically thin), broad-band radiation source would yield a collective line-force that exceeds that from free electrons by about a factor $\overline{Q} \approx 10^7 \times 10^{-4} = 1000$. For stars within a factor two of the free-electron Eddington limit, this implies that line-scattering is capable, in principle, of driving material outward with an acceleration on order a *thousand* times the inward acceleration of gravity!

In practice, of course, this does not normally occur, since any sufficiently large collection of atoms scattering in this way would quickly block the limited flux available within just the narrow frequency bands tuned to the lines. Indeed, in the static portion of the atmosphere, the flux is greatly reduced at the line frequencies. Such line "saturation" keeps the overall line force quite small, in fact well below the gravitational force, which thus allows the inner parts of the atmosphere to remain gravitationally bound.

This, however, is where the second key factor, the *Doppler effect*, comes into play. In the outward-*moving* portions of the outer atmosphere, the Doppler effect red-shifts the local line resonance, effectively desaturating the lines by allowing the atoms to resonate with relatively unattenuated stellar flux that was initially at slightly higher frequencies. By effectively sweeping a broader range of the stellar flux spectrum, this makes it possible for the line force to overcome gravity and accelerate the very outflow it itself requires. As quantified within the CAK wind theory described below, the amount of mass accelerated adjusts such that the self-absorption of the radiation reduces the overall line-driving to being just somewhat (not a factor thousand) above what's needed to overcome gravity.

4.2.3 The Sobolev Approximation for Line-Driving

The late Russian astrophysicist V. V. Sobolev developed an extremely useful approach for treating line-transfer in such a rapidly accelerating flow. As illustrated in figure 4, he noted how radiation emitted radially from the star at frequency somewhat blueward of a line propagates freely until the accelerating flow Doppler shifts the line into into a local resonance with the radiation. For the usual case that the broadening of the line is set by the ion thermal speed v_{th}, the geometric width of this resonance is about a *Sobolev length*, $l_{Sob} \equiv v_{th}/(dv/dr)$. In a supersonic flow, this Sobolev length is of order $v_{th}/v \ll 1$ smaller than a typical flow variation scale, like the density/velocity scale length $H \equiv |\rho/(d\rho/dr)| \approx v/(dv/dr)$.

The nearly homogeneous conditions within such resonance layers imply that the key parameters of the line-scattering can be described in terms of strictly *local* conditions at any radius. In particular, the total optical depth of radiation propagating radially through the line resonance – which normally requires evaluation of a nonlocal spatial integral – can in this case be well approximated simply in terms of the local density and velocity gradient at the resonant radius

$$\tau_s = \rho\kappa l_{Sob} = \frac{\rho\kappa v_{th}}{dv/dr} = \frac{\rho q \kappa_e c}{dv/dr} \equiv qt\,, \tag{4.5}$$

where κ characterizes the opacity near line center. Noting that $\kappa \sim 1/v_{th}$, the second equality eliminates the misleading appearance of the thermal speed by defining

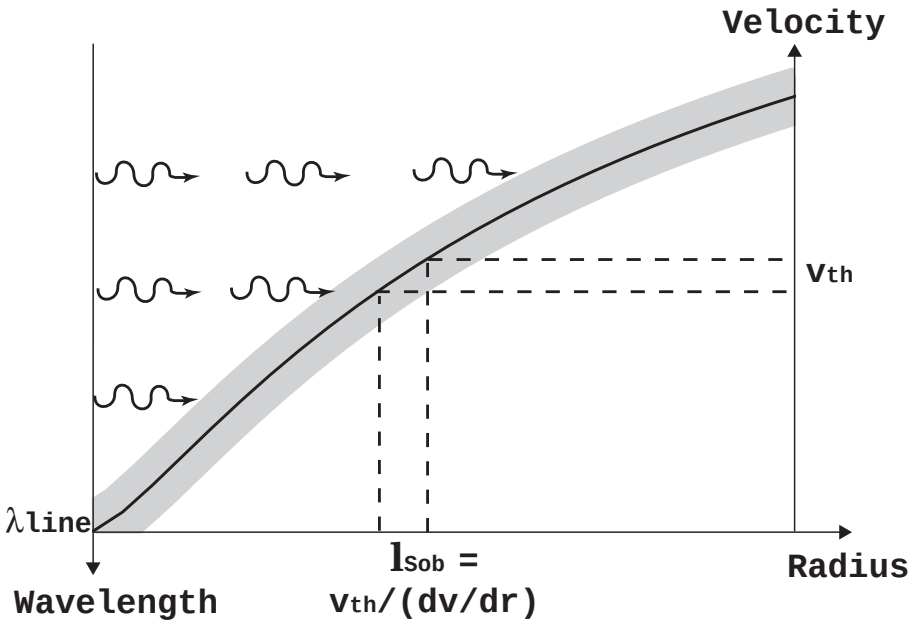

Fig. 4. The Doppler-shifted line-resonance in an accelerating flow. Photons with a wavelength just shortward of a line propagate freely from the stellar surface up to a layer where the wind outflow Doppler shifts the line into a resonance over a narrow width (represented here by the shading) equal to the Sobolev length, set by the ratio of thermal speed to velocity gradient, $l_{Sob} \equiv v_{th}/(dv/dr)$.

a frequency-integrated line-strength $q \equiv \kappa v_{th}/\kappa_e c$, which is actually independent of v_{th}. In the final equality, $t \equiv \kappa_e \rho c/(dv/dr)$ is the Sobolev optical depth for a line with integrated strength equal to free electron scattering, i.e. with $q = 1$.

As is quantified below, the Sobolev optical depth allows a localized solution for how much the flow absorption reduces the illumination of the line-resonance by the stellar flux; this leads to a simple, general expression for the radial line acceleration,

$$g_{line} \approx g_{thin} \frac{1 - e^{-qt}}{qt}. \tag{4.6}$$

In the optically thin limit $\tau_s \ll 1$, this line-acceleration reduces to a form similar to the electron scattering case,

$$g_{thin} \equiv \frac{\kappa v_{th} \nu_o L_\nu}{4\pi r^2 c^2} = w_{\nu_o}\, q\, g_e\,, \tag{4.7}$$

where in the latter equality $w_{\nu_o} \equiv \nu_o L_\nu / L_*$ weights the placement of line within the luminosity spectrum L_ν. Note that for a line with frequency ν_o near the peak of this spectrum L_ν, $\nu_o L_\nu \approx L_*$ and so $w_{\nu_o} \approx 1$.

In the opposite limit of an optically thick line with $\tau_s \gg 1$, there results a quite different form,

$$g_{thick} \approx \frac{g_{thin}}{qt} = w_{\nu_o} \frac{g_e}{t} = w_{\nu_o} \frac{L_*}{4\pi r^2 \rho c^2} \frac{dv}{dr} = w_{\nu_o} \frac{L_*}{\dot{M} c^2} \, v \frac{dv}{dr}, \tag{4.8}$$

where the last equality uses the definition of the wind mass loss rate, $\dot{M} \equiv 4\pi\rho v r^2$.

A key result here is that the optically thick line force is *independent* of the line-strength q, and instead varies in proportion to the velocity gradient dv/dr. The basis of this result is illustrated by figure 4, which shows that the local *rate* at which stellar radiation is red-shifted into a line-resonance depends on the *slope* of the velocity. By Newton's famous equation of motion, a force is normally understood to *cause* an acceleration. But here we see that an optically thick line-force also *depends* on the wind's advective rate of acceleration, $v\, dv/dr$.

4.2.4 Sobolev Localization of Line-Force Integrals for a Point Star

To provide a more quantitative illustration of this Sobolev approximation, let us now derive these key properties of line-driving through the localization of the spatial optical depth integral. Applying the general radial acceleration eqn. (4.2) to the case of a single line of integrated strength q, we find

$$g_{line}(r) = \frac{2\pi q \kappa_e}{c} \int_{-1}^{1} d\mu \, \mu \int_{-\infty}^{\infty} dx \, \phi(x - \mu u(r)) I(x, \mu, r) \, , \tag{4.9}$$

where the integration is now over a scaled frequency $x \equiv (\nu/\nu_o - 1)(c/v_{th})$, defined from line center in units of the frequency broadening associated with the ion thermal motion. The integrand is weighted by the line-profile function $\phi(x)$, which for thermal broadening typically has the Gaussian form $\phi(x) \sim e^{-x^2}$. At a wind radius with velocty $v(r)$, the local line profile is centered on the comoving frame frequency $x - \mu u(r)$, where $u(r) = v(r)/v_{th}$ is the velocity in units of the thermal speed v_{th}.

Here $I(x, \mu, r)$ is the specific intensity at frequency x along a local direction cosine μ. In general this consists of both a *diffuse* component $I_{\rm diff}$ associated with scattered radiation, and *direct* component associated with the attenuated source intensity I_* from the underlying star. In a smooth supersonic wind, the force associated with diffuse component nearly vanishes. As illustrated in figures 5 and 16b, this is because the diffuse intensity has a nearly fore-aft symmetry, $I_{\rm diff}(\mu) \approx I_{\rm diff}(-\mu)$, which thus makes the angle integration vanish due to the overall oddness in μ. (The diffuse component can, however, play an important dynamical role in mitigating the effect of instabilities associated with line-driving; see §5.1.4)

The direct intensity is given by

$$I_{\rm dir}(x, \mu, r) = I_*(\mu) e^{-qt(x,\mu,r)} \, , \tag{4.10}$$

where the exponential reduction takes account of the integrated attenuation of the stellar source intensity I_* by intervening material, as set by the frequency-

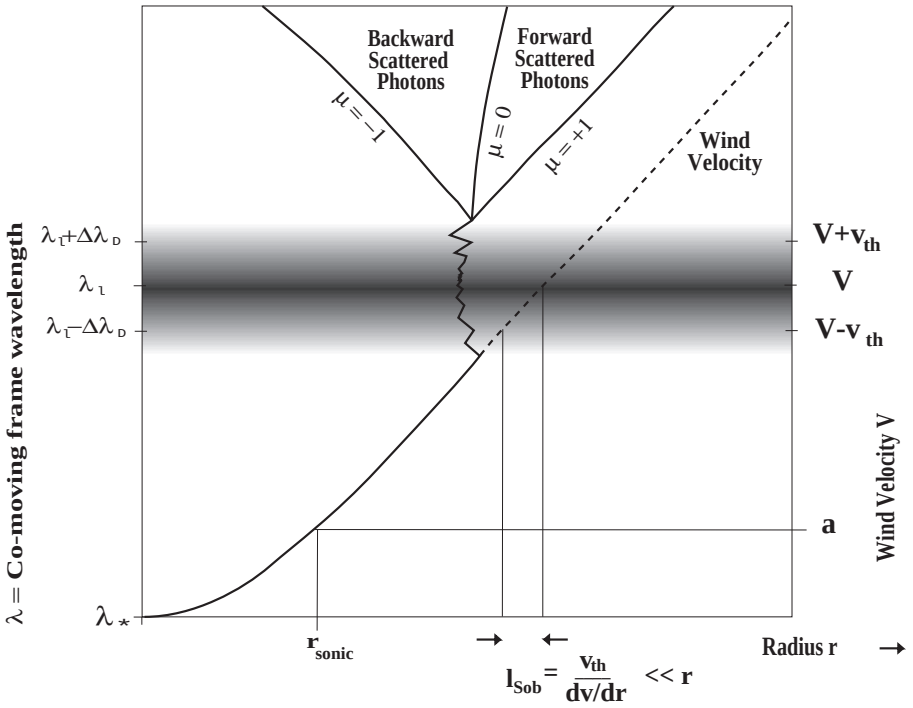

Fig. 5. The Doppler-shifted line-resonance in an accelerating flow, now viewed from the perspective of scattered photons instead absorbing ions (cf. fig. 4). Photons of initial wavelength λ_* are red-shifted by the wind expansion until the comoving-frame wavelength approaches the fixed line-resonance wavelength λ_{line}. They are then scattered many times before the overall wind-expansion shifts their wavelength to the red-edge of the resonance, thus allowing escape with nearly equal probability in the forward or backward directions. The resulting approximate fore-aft symmetry of such scattered radiation means the associated diffuse line-force nearly vanishes.

dependent optical depth $qt(x, \mu, r)$ to the stellar surface at radius R_*. For simplicity, let us consider this optical depth along a *radial* ray with $\mu = 1$,

$$qt(x, 1, r) \equiv \int_{R_*}^{r} dr' \kappa \rho(r') \phi \left(x - v(r')/v_{th}\right) \ . \tag{4.11}$$

A crucial point in evaluating this integral is that in a supersonic wind, the variation of the integrand is dominated by the velocity variation within the line-profile. As noted above, this variation has a scale given by the Sobolev length $l_{Sob} \equiv v_{th}/(dv/dr)$, which is smaller by a factor v_{th}/v than the competing density/velocity scale, $H \equiv |\rho/(d\rho/dr)| \approx v/(dv/dr)$. A key step in the Sobolev approximation is thus to recast this spatial integration as an integration over the comoving-frame

frequency $x' \equiv x - u(r')$,

$$qt(x,1,r) = -\int_{x'(R_*)}^{x'(r)} \frac{dx'\, v_{th}}{dv/dr'}\, \kappa\rho(x')\,\phi(x') \approx \tau_s \Phi(x-u(r))\,, \tag{4.12}$$

where the integrated profile

$$\Phi(x) \equiv \int_x^\infty dx' \phi(x')\,, \tag{4.13}$$

and the latter approximation in (4.12) uses the assumption that $v(r) \gg v_{th}$ to formally extend the surface frequency $x'(R_*)$ to infinity relative to the local resonance $x'(r)$. As defined in eqn. (4.5), the Sobolev optical thickness $\tau_s = qt$ arises here as a collection of spatial variables that are assumed to be nearly constant over the Sobolev resonance zone, and thus can be extracted outside the integral.

To apply this optical depth in computing the line-force, let us for now ignore the finite angular extent of the stellar radiation source, and instead assume the stellar radiation is radial streaming, as from a point source. The associated line acceleration then becomes

$$g_{line}(r) \approx g_{thin} \int_{-\infty}^{\infty} dx\, \phi\left(x-u(r)\right) e^{-qt\Phi(x-u(r))} \tag{4.14}$$

$$= g_{thin} \frac{1-e^{-qt}}{qt}\,. \tag{4.15}$$

The latter equality shows that a remarkable, extra bonus from this approximation is that the resulting optical depth (4.12) now has precisely the form needed to allow analytic evaluation of the line-force integral (4.15), yielding directly the general Sobolev force expression given in eqn. (4.6).

Figure 16a illustrates this frequency integral formulation of the direct line-force.

4.2.5 The CAK Line-Ensemble Force for a Point Star

In practice, a large number of lines with a range of frequencies and strengths can contribute to the wind driving. Castor, Abbott, and Klein (1975; hereafter CAK) introduced a practical formalism for computing the cumulative line-acceleration from a parameterized line-ensemble, under the simplifying assumption that the spectral distribution keeps the individual lines nearly independent. For the point-star model of §4.3.1, direct summation of the individual line-accelerations as given by eqn. (4.6) yields

$$g_{tot} = g_e \sum w_{\nu_o} q \frac{1-e^{-qt}}{qt} \approx g_e \int_0^\infty q \frac{dN}{dq} \frac{1-e^{-qt}}{qt}\, dq\,, \tag{4.16}$$

where the latter equality approximates the discrete sum as a continuous integral over the flux-weighted number distribution dN/dq. Following CAK, a key further

simplification is to approximate this number distribution as a simple power law in the line strength q,

$$q\frac{dN}{dq} = \frac{1}{\Gamma(\alpha)}\left(\frac{q}{\bar{Q}}\right)^{\alpha-1} , \tag{4.17}$$

where $\Gamma(\alpha)$ is the complete Gamma function, the CAK power-law index satisifies $0 < \alpha < 1$, and the above-mentioned cumulative line-strength $\bar{Q}$ provides a convenient overall normalization (cf. §4.2.2). Application of eqn. (4.17) in (4.16) then yields the CAK, point-star, line-force from this line-ensemble

$$g_{CAK} = \frac{\bar{Q}^{1-\alpha}}{(1-\alpha)}\frac{g_e}{t^\alpha} \tag{4.18}$$

$$= \frac{1}{(1-\alpha)}\frac{\kappa_e L_* \bar{Q}}{4\pi r^2 c}\left(\frac{dv/dr}{\rho c \bar{Q}\kappa_e}\right)^\alpha . \tag{4.19}$$

Note that this represents a kind of "geometric mean" between the optically thin and thick forms (eqns. 4.7 and 4.8) for a single line.

CAK dubbed the ratio g_{CAK}/g_e the "force multiplier", written as $M(t) = kt^{-\alpha}$, with k the CAK normalization constant. Note however that CAK used a fiducial thermal speed v_{th} in their definition of the electron optical depth parameter $t = \kappa_e \rho v_{th}/(dv/dr)$, which then gives an artificial thermal-speed dependence to the CAK normalization parameter, $k = (v_{th}/c)^\alpha\, \bar{Q}^{1-\alpha}/(1-\alpha)$. In the Sobolev approximation, the line-force has no physical dependence on the thermal-speed, and so the formal inclusion of a fiducial v_{th} in the CAK parameterization has sometimes led to confusion, e.g., in applying tabulations of the multiplier constant k. The formulation here avoids this problem, since the parameters q, $\bar{Q}$, and $t = \kappa_e \rho c/(dv/dr)$ are all independent of v_{th}. A further advantage is that, for a wide range of hot-star parameters, the line normalization has a relatively constant value $\bar{Q} \approx 2000$ (Gayley 1995).

4.2.6 3D Vector Generalization for the CAK/Sobolev Line-Force

The localization of line-transfer within the Sobolev approximation actually makes it relatively easy to obtain generalizations of the above 1D point-star results, extending even to a full vector form for the line acceleration in 2D or even 3D wind models. Within the same Sobolev approach that emphasizes the central role of Doppler shift, the key is to replace the radial gradient of the radial velocity (dv_r/dr) with the appropriate *projected gradient* of the *projected velocity* in a direction $\hat{\mathbf{n}}$ that is no longer necessarily along the local radial vector $\hat{\mathbf{r}}$,

$$\frac{dv}{dr} \rightarrow \hat{\mathbf{n}} \cdot \nabla\ (\hat{\mathbf{n}} \cdot \mathbf{v}) \equiv dv_n/dn\,. \tag{4.20}$$

As long as this projected gradient is large, e.g. so that the associated Sobolev length $l_{sob} = v_{th}/(dv_n/dn) \ll r$, then the same Sobolev approximation can be applied for each ray of source-surface intensity $I_*(\hat{\mathbf{n}})$. For local absorption of this

intensity in a single line of strength q, the associated vector generalization of the radial-streaming line-acceleration (4.6) is

$$\mathbf{g}_{line}(\mathbf{r}) = \frac{w_{\nu_o} q \kappa_e}{c} \left\langle \hat{\mathbf{n}} I_*(\hat{\mathbf{n}}) \frac{1 - e^{-qt_n}}{qt_n} \right\rangle , \tag{4.21}$$

where again (cf. eqn. 4.1) the angle brackets denote angle integration over all such directions $\hat{\mathbf{n}}$, along which the associated Sobolev optical thickness is now (cf. eqn. 4.5)

$$t_n \equiv \frac{\rho \kappa_e c}{\hat{\mathbf{n}} \cdot \nabla \ (\hat{\mathbf{n}} \cdot \mathbf{v})} \tag{4.22}$$

To obtain the analogous vector form for the CAK ensemble line-force, we likewise (cf. eqn. 4.16) convolve this single-line vector force (4.21) with the CAK power-law distribution (4.17), yielding

$$\mathbf{g}_{CAK} = \frac{\bar{Q}^{1-\alpha} \kappa_e}{(1-\alpha)c} \left\langle \hat{\mathbf{n}} \frac{I_*(\hat{\mathbf{n}})}{t_n^\alpha} \right\rangle \tag{4.23}$$

$$= \frac{(\bar{Q}\kappa_e)^{1-\alpha}}{(1-\alpha)c(\rho c)^\alpha} \left\langle \hat{\mathbf{n}} I_*(\hat{\mathbf{n}}) \left[\hat{\mathbf{n}} \cdot \nabla \ (\hat{\mathbf{n}} \cdot \mathbf{v})\right]^\alpha \right\rangle . \tag{4.24}$$

As discussed in §7, this vector form for the line-acceleration is relevant for multi-dimensional wind models that include rotation effects.

4.2.7 Finite-Disk Form for the CAK Line-Force

In 1D spherical models, this more general form now also provides a way to account for the finite cone-angle of the star. For a star with radius R_*, the cosine of this cone-angle at some wind radius r is $\mu_* = \sqrt{1 - R_*^2/r^2}$. For stellar radiation with local radial projection cosines $\mu \equiv \hat{\mathbf{n}} \cdot \hat{\mathbf{r}}$ in the range $\mu_* < \mu < 1$, the Sobolev optical depth is now given by $t_\mu \equiv t(1+\sigma)/(1+\sigma\mu^2)$, with $\sigma \equiv d\ln v/d\ln r - 1$ and t the radial Sobolev optical depth of eqn. (4.5). Taking the radial component of the vector force (4.24), application of these scalings yields for the finite-disk line-force

$$g_{fd} = \frac{\bar{Q}\kappa_e}{(1-\alpha)ct^\alpha} \left\langle \mu I_*(\mu) \left[\frac{1+\sigma\mu^2}{1+\sigma}\right]^\alpha \right\rangle \tag{4.25}$$

$$= g_{CAK} \left[\frac{(1+\sigma)^{1+\alpha} - (1+\sigma\mu_*^2)^{1+\alpha}}{(1+\alpha)\sigma(1+\sigma)^\alpha(1-\mu_*^2)}\right] , \tag{4.26}$$

where the latter equality evaluates the angle integral for the simple case of uniform intensity I_* (i.e. with no limb darkening) over the stellar disk. The term in square brackets represents a "finite-disk-correction" factor for the simple point star CAK line-force g_{CAK}. We discuss the dynamical effects of this finite-disk correction in §4.3.2; but first, let us next analyze the nature of line-driven winds within the simpler, point-star approximation.

4.3 Steady, Spherically Symmetric Models for Line-Driven Stellar Winds

4.3.1 Point-Star CAK Model in the Zero-Sound-Speed Limit

The simple, local CAK/Sobolev expression (4.19) for the cumulative line-driving force in the point-star approximation provides a convenient basis for deriving the basic scalings for a line-driven stellar wind. Since, as noted above, the gas pressure is not of much importance in the overall wind driving, let us first consider the steady-state equation of motion in the zero-sound-speed limit, $a = 0$. This simply requires that the wind acceleration must equal the line-acceleration minus the inward acceleration of gravity,

$$v\frac{dv}{dr} = g_{CAK} - \frac{GM_*(1-\Gamma_e)}{r^2}, \tag{4.27}$$

wherein we've also taken into account the effective reduction of gravity by the free-electron scattering factor Γ_e. Note from eqn. (4.19) that the CAK line-force g_{CAK} depends itself on the flow acceleration it drives.

Since this feedback between line-driving and flow acceleration is moderated by gravity, let us define the gravitationally scaled inertial acceleration

$$w' \equiv r^2 v v'/GM_*(1-\Gamma_e)\,. \tag{4.28}$$

In terms of an inverse-radius coordinate $x \equiv 1 - R_*/r$, note that $w' = dw/dx$, where $w \equiv v^2/v_{esc}^2$ represents the ratio of wind kinetic energy to the effective gravitational binding $v_{esc}^2/2 \equiv GM_*(1-\Gamma_e)/R_*$ from the surface. Using eqn. (4.19), the equation of motion can then be rewritten in the simple, dimensionless form,

$$w' = C\, w'^{\alpha} - 1, \tag{4.29}$$

where the constant is given by

$$C = \frac{1}{1-\alpha}\left(\frac{\overline{Q}\Gamma_e}{1-\Gamma_e}\right)^{1-\alpha}\left(\frac{L_*}{\dot{M}c^2}\right)^{\alpha}. \tag{4.30}$$

Figure 6 illustrates the graphical solution of this dimensionless equation of motion for various values of the constant C. For fixed stellar and opacity-distribution parameters, this corresponds to assuming various values of the mass loss rate $\dot{M}$, since $C \propto 1/\dot{M}^{\alpha}$. For high $\dot{M}$ (low C), there are no solutions, while for low $\dot{M}$ (high C), there are two solutions. The two limits are separated by a critical case with one solution – corresponding to the *maximal* mass loss rate – for which the function Cw^{α} intersects the line $1+w$ at a tangent. For this critical case, the tangency requirement implies $\alpha C_c w_c'^{\alpha-1} = 1$, which together with the original equation (4.29) yields the critical conditions $w_c' = \alpha/1-\alpha$ and $C_c = 1/\alpha^{\alpha}(1-\alpha)^{1-\alpha}$.

From eqn. (4.30), this critical value of C_c defines the maximal CAK mass loss rate

$$\dot{M}_{CAK} = \frac{L}{c^2}\,\frac{\alpha}{1-\alpha}\left[\frac{\bar{Q}\Gamma}{1-\Gamma}\right]^{(1-\alpha)/\alpha}. \tag{4.31}$$

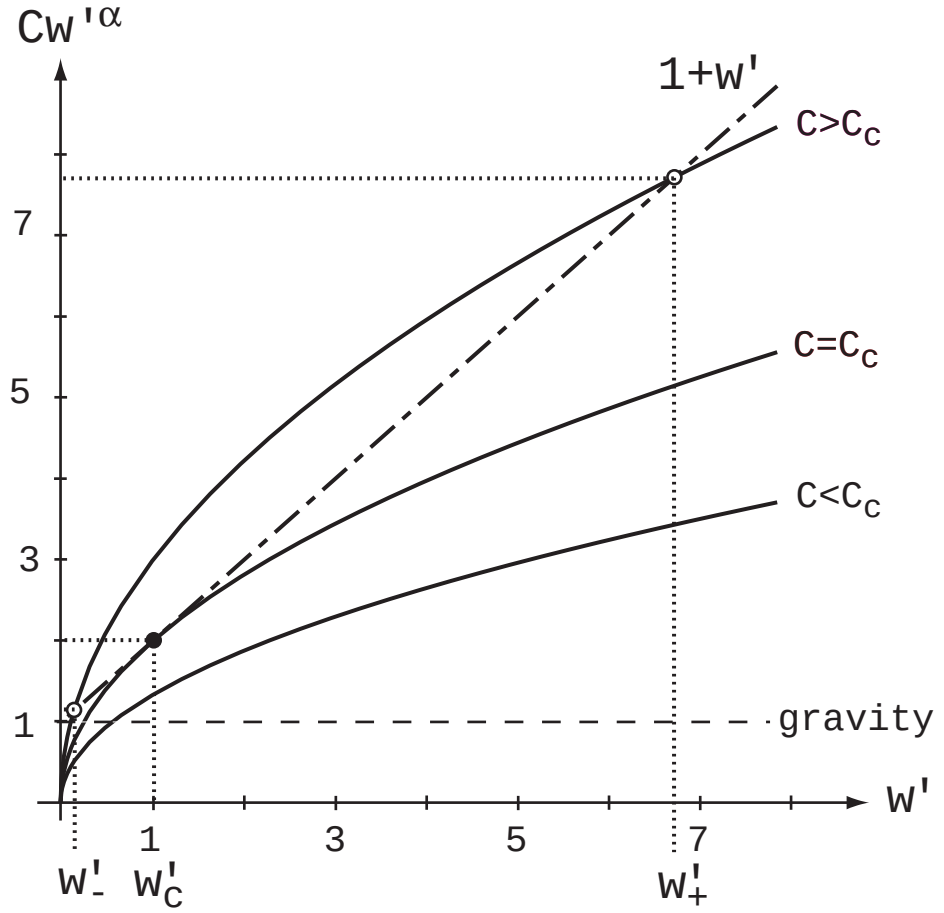

Fig. 6. Graphical solution of the dimensionless equation of motion (4.29) representing a 1D, point-star, zero-sound-speed CAK wind, as controlled by the constant $C \sim 1/\dot{M}^{\alpha}$. If $\dot{M}$ is too big, there are no solutions; if $\dot{M}$ is small there are two solutions. A maximal value $\dot{M} = \dot{M}_{CAK}$ defines a single, "critical" solution.

Moreover, since eqn. (4.29) has no explicit spatial dependence, these critical conditions hold at all radii. By spatial integration of the critical acceleration w'_c from the surface radius R_*, we thus obtain the CAK velocity law,

$$v(r) = v_\infty \left(1 - \frac{R_*}{r}\right)^{1/2} \tag{4.32}$$

where the terminal speed is given by $v_\infty = v_{esc}\sqrt{\alpha/1-\alpha}$, with v_{esc} the effective

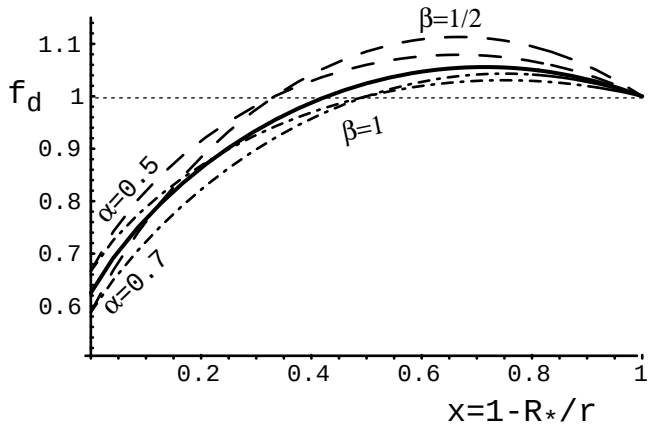

Fig. 7. Spatial variation of the finite-disk-correction factor f_d, plotted vs. scaled inverse radius $x = 1 - R_*/r$, for various CAK exponents α and velocity-law exponents β. The heavy solid curve shows our standard case with $\alpha = 0.6$ and $\beta = 3/4$. The dashed curves use $\beta = 1/2$ and the dot-dashed curves $\beta = 1$, and are each plotted for CAK exponents $\alpha = 0.5$ and $\alpha = 0.7$ that span the nominal range. A key point is that all these varied curves have a similar form, rising sharply from a base value $[f_{d*} = 1/(1 + \alpha)]$, crossing above unity (dotted line), and then relaxing back to it at large radial distances, $x \to 1$.

surface escape speed.

The fact that the critical condition applies equally well at all radii throughout the wind makes this zero-sound-speed, point-star model a degnerate case. The orignal CAK analysis broke this degeneracy by including the small, finite gas-pressure, but in practice a more physically important effect is the finite-disk correction, which brings the critical point very close to the stellar surface, as discussed next.

4.3.2 Finite-Disk Correction

The above analysis has so far been based on the idealization of radially streaming radiation, as if the star were a point-source at the origin. This was the basis of the original CAK wind solutions, although they did already identify (but did not implement) the appropriate "finite-disk correction factor" to account for the full angular extent of the star [see CAK eqn. (50)]. From eqn. (4.26), for a star with a constant surface brightness, this correction factor is given by

$$f_d(r) \equiv \frac{g_{fd}}{g_{CAK}} = \frac{(1+\sigma)^{1+\alpha} - (1+\sigma\mu_*^2)^{1+\alpha}}{(1+\alpha)\sigma(1+\sigma)^{\alpha}(1-\mu_*^2)}\,, \tag{4.33}$$

with $\mu_* \equiv \sqrt{1 - R_*^2/r^2}$ the cosine of the finite-cone angle of the stellar disk, and $\sigma \equiv d\ln v/d\ln r - 1$. The complex dependence on radius, velocity, and velocity

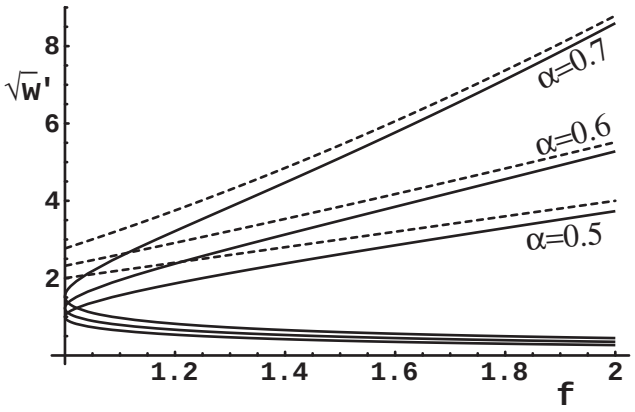

Fig. 8. Root of the scaled acceleration $\sqrt{w'}$ that solves the equation of motion (4.34), plotted as a function of the surface-normalized finite-disk factor f. Since the wind terminal speed scales as $v_\infty \sim \sqrt{w'} v_{esc}$, note that even modest increases in the finite-disk factor can lead to a very high speed wind (especially for larger α). The dashed curves denote the asymptotic solutions $\sim (C_c f)^{1/(2(1-\alpha))}$ that apply in the limit of large acceleration $w' \gg 1$.

gradient now precludes self-consistent analytic wind solutions, like those obtained above for the point-star case. Numerical solutions have been derived independently by Friend and Abbott (1986) and Pauldrach, Puls, and Kudritzki (1986). They yield a somewhat reduced mass loss rate $\dot{M}_{fd} \approx \dot{M}_{CAK}/(1+\alpha)^{1/\alpha}$, higher terminal speed $v_\infty \approx 3 v_{esc}$, and flatter velocity law, roughly characterized by replacing the exponent 1/2 in eqn. (4.32) with a somewhat higher value $\beta \approx 0.8 - 1$.

If one simply assumes such a canonical "beta" velocity law, figure 7 illustrates the specific radial variations of $f_d(r)$ for various CAK exponents α and velocity exponents β. All these varied cases show a quite common general behavior. For the initial acceleration from a static stellar surface $r \approx R_*$ (where $v \to 0$ with finite dv/dr implies $\sigma \to \infty$), f_d has a starting value $f_{d*} \approx 1/(1+\alpha)$. It then increases outward, past unity at the point where the wind has a locally isotropic expansion (with $dv/dr = v/r$, so that $\sigma = 0$). Finally it falls back asymptotically toward unity at large radii, where the star is indeed well approximated by a point source.

To understand the dynamical effect of this finite-disk factor, it is helpful to examine how such a typical radial variation influences the scaled acceleration w' through solutions to the appropriately modified equation of motion (cf. eqn 4.29),

$$w' = -1 + f\, C_*\, (w')^\alpha\,, \tag{4.34}$$

where for convenience we have defined scaled quantities $f \equiv f_d/f_{d*}$ and $C_* \equiv f_{d*} C$, and again assumed the zero-sound-speed case $a = 0$. Note that, since f increases outward from unity at the surface, the surface radius R_* now represents

a critical point (a.k.a. choke or throat) that fixes the required minimal value of $C_* = C_c = 1/\alpha^\alpha(1-\alpha)^{1-\alpha}$ to allow an accelerating solution from this wind base. Accounting then for the mass loss rate scaling of $C_* \sim 1/\dot{M}^\alpha$, we readily see that the net result is to reduce the maximal allowed mass loss to

$$\dot{M}_{fd} = f_{d*}^{1/\alpha}\dot{M}_{CAK} = \dot{M}_{CAK}/(1+\alpha)^{1/\alpha}\,. \tag{4.35}$$

This thus provides a simple rationale for this aspect of the detailed numerical solutions of Friend and Abbott (1986) and Pauldrach et al. (1986).

As the finite-disk factor increases from its reduced base value, the lower mass loading allows for stronger CAK line-force, with now the resulting greater acceleration being "leveraged" by its effect in further increasing the line-force. From the graphical solution in figure 6, one sees that a modest increase in the line-acceleration term $[C(w')^\alpha]$ above the critical solution (with $C = C_c$) leads to a solution with a *much* larger scaled acceleration w'. (There also arises a much shallower acceleration, but as discussed by Feldmeier & Shlosman (2000), maintaining this beyond the critical point requires a special kind of outer boundary condition, whereas the more rapid acceleration is compatible with the standard assumption of simple expansion into a vacuum.)

Figure 8 illustrates this strong sensitivity to the finite-disk correction in terms of $\sqrt{w'}$, which sets the scaling of terminal speed $v_\infty \sim v_{esc}\sqrt{w'}$. Note how the modest, less-than-factor-two change in f leads to large increases in this speed scale $\sqrt{w'}$, with the trends being most dramatic for the largest α. From eqn. (4.34), we see that in the limit of large acceleration $w' \gg 1$, the speed scaling approaches the form

$$\sqrt{w'} \sim C_c f^{1/2(1-\alpha)} \;\;;\;\; w' \gg 1\,, \tag{4.36}$$

which is illustrated through the dashed curves in figure 8. For the specific case $\alpha = 1/2$, we can use the quadratic formula to obtain a simple expression that applies to the full range,

$$\sqrt{w'} = f\left[1 + \sqrt{1 - 1/f^2}\right]\,, \tag{4.37}$$

where the choice of the "plus" root gives the steeper of the two acceleration solutions.

To obtain specific values for the flow speed, we can numerically integrate the scaled equation of motion (4.34) accounting for the complex functional dependence of the finite disk factor (4.33) on radius, velocity, and velocity gradient. The left panel in fig. 9 shows how the ratio of terminal to escape speed depends on the CAK power index α; the right panel plots the full radial variation of velocity for the $\alpha = 0.6$ case. The dashed curves compare results for a similar integration when a canonical beta velocity law is used to evaluate the finite-disk factor. For $\beta = 0.75$ the curves are indistinguishable from the full calculation, and other values of β also give very good approximations.

A basic conclusion is thus that one may derive accurate finite-disk-corrected wind solutions using a beta velocity law to obtain spatially explicit approximations

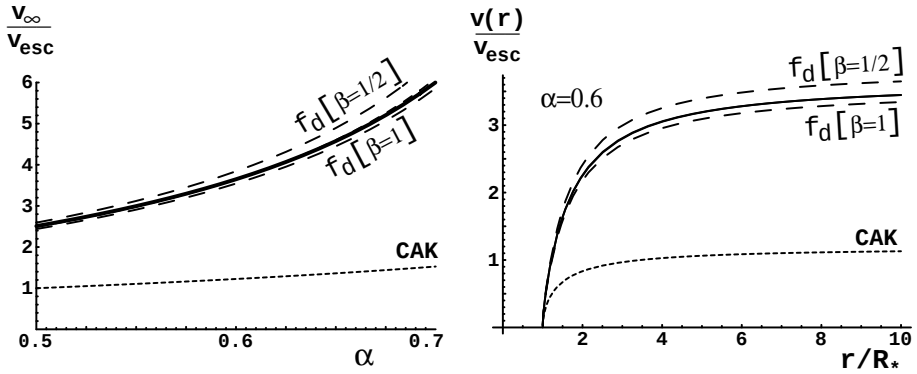

Fig. 9. Comparison of the full finite-disk solutions (solid) with integrations that use a beta-velocity law to obtain spatially explicit approximations for the finite-disk factor (dashed). Left: The ratio of terminal to escape speed vs. CAK exponent α. Right: Radial variation of the velocity for the $\alpha = 0.6$ case. In both panels, results for a model using $\beta = 3/4$ to evaluate the finite-disk factor are also included, but are indistinguishable from the full solution plotted by the solid line. The dotted curves show corresponding results for the point-star CAK model.

of the finite-disk factor, with especially good agreement obtained for $\beta \approx 0.75$. In addition, the finite-disk mass loss rate is reduced by a factor $(1+\alpha)^{-1/\alpha}$ compared to the point-star CAK scaling of eqn. (4.31).

4.3.3 Ionization Correction Factor

The above analysis assumes the line-driving parameters $\overline{Q}$ and α are fixed constants throughout the wind. To account for potential radial variations in line-driving associated with radial variations in the competition between photoionization and radiative recombination, Abbott (1982) introduced the ionization correction factor

$$h(r) \sim \left[\frac{n_e}{W}\right]^{\delta}, \tag{4.38}$$

where n_e is the electron density, the exponent has a typical value $\delta \approx 0.1$, and $W = 0.5(1-\mu_*)$ is the core-radiation dilution-factor, with $\mu_* \equiv \sqrt{1 - R_*^2/r^2}$. Using the mass-continuity equation, the radial variation of this ionization correction can be written as

$$h(r) = \left[(1 + \mu_*(r))\, \frac{v_c}{v(r)}\right]^{\delta}, \tag{4.39}$$

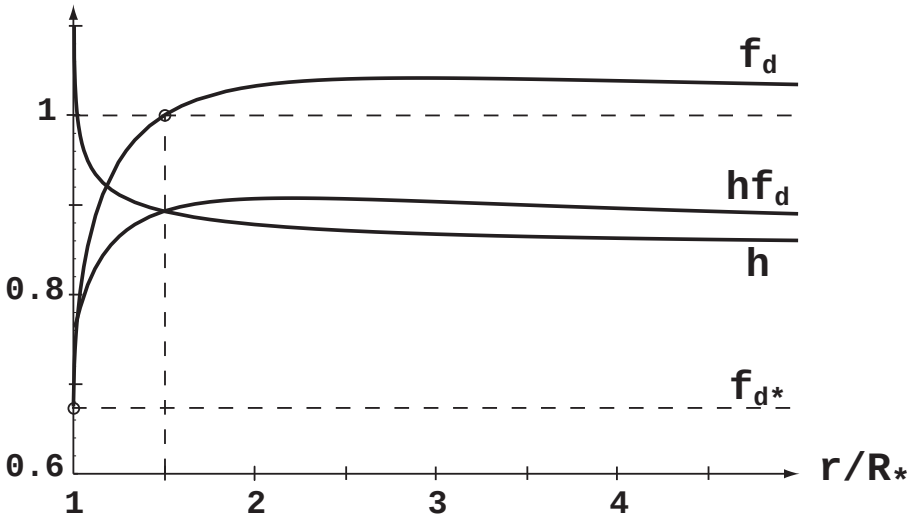

Fig. 10. Comparison of the radial variations of the finite-disk correction factor $f(r)$, the ionization correction factor $h(r)$ for $\delta = 0.1$, and their product $h(r)f(r)$, assuming a 'beta' velocity law $v(r) = v_\infty(1 - R_*/r)^\beta$, taking here $\beta = 1/2$.

where we have normalized to have $h = 1$ at a characteristic critical speed v_c. As illustrated in figure 10, this is a decreasing function of radius, and as such acts to counter the outward increase in line-driving associated with the finite-disk correction. Thus, to take account of these ionization effects in the above analysis of the steepness of wind solutions, we can simply replace the f with hf in eqn. (4.34). The net upshot is that appropriate values of hf are smaller, thus implying somewhat weaker values for the gravity-scaled acceleration w'. This is generally consistent with the lower wind accelerations and lower wind terminal speeds found in such models with a non-zero δ. Since the scaling of the line force with density is now $g_{CAK} \sim 1/\rho^{\alpha-\delta}$, the CAK mass loss rate scalings given by eqn. (4.31) still apply if the α parameter in the exponent is replaced with $\alpha' \equiv \alpha - \delta$.

4.3.4 Correction for Finite Sound Speed

Let us next consider the effect of a finite gas pressure associated with a non-zero sound speed. Historically, there has been considerable debate on the role of gas pressure in line-driven winds, particularly in regards to the mathematical analysis of critical points. For example, in the original CAK point-star analysis, the gas pressure was added to break the degeneracy of the critical condition for the zero-sound-speed limit. More generally, in both point-star and finite-disk models, the critical point is not at the sonic point, and this even led to some initial doubts about the basic validity of the whole CAK/Sobolev approach.

To give a physical perspective to these mathematical subtleties, let us focus

here on the relative magnitude of gas pressure effects within the steady-state, radial equation of motion (cf. eqn. 2.12) for a line-driven stellar wind

$$\left(1 - \frac{a^2}{v^2}\right) v\frac{dv}{dr} = -\frac{GM(1-\Gamma)}{r^2} \; + \; g_{fd} + \frac{2a^2}{r} + \frac{da^2}{dr}\,, \tag{4.40}$$

We first note that, because in hot-star winds the dominant competition between radiative heating and cooling enforces a nearly isothermal condition, we can quite generally ignore the sound-speed gradient term. The remaining gas pressure term on the right-hand-side scales as $4sr/R_*$ relative to the effective gravity, where $s \equiv (a/v_{esc})^2$, with v_{esc} again the effective escape speed from the stellar surface. Since in hot-star winds, $s \approx 0.001$, it is clear that this term is of negligible importance relative to the line-forces that must overcome gravity to drive the outward wind acceleration.

On the left-hand-side, the sound speed factor allows for smooth mapping of the subsonic wind base onto a hydrostatic atmosphere, while also reducing the effective inertia in the moderately supersonic flow. In the global wind that reaches speeds comparable to the escape speed, $v \approx v_{esc} \gg a$, its importance is limited to a relatively small region at the base of the wind near the stellar surface; but through the interaction with the steep decline of finite-disk factor this can modify the maximum mass loss that can be driven from the base.

In the zero-sound-speed limit considered above, the minimal value of the finite-disk-correction factor, $f_{d*} = 1/(1+\alpha)$, occurs near the stellar surface, $r \to R_*$, and this sets the critical conditions that determine the maximal allowed steady mass loss rate, $\dot{M}_{fd}$. But with a finite sound speed, the reduced effective inertia in the base region near the sonic point shifts this critical location for most difficult driving slightly away from the surface wind base. Then, because of the somewhat larger finite-disk factor, this in turn allows a somewhat larger maximal mass loss rate.

To estimate the net effect on the above zero-pressure scalings for the mass loss rate and flow speed, we can apply an analytic, *perturbation expansion* in the small parameter s. For an isothermal wind driven by the finite-disk CAK line-force, let us write the equation of motion (4.40) in the dimensionless form (cf. eqn. 4.34),

$$F(x, w, w') \equiv (1 - s/w)\, w' + 1 - \frac{f}{(1+\delta m_s)^\alpha} C_c (w')^\alpha - 2s/(1-x) = 0\,, \tag{4.41}$$

where

$$\delta m_s \equiv \frac{\dot{M}_{fd,fs}}{\dot{M}_{fd}} - 1 \tag{4.42}$$

is the fractional correction of the mass loss rate due to this small, but non-zero s. The new critical point where this mass loss is fixed now occurs somewhat away from the surface, $x_c > 0$, but in the usual cases that $s \ll 1$, we expect both $\delta m_s \ll 1$ and $x_c \ll 1$.

In the narrow region from the sonic point to this critical point, the driving is dominated by the need to overcome gravity. This implies an outward acceleration

that scales as the inward gravity, namely $w'(x) \approx w'_c = \alpha/(1-\alpha)$, which in turn implies that the velocity in this initial region nearly follows the standard CAK ("beta=1/2") solution, $w(x) \approx w'_c x$. Using this, we obtain a spatially explicit form for the finite-disk factor, which upon expansion to first order in $x \leq x_c \ll 1$ becomes

$$f(x) \approx 1 + 4x\,. \tag{4.43}$$

We then find the equation of motion (4.41) takes the spatially explicit form

$$F(x) = \frac{(1-\alpha)s}{x} + 4x - \alpha\,\delta m_s + 2s = 0\,, \tag{4.44}$$

where we have also expanded $1/(1+\delta m_s)^\alpha$ and kept terms to first order in the smallness parameter s. The critical point is located where this function has a spatial minimum,

$$0 = \left[\frac{dF}{dx}\right]_c = 4 - \frac{(1-\alpha)s}{x_c^2}\,, \tag{4.45}$$

which solves to

$$x_c \approx \sqrt{(1-\alpha)s}/2\,. \tag{4.46}$$

Applying this in eqn. (4.44) and keeping only the leading term of order $\sqrt{s}$, we find the mass loss correction is given by

$$\delta m_s \approx \frac{4\sqrt{1-\alpha}}{\alpha}\,\frac{a}{v_{esc}}\,. \tag{4.47}$$

Beyond this critical point, the increase in the finite-disk factor means that solutions to the equation of motion quickly approach their large gradient limit, $w'^{1-\alpha} \approx fC^c/(1+\delta m_s)^\alpha$. (See dashed curves in figure 8.) Since the wind terminal speed scales as $v_\infty \sim \sqrt{w'}$, this implies that the fractional speed corrections from a finite sound speed should scale as

$$\delta v_{\infty,s} \equiv \frac{v_{\infty,s}}{v_{\infty,s=0}} - 1 \approx (1+\delta m_s)^{-\alpha/2(1-\alpha)} - 1 \approx \frac{-\alpha\delta m_s}{2(1-\alpha)} \approx \frac{-2}{\sqrt{1-\alpha}}\,\frac{a}{v_{esc}}\,. \tag{4.48}$$

For a typical case with $\alpha = 1/2$ and $s = 0.001$, we find $x_c \approx 0.012$, $\delta m_s \approx 0.18$, and $\delta v_{\infty,s} \approx -0.09$. For the same s but $\alpha = 0.7$, we get $\delta m_s \approx 0.10$ and $\delta v_{\infty,s} \approx -0.12$.

In a broad physical context, neglect of gas pressure seems of relatively modest importance compared to other approximations inherent in modelling line-driven mass loss. Relative to the finite-disk, zero-pressure scaling relations, the net effect is to increase the mass loss rate and decrease the wind terminal speed, both by about 10%.

4.3.5 The Wind-Momentum-Luminosity Relation

An important success of these CAK scaling laws is the theoretical explanation they provide for an empirically observed "Wind-Momentum-Luminosity" (WML) relation. Combining the CAK mass-loss law (4.31) together with the scaling of the

terminal speed v_∞ with the effective escape speed $v_{esc} = \sqrt{2GM_*(1-\Gamma_e)/R_*}$, we obtain a WML relation of the form,

$$\dot{M} v_\infty \sqrt{R_*} \sim L_*^{1/\alpha'} Q^{1/\alpha'-1} \,, \tag{4.49}$$

wherein we have neglected a residual dependence on $M_*(1-\Gamma_e)$ that is generally very weak for the usual case that α' is near 2/3. Stellar mass loss rates can be routinely derived by fits to the observed Balmer (Hα) line emission, and wind terminal speeds can be inferred from the blue edge of observed P-Cygni-profiles. Combined with spectroscopic estimates of the stellar luminosity and radius (the latter of which in any case enters only weakly as a square root), empirical fits for a large sample of galactic OB supergiants have demonstrated a remarkably tight agreement with a single WML relation. These fits give a luminosity slope that implies $\alpha' \approx 0.57$, and an overall normalization that is quite consistent with the expectation that $\overline{Q} \approx 10^3$.

Less extensive fits have also been derived for OB stars in the Magellanic clouds. These are each separately consistent with a single WML relation, but with a lower normalization, especially for the small cloud. This likely just reflects the weaker radiative driving from the lower metallacity Z, since the line opacity normalization varies in direct proportion to the metallicity, $\overline{Q} \sim Z$. There are currently efforts toward carefully calibrating this WML relation and its dependence on metallicity. The ultimate goal is to apply observationally inferred wind parameters of luminous hypergiant stars in external galaxies as an alternative "standard candle" for extragalactic distance measurements. In this way hot-star winds may play a role in calibrating the distance scale of the universe.

4.4 Summary for Line-Driven, OB-Star Winds

- The large ratio of luminosity to mass means OB stars are near the "Eddington limit", for which the radiative force from just scattering by free electrons nearly cancels the stellar gravity.

- The resonance nature of line absorption by bound electrons makes their cumulative effective opacity of order a thousand times larger than free electrons, but the discrete energies of bound states means the opacity is tuned to very specific photon wavelengths.

- In a static atmosphere, saturation of line absorption keeps the associated force smaller than gravity; but in an accelerating wind, the associated Doppler shift of the line-frequency exposes it to fresh continuum radiation, allowing the line-force to become strong enough to overcome gravity and drive the outflow.

- Because lines have a thermally broadened velocity width ($v_{th} \lesssim a$) much less than the wind flow speed ($v \approx v_{esc}$), the absorption or scattering of photons in such an accelerating wind occurs over a narrow resonance layer (of width $l_{sob} = v_{th}/(dv/dr) \approx (v_{th}/v_{esc})R_*$); following methods introduced

by V. V. Sobolev, this allows nearly local solution of the line-transfer in such accelerating flow.

- Within the CAK model for a power-law distribution of line strengths, the cumulative line-force scales with a power of the local velocity gradient divided by the density.
- For the idealized case of negligible gas pressure and a radially streaming point-source of stellar radiation, application of this CAK line-force within a steady-state radial equation of motion yields analytic scalings for the mass loss rate and wind velocity law.
- Accounting for the finite cone-angle of the stellar disk and radial ionization balance variations in the driving opacity yield order unity corrections to the point-star scalings. Corrections for a finite gas pressure are smaller, of order 10%.
- Overall, the predictions of the CAK scalings agree well with an observationally inferred wind-momentum-luminosity relation for OB supergiants.

5 Wolf-Rayet Winds and Multi-line Scattering

The above CAK model is based on a simplified picture of absorption of the star's radiative momentum by many *independent* lines, effectively ignoring overlap effects among optically thick lines. Since each such thick line sweeps out a fraction v_∞/c of the star's radiative momentum L_*/c, the ratio of wind to radiative momentum is

$$\eta \equiv \frac{\dot{M} v_\infty}{L_*/c} = N_{thick} \frac{v_\infty}{c} \,, \tag{5.1}$$

which is sometimes termed the wind "momentum" or "performance" number. To avoid overlap, we must require $N_{thick} < c/v_\infty$, which in turn implies the so-called "single-scattering" limit for the wind momentum, $\eta < 1$. Since most OB winds are inferred to be below this limit, the basic CAK model ignoring overlap still provides a reasonably good model for explaining their overall properties.

However, such a single-scattering formalism seems quite inadequate for the much stronger winds of Wolf-Rayet (WR) stars. Wolf-Rayet stars are evolved, massive, hot stars for which the cumulative mass loss has led to depletion of the original hydrogen envelope. They typically show broad wind-emission lines of elements like carbon, nitrogen, and/or oxygen that are the products of core nucleosynthesis. Overall, observations indicate that WR winds are especially strong, and even optically thick to continuum scattering by electrons. Notably, inferred WR wind momenta $\dot{M} v_\infty$ are generally substantially higher than for OB stars of comparable luminosity, placing them well above the OB-star line in the above Wind-Momentum-Luminosity relation. In fact, in WR winds the inferred momentum numbers are typically well above the single-scattering value $\eta = 1$, sometimes as high as $\eta = 10 - 50$!

This last property has often been cast as posing a WR wind "momentum problem", sometimes with the implication that it means WR winds cannot be radiatively driven. In fact, it merely means that, unlike for OB stars, WR winds cannot be treated in the standard, single-scattering formalism. However, momentum ratios above unity can, in principle, be achieved by *multiple scattering* between overlapping thick lines with a velocity-unit frequency separation $\Delta v < v_\infty$. Figure 11 illustrates this for the simple case of two overlapping lines. But, as we review below, the large momentum of WR winds requires much more extensive overlap, with thick lines spread densely throughout the spectrum without substantial gaps that can allow radiation to leak out. An overall theme here is that understanding WR mass loss represents more of an "opacity" than a "momentum" problem.

5.1 Example of Multiple Momentum Deposition in a Static Gray Envelope

To provide the basis for understanding such multi-line scattering, it is helpful first to review the momentum deposition for *continuum* scattering. The total radial momentum imparted by radiation on a spherically symmetric circumstellar envelope can be expressed in terms of the radiative force density ρg_{rad} integrated

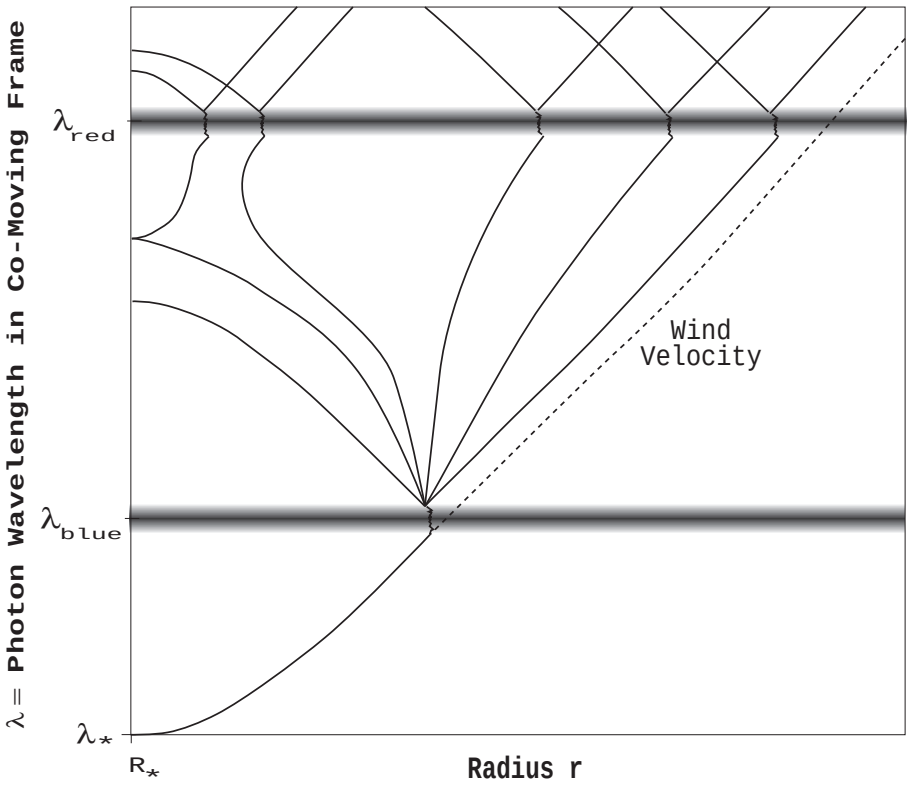

Fig. 11. The Doppler-shifted line-resonance in an accelerating flow, now for two lines with relative wavelength separation $\Delta\lambda/\lambda < v_\infty/c$ close enough to allow multi-line scattering within the wind. Photons scattered by the bluer line are reemitted with nearly equal probability in the forward or backward directions, but then further red-shifted by the wind expansion into resonance with the redder line. Because of the gain in radial direction between the line resonances, the red-line scattering imparts an additional component of outward radial momentum.

over volume, outward from the wind base at radius R_*,

$$\dot{p}_{rad} = \int_{R_*}^{\infty} 4\pi r^2 \rho g_{rad} dr, \tag{5.2}$$

where the radiative acceleration is given by a frequency integral of the opacity κ_ν over the stellar flux spectrum, F_ν, (cf. eqn. 4.2)

$$g_{rad} = \int_0^{\infty} \frac{\kappa_\nu F_\nu}{c} d\nu \tag{5.3}$$

A particularly simple way to illustrate the requirements of multiple momentum deposition is in terms of an envelope with a *gray* opacity κ. In this case, the flux

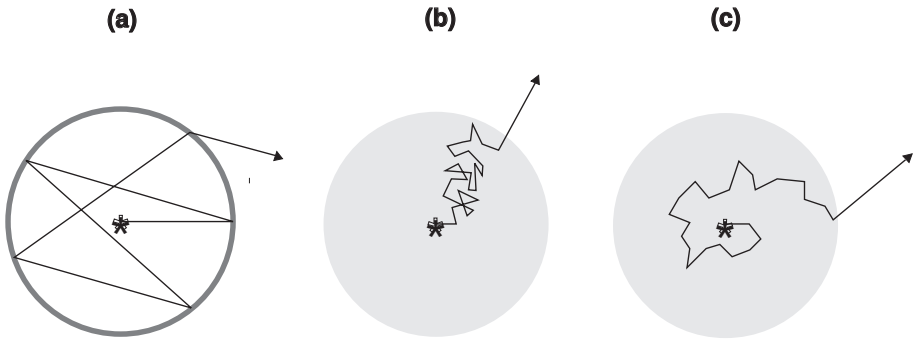

Fig. 12. Schematic photon trajectories in (a) hollow and (b) filled gray spheres, with part (c) illustrating the net "winding" that makes even the filled case have a persistent net outward push that implies multiple radial momentum deposition. See text for details.

is just a constant in frequency, set at each radius by the bolometric luminosity through $F = L/4\pi r^2$. This implies $g_{rad} = \kappa L/4\pi r^2 c$, and so yields

$$\dot{p}_{rad} = \frac{L}{c}\int_R^\infty \kappa\rho dr = \frac{L}{c}\tau, \tag{5.4}$$

where τ is the total wind optical depth. We thus see that the requirement for exceeding the single scattering limit for radiative momentum deposition, $\dot{p}_{rad} > L/c$, is simply that the envelope be optically thick, $\tau > 1$.

Figure 12 provides a geometric illustration of how multiple momentum deposition occurs in an optically thick envelope. Figure 12a shows the case of a hollow shell with optical thickness $\tau = 5$, wherein a photon is backscattered within the hollow sphere roughly τ times before escaping, having thus cumulatively imparted τ times the single photon momentum, as given by eqn. (5.4).

However, the same momentum deposition also occurs in a *solid* sphere with the same total optical depth, even though, as shown in figure 12b, photons in this case undergo a much more localized diffusion without hemispheric crossing.

Figure 12c illustrates how these diffusive vs. direct-flight pictures of multiple momentum deposition can be reconciled by thinking in terms of an effective "winding"around the envelope. For each scattering within a spherical envelope the radial momentum deposition is unchanged by arbitrary rotations about a radius through the scattering point. For figure 12c the rotations are chosen to bring all the scattered trajectories into a single plane, with the azimuthal component always of the same sense, here clockwise viewed from above the plane. In this artificial construction, scattering thus leads to a *systematic* (vs. random walk) drift of the photon along one azimuthal direction, implying a cumulative *winding* trajectory for which the systematic *outward* push of the scattered photon is now apparent.

5.2 Multi-Line Transfer in an Expanding Wind

The multiple scattering by a dense ensemble of lines can actually be related to the above gray envelope case, *if* the spectral distribution of lines is Poisson, and so is spread throughout the spectrum without extended bunches or gaps. As first noted by Friend and Castor (1983), and later expanded on by Gayley *et al.* (1995), a wind driven by such an effectively gray line-distribution can be analyzed through an extension of the above standard CAK formalism traditionally applied to the more moderate winds of OB stars. In the case of dense overlap, wherein optically thick lines in the wind have a frequency separation characterized by a velocity Δv much less than the wind terminal speed v_∞, the mean-free-path between photon interactions with separate lines is given by

$$\frac{1}{\rho\kappa^{eff}} = \frac{\Delta v}{dv_n/dn}, \tag{5.5}$$

where $dv_n/dn \equiv \hat{\mathbf{n}} \cdot \nabla(\hat{\mathbf{n}} \cdot \mathbf{v})$ is the projected wind velocity gradient along a given photon direction $\hat{\mathbf{n}}$ (see §4.2.6). The directional dependence of this velocity gradient implies an inherent *anisotropy* to the associated effectively gray line-ensemble opacity κ^{eff}. However, a full non-isotropic diffusion analysis (Gayley *et al.* 1995) indicates that the overall wind dynamics is not too sensitive to this anisotropy. In particular, the total wind momentum can still be characterized by the effective *radial* optical depth, τ_r^{eff}, which in this case yields,

$$\dot{p}_{rad} \approx \frac{L}{c}\tau_r^{eff} = \frac{L}{c}\int_R^\infty \rho\kappa_r^{eff} dr = \frac{L}{c}\int_R^\infty \frac{1}{\Delta v}\frac{dv_r}{dr} dr = \frac{L}{c}\frac{v_\infty}{\Delta v}, \tag{5.6}$$

from which we identify $\tau_r^{eff} = v_\infty/\Delta v$. Neglecting a modest correction for gravitational escape, global momentum balance requires $\dot{p}_{rad} \approx \dot{M} v_\infty$, thus implying

$$\eta \approx \frac{v_\infty}{\Delta v}. \tag{5.7}$$

For winds driven by a gray ensemble of lines, we thus see that large momentum factors $\eta \gg 1$ simply require that there be a large number of optically thick lines overlapping within the wind, $v_\infty \gg \Delta v$.

Note that eqn. (5.7) implies that the mass loss scales as

$$\dot{M} \approx \frac{L}{c^2}\frac{c}{\Delta v}, \tag{5.8}$$

wherein we note that $c/\Delta v$ just represents the total, spectrum-integrated number of thick lines, N_{thick}. It is important to realize, however, that this number of thick lines is not fixed *a priori*, but is itself dependent on wind properties like the mass loss rate and velocity law.

Self-consistent solution is again possible though through an extension of the standard CAK formalism. The key is to account for the fact that radiation entering into resonance of each line does not in general come directly from the stellar

core, but instead has been previously scattered by the next blueward overlapping line. In the limit of strong overlap, the transfer between lines can be treated as local diffusion, using however a non-isotropic diffusion coefficient to acccount for the directional variation of the velocity gradient. In analogy to the finite-disk correction for point-star CAK model, one can then derive a "non-isotropic diffusion" correction factor, f_{nid}, to account for the diffuse angle distribution of the previously line-scattered radiation as it enters into resonance with then next line. With this factor, one again finds that the mass loss follows a standard CAK scaling relation (4.31)

$$\dot{M} = f_{nid}^{1/\alpha} \dot{M}_{cak} = f_{nid}^{1/\alpha} \frac{L}{c^2} \frac{\alpha}{1-\alpha} \left[\frac{\bar{Q}\Gamma}{1-\Gamma} \right]^{(1-\alpha)/\alpha} . \tag{5.9}$$

where $f_{nid}^{1/\alpha}$ is typically about one half. (See fig. 6 of Gayley *et al.* 1995.)

The wind velocity law in such multi-scattering models is found to have a somewhat more extended acceleration than in standard finite-disk CAK models, with velocity law indexes of roughly $\beta = 1.5 - 2$. The terminal speed is again scales with the effective escape speed, $v_\infty \approx 3 v_{esc}$.

This analysis shows that, within such "effectively gray" distribution of overlapping lines, multiline scattering can, in principle, yield momentum numbers $\eta \gg 1$ well in excess of the single-scattering limit. In this sense, there is thus no fundamental "momentum" problem for understaneding WR winds.

5.3 Wind-Momentum-Luminosity Relation for WR Stars

As noted above (§4.3.5), this CAK mass-loss law together with the tendency for the terminal speed v_∞ to scale with the effective escape speed v_{esc} implies the Wind-Momentum-Luminosity relation (4.49). Fits for galactic OB supergiants (Puls et al. 1996) give a luminosity slope consistent with $\alpha \approx 0.6$, with a normalization implying $\overline{Q} \approx 10^3$.

For WR stars, such comparisons of wind momentum vs. luminosity show a much greater scatter, but with momenta consistently above those inferred for OB stars, typically reflecting more than a factor 10 higher mass loss rate for the same luminosity (Hamman *et al.* 1995). If we assume the same $\alpha \approx 0.6$ that characterizes OB winds, eqn. (4.49) suggests that WR winds must have a line opacity normalization $\overline{Q}$ that is more than a factor $\approx 10^{\alpha/(1-\alpha)} \approx 30$ higher! Alternatively, this enhanced mass loss could also be obtained through a slightly lower α, representing a somewhat flatter number distribution in line opacity. For example, for stars with Eddington parameter $\Gamma \approx 1/2$ and O-star value for $\overline{Q} \approx 10^3$, simply decreasing from $\alpha = 0.6$ to $\alpha = 0.5$ yields the required factor $\overline{Q}^{1/0.5-1/0.6} \approx 10$ increase in $\dot{M}$.

While such a modest reduction in α may seem more plausible than a large increase in $\overline{Q}$, it is generally not clear what basic properties of WR winds could lead to either type of change in the line opacity distribution. In this context, it thus seems useful here to distinguish the classical *momentum* problem of achieving the

large inferred WR momentum numbers, from an *opacity* problem of understanding the underlying sources of the enhanced line opacity needed to drive the enhanced mass loss of WR winds. The wind-momentum vs. luminosity relation given in eqn. (4.49) yields a scaling of wind momentum numbers with $\eta \sim L_*^{1/\alpha-1} \sim L_*^{2/3}$, implying that even OB winds should have large momentum numbers, even exceeding the single scattering limit, for a sufficently large luminosity. Viewed in this way, the fundamental distinguishing characteristic of WR winds is not so much their large momentum number, but rather their enhanced mass loss compared to OB stars with similar luminosity. Identifying the sources of the enhanced opacity required to drive this enhanced mass loss thus represents a fundamental, unsolved "opacity problem".

5.4 Cumulative Co-Moving-Frame Redshift from Multi-line Scattering

One can also view this multi-line scattering that occurs in a WR wind as a random walk over wind *velocity*. To achieve the rms target velocity v_∞ in random increments of Δv requires stepping through $(v_\infty/\Delta v)^2$ lines. Since the expected net redshift from each line interaction is of order $\Delta v/c$, photons undergo a cumulative redshift $\Delta E/E \approx (v_\infty^2/\Delta v^2)\Delta v/c$ over the course of their escape. The associated radial momentum deposition factor is $\eta \approx (\Delta E/E)(c/v_\infty) \approx v_\infty/\Delta v$, as found above.

Figure 13 illustrates the comoving-frame redshift for a typical photon as it diffuses in radius due to multi-line scattering. The photon track shown is a characteristic result of a simple Monte Carlo calculation for a wind velocity law $v(r) = v_\infty(1 - R_*/r)$ and a constant line spacing $\Delta v = v_\infty/10$. Each of the nodes shown represents scattering in one line. In this specific case, the photon escapes only after interacting with nearly 90 lines, resulting in cumulative redshift of nearly $9v_\infty/c$. These are near the statistically expected values of $(v_\infty/\Delta v)^2 = 100$ line scatterings resulting in a total redshift $v_\infty^2/c\Delta v = 10v_\infty/c$, as given by the above random walk arguments.

This systematic photon redshift can also be related to the energy loss – or photon "tiring" – that results from the *work* the radiation does to accelerate the wind to its terminal speed v_∞. The ratio of wind kinetic energy to the radiative energy represents a "kinetic tiring number"

$$m_{kin} = \frac{\dot{M} v_\infty^2}{2L_*} = \eta \frac{v_\infty}{2c} \,. \tag{5.10}$$

Since typically $v_\infty/c < 0.01$, we see that for WR winds with momentum numbers of order $\eta \approx 10$, photon tiring is only a $\sim$5% effect. Although thus not of much significance for either OB or WR winds, photon tiring does represent a fundamental limit to mass loss, with implications for understanding the giant eruptions from Luminous Blue Variable (LBV) stars. We return to this in §6, which deals with continuum driven mass loss for stars near or above the Eddington limit.

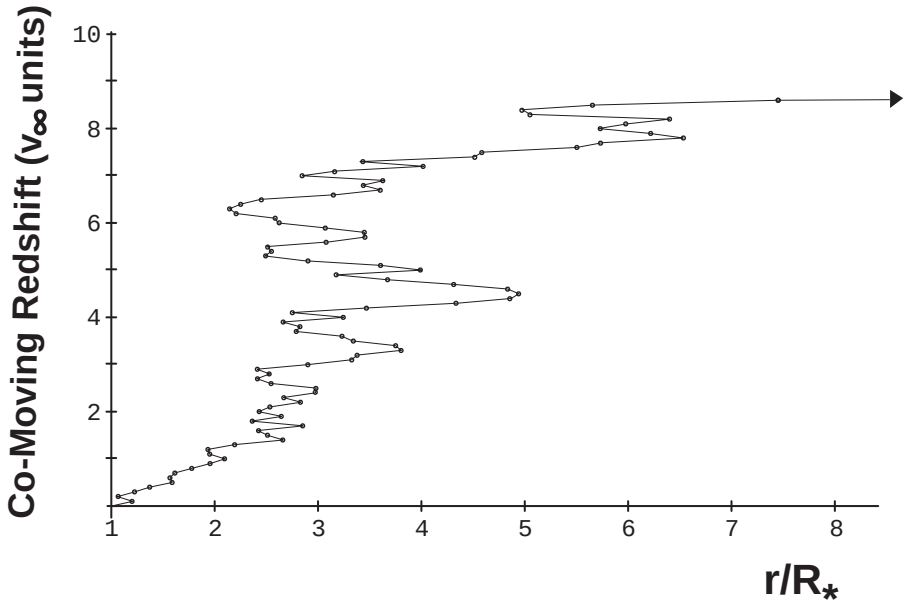

Fig. 13. Simulated photon redshift in the comoving frame as a photon executes a random walk through the wind. The adopted line density is $v_\infty/\Delta v = 10$, which because of the random walk character, implies the photon will interact with roughly 10^2 different lines during escape. Since the comoving redshift between scatterings is $v_\infty/10$, this implies a total comoving redshift of 10 v_∞.

5.5 Role of Line Bunches, Gaps, and Core Thermalization

An essential complication for developing realistic models of WR winds stems from the inherently non-Poisson character of the spectral line distributions derived from atomic databases of line lists. At any given wind radius, the dominant contribution to the line opacity stems from a surprisingly small number of specific ionization stages of abundant heavy metals, primarly iron and iron-group elements. Moreover, for any given ion stage, the term structure is such that the lines are notably "bunched" into relatively restricted ranges of wavelength. With just a small number of distinct ion stages, the cumulative line spectrum thus likewise exhibits extensive wavelength bunching. Within the gaps between these bunches, the radiation can propagate relatively unimpeded by line-scattering, thus representing a potential preferential "leakage" that can significantly reduce the global radiative momentum deposition.

To provide a physical perspective it is helpful to return to the above concept that the line-ensemble constitutes an effective *continuum* opacity, but now allowing this to be frequency dependent to account for the relative bunches and gaps in the spectral distribution of lines. As seen from eqn. (5.3), the radiative acceleration

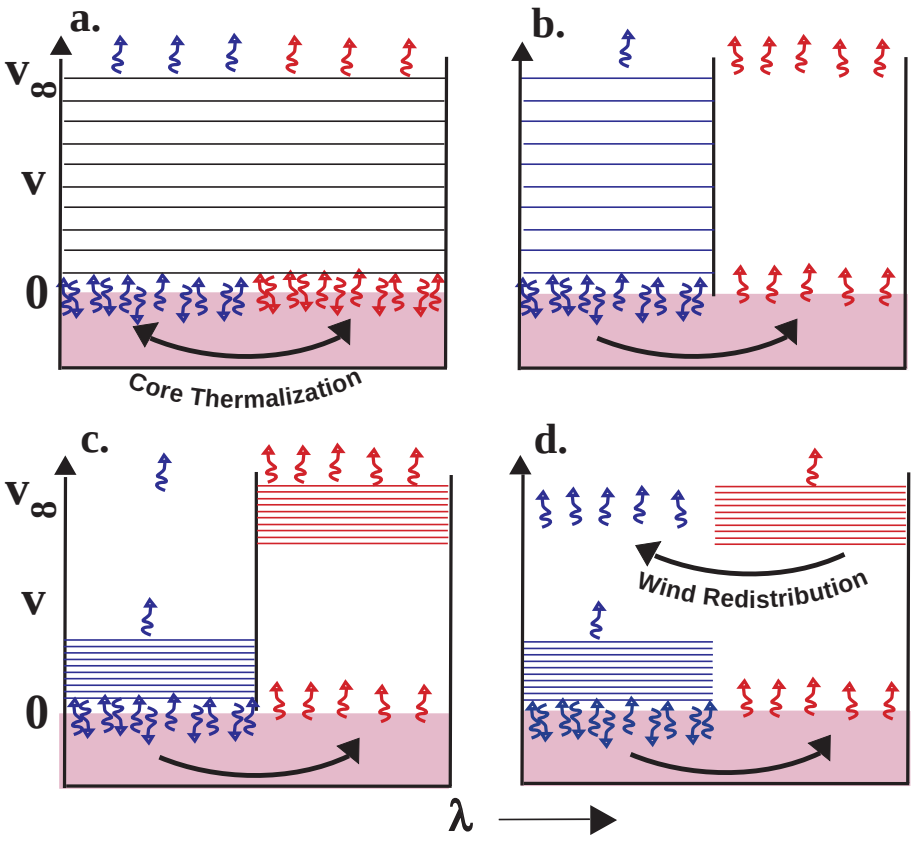

Fig. 14. Schematic diagram illustrating the role of line gaps, line bunches, and photon thermalization for WR wind momentum deposition. The horizontal lines represent the velocity/frequency spacing of optically thick lines in the wind. The four parts represent: (a.) an effectively gray model (b.) a wind with fixed ionization and extensive gaps (c.) a wind with ionization stratification that fills gaps (d.) the importance of limiting energy redistribution in the wind.

for such a non-gray opacity depends on the spectral integral of the opacity times the *frequency-dependent* radiation flux. In general the flux spectrum at any given location in an atmosphere or wind depends on self-consistent solution of a global radiation transport problem, with overall characteristics depending critically on the *thermalization* and frequency *redistribution* properties of the medium.

Figures 14a-d illustrate this key role of photon thermalization and redistribution for simple non-gray line-distributions that are divided locally into two distinct spectral regions, representing either a line "bunch" or "gap". Figure 14a first recaps the effectively gray case in which the entire spectrum is covered by lines

at fixed velocity separation $\Delta v = v_\infty/10$. Since this represents a total effective optical depth $\tau = 10$ for photons to escape from the surface ($v = 0$) to infinity ($v = v_\infty$), the global radiative momentum is $\dot{p}_{rad} = 10L/c$, as follows from eqn. (5.4).

Figure 14b represents the case when lines have the same concentration $\Delta v = v_\infty/10$ in half the spectrum (the bunch), with the other half completely line-free (the gap). Photons blocked in the bunched region are then rethermalized in the stellar core, and so tend to escape though the gap. Simple statistical arguments show that only about $0.5/(1 + \tau/2) = 1/12$ of the total flux now makes it out through the half of the spectrum covered by the bunch, implying from eqn. (5.4) that the total radiative momentum is now only $\dot{p}_{rad}/(L/c) \approx 10\times1/12+0\times11/12 = 5/6 < 1$! This roughly represents the circumstance applicable to OB star winds, which have radially constant ionization, and so a radially fixed line-spectrum. For such winds, we can see that any significant spectral gaps keep the momentum number to near the single scattering limit $\dot{p}_{rad} \approx L/c$, even if there is very extensive line overlap in spectral line bunches.

Figure 14c represents the case wherein there are again $\tau = 10$ lines covering the full spectrum, but now over a limited spatial range, occuring very close to the star in one spectral region, and very far away in the other. In the region where line-blocking occurs near the star, core thermalization again channels photons to the other spectral region. But in this second spectral region, the blocking occurs far away from the star, with greatly reduced probability of backscattering to thermal redistribution in the stellar core. Again assuming purely coherent line-scattering in the wind, this means the flux is nearly independent of the outer wind blocking. Since all the stellar flux must diffuse through a layer somewhere with $\tau = 10$ lines, the global momentum deposition is now again, as in case a, simply $\dot{p}_{rad} = 10L/c$. However, note that the flux distribution is still similar to case b, i.e. in proportion 1/12 and 11/12 to the spectral regions corresponding respectively to the inner and outer wind blocking. This thus implies the same ratio for the relative deposition of radiative momentum. Overall we see that this example, intended to represent the case of an optically thick WR wind with ionization stratification, does indeed illustrate how it is possible to get a large global momentum deposition even when the line-opacity-spectrum is locally divided into gaps and bunches. However, this radiative momentum tends to be deposited more in the outer wind, leaving a net deficit in driving needed to initiate the outflow in the lower wind. This may play a factor in inducing the inferred structure and variability of WR winds.

The final example in figure 14d illustrates the crucial importance of the assumption that the radiative transfer within the wind itself is through pure, coherent scattering. If there is significant thermalization or any other type of spectral energy redistribution within the wind itself, then radiation will always tend to be channeled into local gaps, thus again limiting the momentum deposition to a level roughly characterized by the single scattering limit.

5.6 Summary for Wolf-Rayet Winds

- The classical "momentum problem" (to explain the large inferred ratio of wind to radiative momentum, $\eta \equiv \dot{M} v_\infty / (L/c) \gg 1$) is in principle readily solved through multiple scattering of radiation by an opacity that is sufficiently "gray" in its spectral distribution. In this case, one simply obtains $\eta \approx \tau$, where τ is the wind optical depth.

- Lines with a Poisson spectral distribution yield an "effectively gray" cumulative opacity, with multi-line scattering occuring when the velocity separation between thick lines Δv is less than the wind terminal speed v_∞. In this case, one obtains $\eta \approx v_\infty / \Delta v$.

- However, realistic line lists are not gray, and leakage through gaps in the line spectral distribution tends to limit the effective scattering to $\eta \lesssim 1$.

- In WR winds, ionization stratification helps spread line-bunches and so fill in gaps, allowing for more effective global trapping of radiation, and thus $\eta > 1$.

- However, photon thermalization can reduce the local effectiveness of line-driving near the stellar core, making it difficult for radiation alone to initiate the wind.

- The relative complexity of WR wind initiation may be associated with the extensive turbulent structure inferred from observed variabililty in WR wind emission lines.

- Overall, the understanding of WR winds is perhaps best viewed as an "opacity problem", i.e. identifying the enhanced opacity that can adequately block the radiation flux throughout the wind, and thus drive a WR mass loss that is much greater than from OB stars of comparable luminosity.

6 Waves and Instabilities in Line-Driven Stellar Winds

The steady, radial line-driven wind models decribed in §4 have had considerable success in explaining the inferred general properties of OB-star winds, like the total mass loss rate and mean velocity law. But when viewed more carefully there is substantial evidence that such winds are actually quite highly structured and variable on a broad range of spatial and temporal scales. In this section, we examine small-scale, stochastic structure, with emphasis on its likely origin in the strong "line-deshadowing instabililty" (LDI) that is intrinsic to the line-driving mechanism for hot-star winds.

6.1 Linear, Time-Dependent Perturbation Analysis

As a first step in studying possible time-dependent effects in a wind flow, let us examine the response to small-amplitude, *linear* perturbations in the basic flow variables like density and velocity. Within a background steady, radial wind with velocity $v_o(r)$ that depends only on radius, we assume there are superposed small-amplitude, time-dependent, sinusoidal velocity perturbations $\delta v(r,t) = \delta v e^{i(kr-\omega t)}$, with k the radial wavenumber, and ω and δv the complex frequency and wave amplitude.

In view of the relatively minor dynamical role of gas pressure in driving hot-star winds, let us consider the limit of vanishing pressure/sound-speed. For a time-dependent, radial, radiatively driven flow, the equation of motion with no gas pressure is (cf. eqn. 2.6)

$$\frac{\partial v}{\partial t} + v\frac{dv}{dr} = g_{rad} - \frac{GM}{r^2}\,. \tag{6.1}$$

In the local comoving frame of the mean flow with speed v_o, the linearized, first-order perturbed equation of motion can then be written

$$-i\omega\delta v \approx \delta g_{rad} \tag{6.2}$$

where $\delta g_{rad} = g_{rad}(r,t) - g_{rad,o}(r)$ is the perturbed radiative acceleration, and we have assumed the WKB approximation $k \gg (dv_o/dr)/v_o$ to ignore a mean velocity gradient term. We thus find

$$\omega = i\frac{\delta g_{rad}}{\delta v}\,, \tag{6.3}$$

which shows that the complex frequency response of the perturbation depends on the ratio of perturbed radiative force to perturbed velocity, times a 90^o phase shift factor i. The phase propagation of the wave, which is given by the real part of the frequency, thus depends on the imaginary part of the perturbed force ratio. On the other hand, the real part of this force ratio gives rise to an imaginary component of the frequency, which thus implies either unstable growth or wave damping, depending on whether $\Re(\delta g_{rad}/\delta v)$ and thus $\Im(\omega)$ are positive or negative.

The remaining parts of this section discuss the various physical components of the perturbed radiative force that contribute toward propagation, growth, and damping of such a linear velocity perturbation.

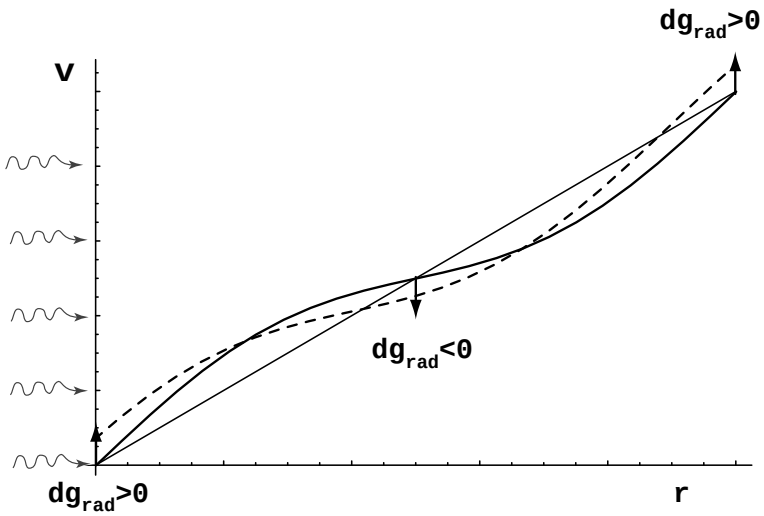

Fig. 15. Illustration of the basic cause of inward propagation of Abbott waves in a line-driven stellar wind. The mean linear increase in velocity has superposed a small-amplitude sinsoidal pertrubation (wavy solid curve). The parts of the perturbation with an increased or decreased velocity gradient have an associated increase or decrease in the line force, as denoted by the up/down vertical arrows. The net effect is to accelerate or decelerate the various parts of the perturbation in such a way that after a short time the overall wave pattern (dashed curve) is shifted inward, *against* the direction of the stellar radiation (wavy arrows at left).

6.1.1 Stable, Propagating Abbott Waves

As a first example, consider the CAK/Sobolev approximation used in §4 for the steady-state wind. If we assume this also applies to the flow perturbation, then the perturbed radiative force scales with the perturbed velocity gradient $\delta v' \equiv d\delta v/dr = ik\delta v$,

$$\delta g_{rad} \approx ik\delta v \, \frac{\partial g_{rad}}{\partial v'} \, . \tag{6.4}$$

Combining eqns. (6.3) and (6.4), we find the frequency is purely real,

$$\omega = -k \, \frac{\partial g_{rad}}{\partial v'} \, . \tag{6.5}$$

Since $\partial g_{rad}/\partial v' > 0$, this represents stable, dispersionless, *inward* wave propagation. First described by Abbott (1980), such propagating solutions are nowadays known as "Abbott waves", with the phase speed $\omega/k = \partial g_{rad}/\partial v' \equiv c_A$ the "Abbott speed". Since the waves are dispersionless, this is also the *group* speed for propagation of a localized perturbation composed with a Fourier spectrum of wavenumbers.

Given that the restoring force for such waves comes from the *outwardly* directed radiative driving, it seems at first peculiar that the net result should be to induce *inward* wave propagation. Figure 15 illustrates an explanation for this. The solid wavy curve represents a small-amplitude sinsoidal velocity perturbation superposed on a constant, mean-wind acceleration. The short vertical arrows indicate the effect of the perturbed radiative driving force, which leads to an enhanced acceleration (upward arrow) at the part of the wave that has a steeper velocity gradient, and decreased acceleration (downward arrow) at the part with shallower gradient. At some short time later the material is variously speeded up or slowed down, following the position of the dashed wavy curve, which has an overall net *inward* phase shift from the earlier wave position.

Abbott (1980) showed also that the associated inward propagation speed is comparable to the outward wind flow speed, which in these highly supersonic winds is much faster than the usual sound speed for gas pressure perturbations. More specifically, he showed that below, at, or above the CAK critical point, this inward wave speed is greater than, equal to, or less than the outward flow speed. This shows that, like the sonic point of a gas-pressure driven wind, the CAK critical point is the outermost wind point from which a net inward propagation of information to the wind base is possible. It thus provides a physical perspective for why conditions at this critical point fix the wind mass loss rate. In analogy with sub- and super-sonic flow, one now speaks of line-driven flow as sub- or super-"Abbottic" depending on whether the speed is below or above the Abbott/CAK-critical speed. Much as the supersonic solar wind solution is the only one that matches the outer boundary condition of a low pressure at large radii (see §3.2), Feldmeier and Shlosman (2002) have recently shown that the super-Abbottic critical solution in line-driven models is the only one compatible with a free vacuum outer boundary condition.

In the point-star, zero-sound-speed CAK model discussed in §4, the *entire wind* equally satisfies the critical condition for maximal mass loss rate (see figure 6 and discussion in §4.3.1.). In this case, the Abbott speed thus exactly equals the mean flow speed throughout the wind. This can be seen explicitly by applying the point-star CAK line-force (4.19)

$$c_A \equiv \frac{\partial g_{rad}}{\partial v'} = \alpha \frac{g_{cak,o}}{v'_o} = \alpha v_o C_c (w'_c)^{\alpha-1} = v_o \,, \tag{6.6}$$

where the latter equalities apply to the mean CAK critical solution derived in §4.3.1. Combining eqns. (6.3) and (6.6) shows such a wave would thus be *stationary* ($w/k + v_o = 0$) in a frame that is fixed relative to the star, reflecting the degenerate, critical nature of the entire wind for such a zero-sound-speed, point-star model.

CAK broke this degeneracy by including the small, finite gas-pressure, but in practice a more physically important effect is the finite-disk correction, which brings the critical point very close to the stellar surface, as discussed in §4.3. In finite-disk, finite-sound-speed models, the flow is thus only sub-Abbottic in this narrow region between the surface and the critical point.

Finally, the stability of these Abbott waves is a direct result of the assumption that the perturbed line-force follows the CAK/Sobolev scaling with velocity gradient. For a sinusoidal velocity perturbation, the gradient has a 90^o phase difference from the perturbed velocity (as signified in the above complex peturbation by the imaginary factor i). Since this means the perturbed line-force is likewise 90^o out of phase with perturbed velocity, it means the force does no net work on the perturbation, which thus implies marginal stability.

6.1.2 Line-Deshadowing Instabillty (LDI)

An alternative perspective, first suggested by Lucy and Solomon (1970) and developed further by MacGregor, Hartmann, and Raymond (1979) and Carlberg (1980), is that the perturbed line-force should instead be proportional to the perturbed *velocity* itself, *not* its gradient. The net work done to amplify the perturbation would then imply a net *instability*.

To see this, let us return to the basic integral expression (4.15) for the line-acceleration resulting from absorption of the direct radiation from a point-source star. Figure 16a plots various components of the integrand vs. comoving frequency $x - u$ (with $u = v(r)/v_{th}$). The net force is proportional to the area under the overlap between the gaussian line-profile and the local intensity on the blue edge. The dashed curve shows the blueward Doppler shift of the line-profile resulting from the local velocity perturbation $\delta u = \delta v/v_{th}$. The resulting "deshadowing" relative to the blue-edge intensity gives the perturbed line-force an increase that scales directly with perturbed velocity

$$\delta g_{rad} = \Omega \delta v \,, \tag{6.7}$$

which when applied in eqn. (6.3) now makes the frequency imaginary

$$\omega = i\Omega \,, \tag{6.8}$$

with the proportionality constant $\Omega > 0$ representing the growth rate of the associated "line-deshadowing instability" (LDI).

The growth rate of this instability is determined by applying the velocity perturbation δv in the line-profile argument of eqn. (4.15) and expanding to first-order,

$$\Omega = \frac{\delta g_{rad}}{\delta v} \approx -\frac{g_{thin}}{v_{th}} \int_{-\infty}^{\infty} dx' \, \frac{d\phi(x')}{dx'} \, e^{-qt\Phi(x')} \tag{6.9}$$

$$= \frac{g_{thin}}{v_{th}} \int_{-\infty}^{\infty} dx' \, 2x' \, \phi(x') e^{-qt\Phi(x')} \tag{6.10}$$

$$\approx 2x_b \, \frac{g_{line}}{v_{th}} \quad ; \quad qt \gg 1 \,, \tag{6.11}$$

where the last equality applies for optically thick lines, with $qt\Phi(x_b) \equiv 1$ defining the blue-edge frequency x_b that characterizes the peak of the force integrand.

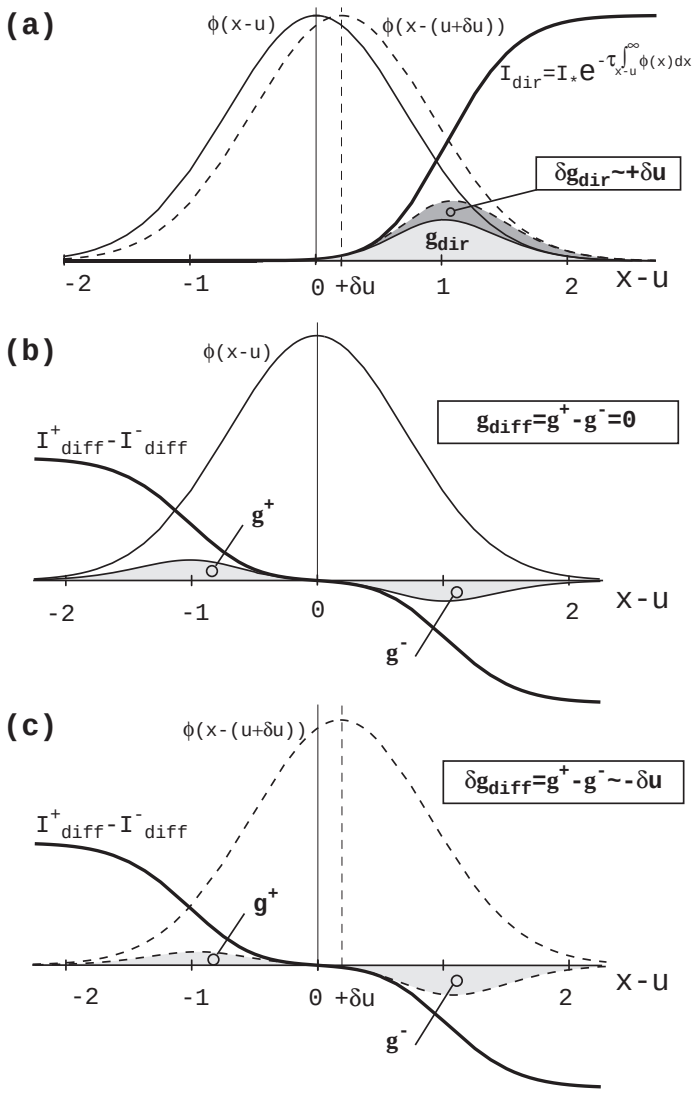

Fig. 16. (a) The line profile ϕ and direct intensity $I_{\rm dir}$ plotted vs. comoving frame frequency $x-u$, with the light shaded overlap area proportional to the net direct line-force g_{dir}. The dashed profile shows the effect of the Doppler shift from a perturbed velocity δu, with the resulting extra area in the overlap with the blue-edge intensity giving a perturbed line-force δ_{rad} that scales in proportion to this perturbed velocity. (b) The comoving-frequency variation of the forward (+) and backward (-) streaming parts of the diffuse, scattered radiation, illustrating the cancelling of the overlap with the line profile that causes the net diffuse force to nearly vanish in a smooth, supersonic outflow. (c) However, because of the Doppler shift from the perturbed velocity, the dashed profile now has a stronger interaction with the backward streaming diffuse radiation. This results in a diffuse-line-drag force that scales with the negative of the perturbed velocity, and so tends to counter the instability of the direct line-force in part a.

Because of the gaussian nature of the profile function, x_b has only a very weak dependence on the optical depth, $x_b \sim \sqrt{\ln(qt)}$; it is near unity for moderately strong lines, i.e. for $qt \approx 10$, we find $x_b \approx 1$.

Apart from this weakly varying blue-edge factor, all optically thick lines thus contribute a nearly equal proportion g_{line}/v_{th} to the instability. Thus, when integrated over the full line-ensemble, the total growth rate is again found (Owocki and Rybicki 1984) to scale in proportion to the ratio of mean line-force to the thermal speed,

$$\Omega \approx \frac{g_{cak}}{v_{th}} \approx \frac{v_o(dv_o/dr)}{v_{th}} \approx \frac{v_o}{l_{sob}} \,. \tag{6.12}$$

Here the latter equalities follow from the steady equation of motion and imply that the instability growth is very large, about the flow rate through the Sobolev length. Since this is a large factor v_o/v_{th} bigger than the typical wind expansion rate $dv_o/dr \approx v_o/R_*$, a small perturbation at the wind base would, within this lineary theory, be amplified by an enourmous factor, of order $e^{v_o/v_{th}} \approx e^{100}$!

6.1.3 The Bridging Law

The above instability analysis ignores perturbations in the optical depth, and so only applies in the limit that the *perturbations* themselves are *optically thin*. By including self-consistently such optical depth perturbations, Owocki and Rybicki (1984) derived a more general, "bridging law" scaling for the perturbed radiative force

$$\frac{\delta g_{rad}}{\delta v} \approx \Omega \frac{ik\Lambda}{1+ik\Lambda} \,, \tag{6.13}$$

where the "bridging length" Λ is found to be of order the Sobolev length l_{sob}. For $k\Lambda \gg 1$, representing short-wavelength, optically thin perturbations, we recover the line-deshadowing instability

$$\frac{\delta g_{rad}}{\delta v} \approx \Omega \quad ; \quad k\Lambda \gg 1 \,, \tag{6.14}$$

while in the opposite limit $k\Lambda \ll 1$, representing long-wavelength perurbations, we recover the stable, Abbott-wave scalings of the Sobolev approximation

$$\frac{\delta g_{rad}}{\delta v} \approx ik\Omega\Lambda = ikc_A \quad ; \quad k\Lambda \ll 1 \,, \tag{6.15}$$

with $c_A = \Omega\Lambda$ the Abbott speed.

6.1.4 Line-Drag of the Diffuse Radiation

As first pointed out by Lucy (1984), this instability associated with line-absorption of the direct radiation from the stellar core can be counteracted by a "line-drag" associated with the diffuse component of scattered radiation. Most of the lines in hot-star winds have a nearly pure-scattering character, but the diffuse radiation has little dynamical effect on the mean wind driving because, as shown in figure

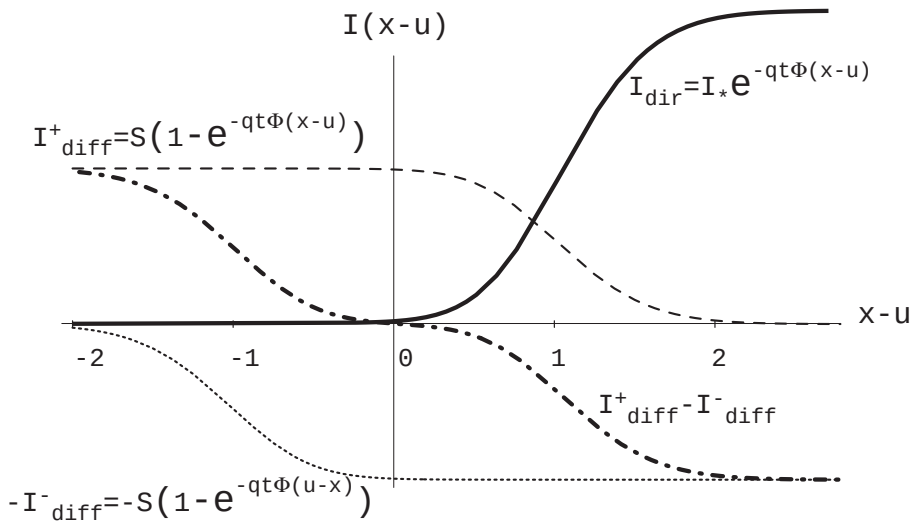

Fig. 17. Various compoents of the intensity vs. comoving-frame frequency $x-u$, for the Sobolev case of a smooth, supersonic flow.

5, photons scattered within a Sobolev line-resonance emerge with a near fore-aft symmetry in the local comoving frame of the wind. As further illustrated in figure 16b, this implies that the associated net diffuse force nearly vanishes. However, figure 16c shows that small velocity perturbations Doppler-shift the local line profile out of this mean comoving frame, leading to a stronger overlap with the backward vs. forward diffuse intensity, and so to a net drag force that is proportional to the *negative* of the perturbed velocity.

An essential element in figure 16 is that backward ($-$) streaming radiation appears peaked on the opposite (i.e. red) side of the comoving-frame line-center than either the direct or forward ($+$) streaming components. To see how this comes about, let us apply this "two-stream" approximation (in which $\mu = \pm 1$) for the diffuse force within the basic line-force integration (4.9),

$$g_{\rm diff} \approx \frac{2\pi q \kappa_e}{c} \int_{-\infty}^{\infty} dx \, [\phi(x-u) I_{\rm diff}(x,1,r) - \phi(x+u) I_{\rm diff}(x,-1,r)] \quad (6.16)$$

$$= \frac{2\pi q \kappa_e}{c} \int_{-\infty}^{\infty} dx \, \phi(x-u) \, [I_{\rm diff}(x,+1,r) - I_{\rm diff}(-x,-1,r)] \; , \quad (6.17)$$

where the latter equality uses the symmetry of the line profile function, $\phi(x) = \phi(-x)$, and a sign flip for the dummy integration variable $x \rightarrow -x$ to give the backward-streaming term a profile function evaluated with same comoving frame variable $x-u$ as the forward term. From the formal solution of the equation of

transfer (Mihalas 1978), this diffuse intensity takes the form,

$$I_{\rm diff}(\pm x,\pm 1,r) = \int S(r')\; e^{-q|t(\pm x,\pm 1,r)-t(\pm x,\pm 1,r')|}\; dt(\pm x,\pm 1,r') \quad (6.18)$$

$$\approx S(r)\left(1-e^{-qt(\pm x,\pm 1,r)}\right), \quad (6.19)$$

where the latter approximation assumes the source function within the integrand can be taken as nearly constant at the value for the local radius, $S(r') \approx S(r)$, which then allows the formal solution spatial integral to be carried out analytically. This "Smooth Source Function" (SSF) approximation is based on the idea that, for a pure scattering line, the source function is given by the frequency- and angle-integrated intensity, $S =< \bar{I} >$, and so tends to be less sensitive to local variations in, e.g. the velocity, than the optical depth terms $t(x,\mu,r')$. The source function can generally be well approximated by its optically thin form

$$S(r) = I_* \frac{1-\mu_*(r)}{2}, \quad (6.20)$$

where $\mu_*(r) = \sqrt{1-R_*^2/r^2}$. (In this two-stream approach, this also applies within the Sobolev approximation for all optical depths qt.)

For the forward (+) stream, the optical depth is the same as for the direct component, given by eqn. (4.11). For the backward (−) stream, it is

$$qt(-x,-1,r) \equiv \int_r^\infty \kappa\rho(r')\phi(-x+u(r'))dr' = \int_r^\infty \kappa\rho(r')\phi(-[x-u(r')])dr'\,. \quad (6.21)$$

For the smooth, background wind with velocity u_o, we can again use the same Sobolev approximation to localize the optical depth integrals

$$qt(\pm x,\pm 1,r) \approx \tau_s \Phi(\pm[x-u(r)])\,, \quad (6.22)$$

Application of eqns. (6.22) and (6.19) into the general force eqn. (6.17) then gives for the diffuse line-force (cf. eqn. 4.14)

$$g_{\rm diff}(r) = \frac{g_{thin}}{2(1+\mu_*)} \int_{-\infty}^{\infty} dx\, \phi\left(x-u(r)\right) \left[e^{-qt\Phi(u_o(r)-x)} - e^{-qt\Phi(x-u_o(r))}\right]. \quad (6.23)$$

For $u = u_o$, and again using the profile function symmetry, we find that the frequency integration of the two terms cancels (see figure 16), giving $g_{diff,o} = 0$. As noted above, the diffuse force vanishes in the Sobolev approximation.

However, for $u = u_o + \delta u$, expansion to first order in δu gives the "line-drag" effect for the perturbed diffuse force (cf. eqn. 6.11)

$$\frac{\delta g_{\rm diff}}{\delta v} \approx -\frac{g_{thin}}{v_{th}} \frac{1}{2(1+\mu_*)} \int_{-\infty}^{\infty} dx' \frac{d\phi(x')}{dx'} \left[e^{-qt\Phi(-x')} - e^{-qt\Phi(x')}\right] \quad (6.24)$$

$$\approx -2x_b \frac{g_{line}}{v_{th}} \frac{1}{1+\mu_*} \quad ; \quad qt \gg 1 \quad (6.25)$$

$$= -\frac{\Omega_{dir}}{1+\mu_*} \quad ; \quad qt \gg 1\,, \quad (6.26)$$

where Ω_{dir} is the instability growth rate associated with the direct component, as given in eqn. (6.11). The net instabililty growth rate is thus

$$\Omega_{net}(r) = \Omega_{dir} \frac{\mu_*(r)}{1+\mu_*(r)} \,. \tag{6.27}$$

Note thus that the instability is effectively *cancelled* near the surface $r \approx R_*$, where $\mu_* = 0$. But further out in the wind, where $\mu_* > 0$, there is still a strong net instability, approaching a growth rate of $\Omega_{net} \approx \Omega_{dir}/2$ far from the star, where $\mu_* \to 1$. Since this is still of order a factor 50 greater than the wind expansion rate, the cumulative amplification of a small perturbation over the wind should still be very large, i.e of order e^{50}.

The next section discusses numerical simulations of the nonlinear evolution of this line-deshadowing instability.

6.2 Numerical Simulation of Nonlinear Evolution of Instability-Generated Wind Structure

With such large growth rates, any finite perturbation should quickly become nonlinear, leading to extensive small-scale structure and variability. Ignoring for now any tendency for this structure to break up into a complex multidimensional form (see §6.2.4), let us first model the radial variability through *numerical* solution of the 1D, time-dependent equations for conservation of mass (cf. 2.7),

$$\frac{\partial \rho}{\partial t} + \frac{1}{r^2}\frac{d\rho v r^2}{dr} = 0 \,, \tag{6.28}$$

and momentum (cf. 2.6),

$$\frac{\partial v}{\partial t} + v\frac{dv}{dr} = -\frac{a^2}{\rho}\frac{dP}{dr} - \frac{GM_*}{r^2} + g_{rad} \,. \tag{6.29}$$

As in the steady-state models, we are again assuming that in these relatively dense winds, the balance between radiative heating and cooling will remain sufficiently dominant to keep the flow nearly isothermal near the stellar effective temperature, with thus a constant sound speed a. Models that include a full, time-dependent energy equation are discussed in §6.2.3.

6.2.1 Nonlocal Line-Force

A key challenge in solving these time-dependent equations regards the computation of the radiative acceleration g_{rad}. Since the instability only occurs for perturbations with a length scale near or below the Sobolev length, we cannot use the standard CAK/Sobolev form (4.19) for computing this force in terms of the *local* density and velocity gradient. Instead we must return to *nonlocal* forms that depend on the full optical depth *integral* (4.11). Combining eqns. (4.11) and (4.9),

and integrating over the CAK line ensemble (4.17), the integral, nonlocal, CAK generalization of the *direct* force is

$$g_{dir}(r) = g_e \bar{Q}^{1-\alpha} \int_{-\infty}^{\infty} dx \frac{\phi(x-u(r))}{t(x,1,r)^\alpha} \,. \tag{6.30}$$

In the Sobolev approximation, $t(x,1,r) \approx \Phi(x-u)t$, this recovers the CAK form (4.19); but for perturbations on a spatial scale near and below the Sobolev length its variation also scales in proportion to the perturbed velocity, leading to unstable amplification.

To account for the line-drag that reduces this instabiity, we need also to include a nonlocal form for the *ensemble diffuse* line-force,

$$g_{diff} = g_e \bar{Q}^{1-\alpha} \frac{1}{2(1+\mu_*)} \int_{-\infty}^{\infty} dx\, \phi(x-u(r)) \left(\frac{1}{t(-x,-1,r)^\alpha} - \frac{1}{t(x,1,r)^\alpha} \right) , \tag{6.31}$$

where we have again assumed the optically thin form (6.20) for the "Smooth Source Function", applied now to all lines of the ensemble.

In contrast to the strictly local dependence of the CAK force, evaluation of these direct and diffuse force components requires a much more costly numerical integration of the outward and inward optical depths for the full range of photon frequencies $0 < x < v_\infty/v_{th}$ that can interact with the line somewhere in the wind. These optical depths are then applied within an additional frequency integration weighted by the local line profile $\phi(x-u(r))$. For a frequency spacing $\Delta x \approx 0.3$ set to marginally resolve the line profile width, the total number of frequency points required is $n_x \approx v_\infty/(v_{th}\Delta x) \approx 1000$. Likewise, to obtain a similar minimal resolution of a few points per Sobolev length, the spatial grid must have at least $n_r \approx 1000$ points. Thus, in principle, the nested frequency-plus-radius integrations required for the line-force can require of order $n_x n_r \approx 10^6$ evaluations of the integrand.[1] Finally, such evaluations must now be applied within each time step of a time-dependent model of the instability-generated structure.

A key advantage to the above two-stream formulation is that it restricts this expensive optical depth integration to a single ray, namely along the local radial direction r. A disadvantage is that the direct force thus correponds to a point-star treatment that does not account for the finite angle of the star. Fortunately, a quite good account of this finite angle (accurate to within a few percent in the force) can be obtained by using instead a single *nonradial* integration ray, chosen to intersect the star's central plane with an imact parameter $p = R_*/\sqrt{2}$. Such a ray is more typically representative of the direction of emergent radiation than the central ray with $p = 0$, which represents the usual point-star approach. The integration then proceeds as before (cf. eqns. 4.11 and 6.21), except that it is now along a nonradial local direction $dz' = dr'/\mu'$, where $\mu' = \sqrt{1 - R_*^2/2r'^2}$, with the projection of thermal-unit velocity $u(r')$ at local radius r' now given by $\pm\mu' u(r')$.

[1] In practice, the integrand is nearly zero for frequencies more than few Doppler widths from

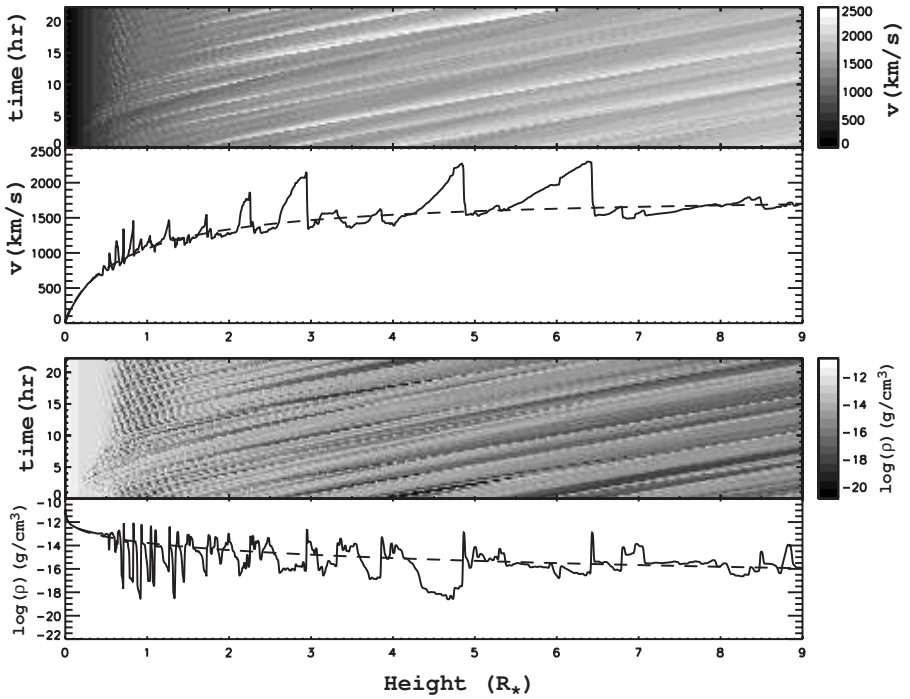

Fig. 18. Results of 1D Smooth-Source-Function simulation of the line-deshadowing instability. The line plots show the spatial variation of velocity (upper) and density (lower) at a fixed, arbitrary time snapshot. The corresponding grey scales show both the time (vertical axis) and height (horizontal axis) evolution. The dashed curve shows the corresponding smooth, steady CAK model.

6.2.2 Simulation Results for 1D Smooth-Source-Function Models

This Smooth-Source-Function (SSF) approach for the direct and diffuse components of the radiative acceleration can be applied within a numerical hydrodynamics code to simulate the nonlinear evolution of the line-deshadowing instability. Under the simplifying assumption of 1D isothermal flow, this is based on time-dependent equations (6.28) and (6.29) for conservation of mass and momentum.

Figure 18 illustrates the results of such a SSF simulation, starting from an initial condition set by smooth, steady-state CAK/Sobolev model (dashed curves). The line plots show the resulting radial variation of velocity (upper) and density (lower) at an arbitrary time snapshot long after this CAK initial condition. The grey scales show the correponding time evolution of deviations from this CAK

---

the local comoving-frame line center $x = u$, and with clever coding this can be exploited to reduce substantially, i.e. by factor 10 or more, the required number of integrand evaluations.

state. Because of the line-drag stabilization of the driving near the star (eqn. 6.27), the wind base remains smooth and steady. But away from the surface, the net strong instability leads to extensive structure in both velocity and density, roughly straddling the CAK steady-state.

This wind structure is "self-excited", arising spontaneously without any explict perturbation at the wind base, and even though the initial condition is set to the smooth, CAK model. Because the CAK and SSF line-forces have modest differences, especially near the subsonic wind base, the time-dependent model adjusts from this CAK initial condition, thus inducing an initial level of structure in the outer wind. But then, because of the backstreaming component of the optical depth within diffuse line-force, this outer wind structure induces small-amplitude fluctuations in the line-driving closer to the wind base. As the line-drag weakens with increased radius from the base, the increased net instability exponentially amplifies these small fluctuations, leading to further outer-wind structure, which then induces more base fluctuations, and so perpetuates the self-excitation.

In the outer wind, the velocity variations become highly nonlinear and non-monotonic, with amplitudes approaching 1000 km/s, leading to formation of strong shocks. However, comparison with the density show that these high-velocity regions have very low density, and thus represent only very little material. This anti-correlation between velocity and density turns out to be a quite general feature of the structure generated by the line-deshadowing instability. It arises in part because the unstable linear waves that lead to the structure have an *inward* propagation relative to the mean flow. Applying linear, sinusoidal ($\sim e^{i(kr-\omega t)}$) perturbations in density $\delta\rho$ and velocity δv within the time-dependent mass conservation eqn. (6.28), we find to first order

$$-i\omega\delta\rho/\rho_o + ik\delta v = 0, \tag{6.32}$$

which solves to $\delta\rho/\rho_o = \delta v/(\omega/k)$. Thus for inward-propagating waves with $\Re(\omega/k) < 0$, as implied for the bridging law (6.13) between Abbott waves and instability, there is an opposite phase between velocity and density. As these waves are amplified by the instability, this grows into the extensive structure with anti-correlation between velocity and density.

For most of the wind mass, the dominant overall effect of the instability is to concentrate material into dense clumps. This has important implications for interpreting emission diagnostics that scale with the square of the density, such as radio or Balmer emission, which depend on recombination or collisional excitation of the emitting ion with an electron. When these are used to infer mass loss rates, the associated overestimate scales as the "clumping factor",

$$\frac{\dot{M}_{obs}}{\dot{M}_{true}} = f_{cl} \equiv \frac{\sqrt{\langle\rho^2\rangle}}{\langle\rho\rangle}\,, \tag{6.33}$$

where the angle brackets now denote averaging over the structure. In these 1D SSF simulations, the computed factor can be 10 or more, which would imply a substantial overestimate of mass loss rates. (As shown in §6.2.4, 2D simulations of the instability yield a somewhat smaller, more realistic clumping factor.)

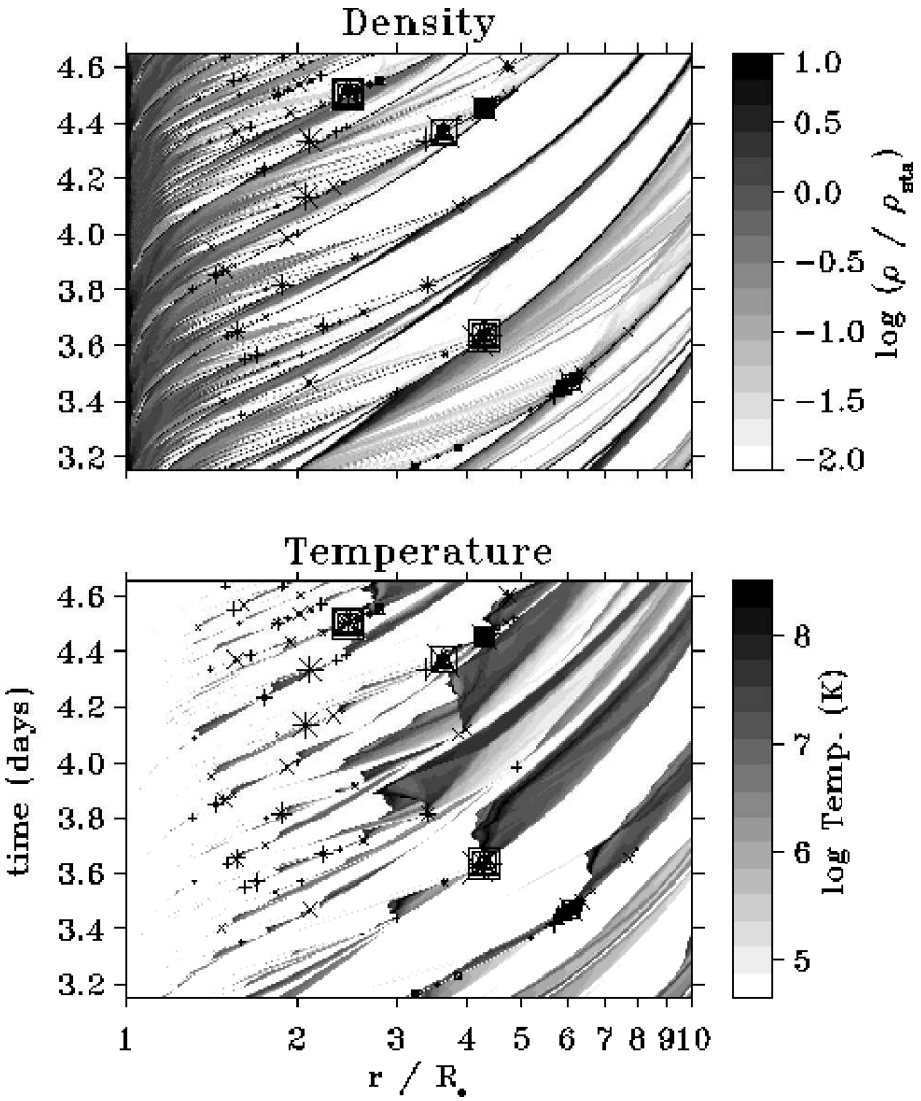

Fig. 19. Greyscale rendition of the evolution of wind density and temperature, for time-dependent wind-instability models with structure formation triggered by photospheric perturbations. The boxed crosses identify localized region of clump-clump collision that lead to the hot, dense gas needed for a substantial level of soft X-rays emission.

6.2.3 Energy Balance Models with X-ray Emission

Observations by orbiting X-ray satellites show O-stars to be moderately strong sources of soft X-rays, following roughly a scaling law $L_x \approx 10^{-7} L_{bol}$ between the

X-ray and bolometric luminosity. A potentially natural explanation is that this X-ray emission might arise from gas heated in shocks induced by the strong line-deshadowing instability. To model X-ray emission, Feldmeier *et al.* (1995, 1997) have carried out SSF simulations including a 1D time-dependent energy equation (cf. eqn. 2.8) that ignores thermal conduction, but does include the important radiative cooling term (cf. eqn. 3.2),

$$\frac{\partial e}{\partial t} + \frac{1}{r^2}\frac{\partial \left(r^2 e v\right)}{\partial r} = -\frac{P}{r^2}\frac{\partial \left(r^2 v\right)}{\partial r} - n_e n_H \Lambda(T)\,, \tag{6.34}$$

where for the assumed monotonic gas with $\gamma = 5/3$, the energy and pressure are related by $e = P/(\gamma - 1) = 3P/2$.

As discussed by Feldmeier (1995), there are severe difficulties with numerically resolving the sometimes narrow cooling region behind strong shocks, with diffusion and overstable oscillation effects that suppress the amount of hot, X-ray emitting gas. But even when these effects are minimized (essentially by reducing the steepness of the cooling function $\Lambda(T)$ at low temperatures), the level of X-ray emission in SSF models with only self-excited instability structiure is well below what is needed to explain the observed X-ray luminosities. As noted above, this is because in such models the highest speed flow has very low density, and thus feeds very little material through the strong shocks needed to heat gas to X-ray emitting temperatures.

To increase the level of X-ray emission, Feldmeier *et al.* (1997) introduced intrinsic perturbations at the wind base, assuming the underlying stellar photosphere has a turbulent spectrum of compressible sound waves characterized by abrupt phase shifts in velocity and density. These abrupt shifts seed wind variations that, when amplified by the line-deshadowing instabilty, now include substantial velocity variations among the dense clumps. As illustrated in figure 19, when these dense clumps collide, they induce regions of relatively dense, hot gas which produce localized bursts of X-ray emission. Averaged over time, these localized regions can collectively yield X-ray emission with a brightness and spectrum that is comparable to what is typically observed from such hot stars.

6.2.4 "2DH+1DR" Models with 2D-Hydrodynamics and 1D-Radiation Transport

Because of the computational expense of carrying out nonlocal optical depth integrations at each time step, such instability simulations have generally been limited to just 1D. More realistically, various kinds of thin-shell instabilites (see, e.g., Vishniac 1994) can be expected to break up the structure into a complex, multidimensional form. As a first step to modelling both radial and lateral structure, recent efforts by Dessart and Owocki (2003) apply a restricted "2D-H+1D-R" approach, extending the hydrodynamical model to 2D (adding azimuthal angle ϕ to radius r), but still keeping the 1D-SSF radial integration for the inward/outward optical depth within each azimuthal zone. To allow high lateral resolution $d\phi = 0.2^o$ with a moderate number n_ϕ of azimuthal zones, the lateral mesh is restricted to a narrow "wedge" with azimuthal range $\Delta\phi = n_\phi \times d\phi = 12^{\rm o}$, over which periodic

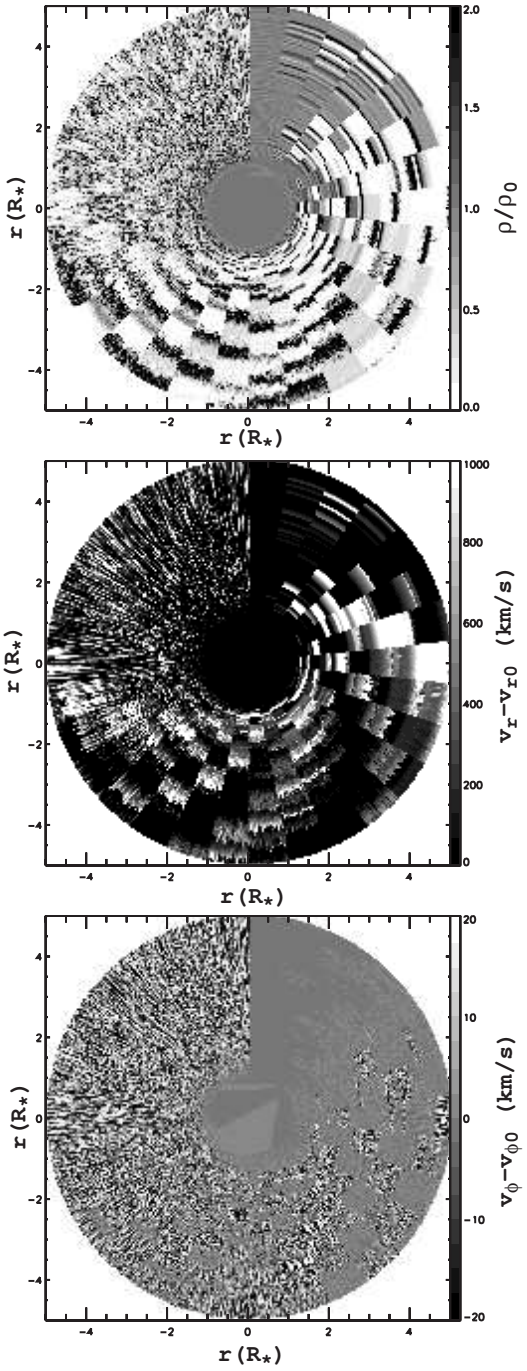

Fig. 20. Grayscale representation for the deviations of a. density, b. radial velocity, and c. azimuthal velocity, rendered as a time sequence of 2D wedges of the simulation model azimuthal range $\Delta\phi = 12^o$ stacked clockwise from the vertical in intervals of 4000 sec.

boundary conditions are implemented by setting all hydrodynamic variables (i.e., density ρ, radial velocity v_r, and azimuthal velocity v_ϕ) to equal values between the left and right interfaces [e.g. for density, $\rho(r_i, \phi_0) = \rho(r_i, \phi_{n_\phi})$].

Figure 20 illustrates results for the time evolution of the resulting 2D flow structure, showing polar coordinate greyscale plots for the relative deviations from the initial CAK steady solutions for (a) density, (b) radial velocity, and (c) azimuthal velocity. These panels employ a rather novel "clock format", in which the state snapshot in each azimuthal wedge of $\Delta\phi = 12^o$ is repeated as a time sequence, starting from the 12 o'clock position and proceeding clockwise at fixed time intervals of 4000 sec.

Starting from the initial smooth CAK state, the line-deshadowing instability is first manifest as strong radial velocity variations and associated density compressions that initially extend nearly coherently across the full azimuthal range of the computational wedge. But as these initial "shell" structures are accelerated outward, they become progressively disrupted by Rayleigh-Taylor or thin-shell (Vishniac 1994) instabilities that operate in azimuth down to the grid scale $d\phi = 0.2^o$. Within the SSF formalism applied through separate radial integrations in each azimuthal zone, the lateral phase variations that arise in the outer wind of this initial structure lead – through the backscattering component of the diffuse radiative force – to corresponding lateral phase variations in small-amplitude fluctuations induced near the wind base. As these now laterally varying fluctuations are amplified within the separate radial propagation in each azimuthal zone, the outer wind structure becomes evermore broken up. By the time $t = 4000 \times 360/12 = 120,000$ sec of the final state shown here (just before 12 o'clock in figs. 1a-c.), the wind is thus characterized by a nearly complete lateral incoherence down to angular scales approaching that of the azimuthal grid.

Such an approach may well exaggerate the level of variation on small lateral scales. The avoidance of the *lateral* integration needed to compute an azimuthal component of the diffuse line-force means that the model ignores a potentially strong net lateral line-drag that should strongly damp azimuthal velocity perturbations on scales below the lateral Sobolev length $l_0 \equiv r v_{th}/v_r$ (Rybicki *et al.* 1990). Presuming that this would inhibit development of lateral instability at such scales, then any lateral breakup would be limited to a minimum lateral angular scale of $\Delta\phi_{min} \approx l_0/r = v_{th}/v_r \approx 0.01\,\mathrm{rad} \approx 0.5^o$. Future work should address this issue through explicit incorporation of the lateral line-force and the associated line-drag effect.

Figure 2 shows line plots of the radial variation of various azimuthally and temporally averaged measures of the flow properties. Since the model ignores any lateral component of the line-force, the variations in azimuthal velocity arise completely from lateral variations in gas pressure, and so have a typical RMS amplitude $\Delta v_{\phi,rms} \approx 10 - 15$ km/s comparable to the sound speed $a = 24$ km/s. The structure in density and radial velocity are a direct outcome of the LDI. The lateral "filling in" of radial rarefactions leads here to a significantly lower density "clumping factor" $f_{cl} \equiv < \rho^2 > / < \rho >^2 \approx 3 - 5$ (with angle brackets representing temporal and/or azimuthal averaging) than is typically found in analagous 1D LDI

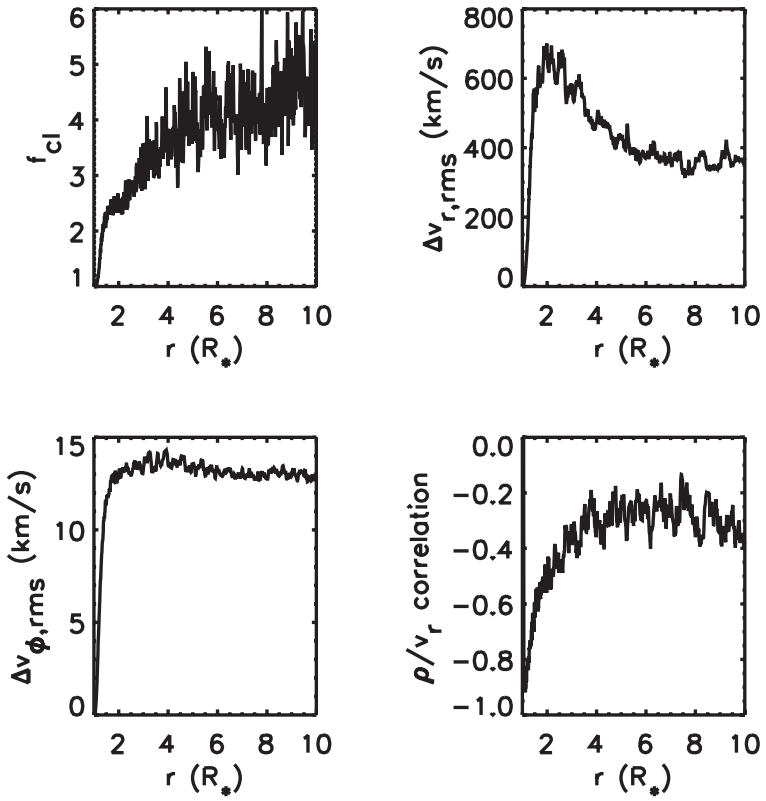

Fig. 21. Radial variation of temporal and azimuthal averages that characterize the nature of flow structure. a. clumping factor f_{cl}; b. radial and c. azimuthal velocity dispersion; and d. velocity-density correlation coefficient.

simulations, which have $f_{cl} \approx 10$ (Runacres & Owocki 2002). On the other hand, the possibility for lateral velocity shear now allows high-speed rarefactions to flow past slower, localized density enhancements, instead of being abruptly truncated as they are in purely radial models. As a result, the radial velocity dispersion in these 2D simulations, $\Delta v_{r,rms} \approx 400 - 700$ km/s, is actually somewhat *higher* that in corresponding 1D models, $\Delta v_{r,rms} \approx 200 - 300$ km/s.

Overall the picture presented by these 2D simulations differs markedly from the 1D models of radially compressed shell structures. The general finding of disruption by lateral instabilities seems likely to be a quite robust result. But establishing the exact limiting angular scale will require further studies that include the lateral transfer of diffuse radiation. This could limit the smallest lateral scale in two ways. The first is through lateral averaging of variation in the diffuse, backscattered radiation that leads to structure self-excitation at the wind base.

The second is through the lateral line-drag effect that could suppress unstable growth at the smallest lateral scales in the outer wind. Developing methods for tractable computation of the lateral component of the diffuse line-force should thus be a principal focus of future studies of the multidimensional nature of wind structure generated by the line-driven instability.

6.3 Summary for Abbott Waves and Line-Deshadowing Instability

- In linear perturbation analysis of a CAK line-driven wind, the scaling of the line-force with velocity gradient leads to a a new wave mode, the "Abbott wave", which is marginally stable, with an *inward* propogation at a speed comparable to the wind outflow speed.

- Below the CAK critical point, the flow speed is somewhat slower than the Abbott speed, or "sub-Abbottic". Above it, it is faster than the Abbott speed, or "super-Abbottic". The critical point thus represents the outermost radius from which Abbott waves can propogate back to the wind base.

- For perturbations on a scale below the Sobolev length, the deshadowing from the perturbed Doppler shift makes the perturbed force increase in proportion to the perturbed velocity, not its gradient; this gives rise to a strong Line-Deshodowning-Instability, with growth rates roughly equal to the flow rate through a Sobolev length, implying of order 100 e-folds of amplification over the full wind acceleration.

- The diffuse, scattered component of the radiation yields a "line-drag" effect that reduces the net instability, nearly cancelling it near the wind base, but only reducing it by a factor of two or so in the outer wind.

- Using a "Smooth Source Function" (SSF) approach for computing nonlocal integral forms for the direct and diffuse components of the line-force, numerical simulations of the nonlinear evolution of the strong net instability show the self-excited development of wind structure within about a half-stellar radius from the wind base.

- This self-excited structure is characterized by high-speed rarefactions terminating in strong shocks that compress the bulk of slower moving material into dense clumps.

- The extensive clumping means that emission diagnostics that scale with the square of the density may overestimate the wind mass loss rate.

- Since only very little material actually passes through the strong shocks of such self-excited structure, explaining the observed level of soft X-ray emission requires using base turblence to seed wind structure with greater velocity dispersion causing stronger collisions among the dense clumps.

- 2D simulation employing a simplfied radial form for the nonlocal line force show that the structure arising from the LDI tends to break up into clumps with lateral sizes ranging down to the grid scale.
- To determine whether lateral line-drag and related effects might limit the lateral scale of wind structure, future multi-D simulations must develop efficient methods for computing the lateral component of the diffuse line-force.

7 Effect of Rotation on Line-Driven Stellar Winds

The hot, luminous stars that give rise to line-driven stellar winds tend generally to have quite rapid stellar rotation. This is most directly evident throught the extensive broadening of their photospheric absorption lines, which suggest projected equatorial rotation speeds $V \sin i$ of hundreds of km/s. (Here $\sin i \leq 1$ accounts for the inclination angle i of the observer line-of-sigh to the stellar rotation axis.) In some of the most rapid rotators, e.g. the Be stars, the rotation is inferred to be a substantial fraction, perhaps 70-80% or more, of the so-called critical rotation speed, $v_{crit} \equiv \sqrt{2GM_*/R_{eq}}$, for which material at the rotational equator of radius R_{eq} would be in Keplerian orbit. This section examines how such rapid rotation should affect the stellar wind mass loss.

7.1 1D Scaling Laws for Centrigually Enhanced, Line-Driven Mass Loss

Initial investigations (Friend & Abbott 1986; Pauldrach *et al.* 1986) of the possible role of rotation on radiatively driven winds derived 1-D models based on the standard CAK line-driving formalism, but now adding the effect of an outward centrifugal acceleration in the equatorial plane, $g_{cent}(r) = V_{rot}^2 R_*^2/r^3$, where V_{rot} is the equatorial rotation speed at the stellar surface radius $r = R_*$. Although this centrifugal term declines faster with radius than gravity, the mass loss is fixed at a critical point quite near the stellar surface. This suggests that the effect on the local mass flux at any colatitude θ of a rotating star can be written in terms of a centrifugally reduced, *effective* surface gravity

$$g_{eff}(\theta) = \frac{GM}{R_*^2}\left(1 - \Omega \sin^2\theta\right), \tag{7.1}$$

where G and M_* are the gravitation constant and stellar mass, and $\Omega \equiv V_{rot}^2 R_*/GM$. We thus rewrite the standard CAK mass loss rate scaling law (cf. eqn. 4.31) in terms of *surface* values of the mass flux $\dot{m} = \rho v$, radiative flux F, and effective gravity g_{eff}, relative to corresponding polar ($\theta = 0$) values $\dot{m}_o$, F_o, and $g_o = GM/R_*^2$,

$$\frac{\dot{m}(\theta)}{\dot{m}_o} = \left[\frac{F(\theta)}{F_o}\right]^{1/\alpha} \left[\frac{g_{eff}(\theta)}{g_o}\right]^{1-1/\alpha}, \tag{7.2}$$

where α is the usual CAK exponent, assumed here to be constant at all latitudes (cf. §7.3 below).

For example, if we take $F(\theta) = F_o$, then we obtain the scaling

$$\frac{\dot{m}(\theta)}{\dot{m}_o} = \left[1 - \Omega \sin^2\theta\right]^{1-1/\alpha} \quad ; \quad F(\theta) = F_o\,. \tag{7.3}$$

Since $\alpha < 1$, the exponent $1-1/\alpha$ is negative, implying that the mass flux increases monotonically from pole ($\sin\theta \to 0$) toward the equator ($\sin\theta \to 1$). This view, characterisic of the first analyses of the effects of rotation on line-driven mass loss,

is thus that the reduced effective gravity toward the rotational equator should allow for a stronger mass loss, and thus an enhanced density.

Subsequent work has, however, led to a quite different picture. This is because, contrary what is assumed above, the radiative flux from a rapidly rotating star need not be constant in latitude. Rather, as first demonstrated by von Zeipel (1924), for a radiative stellar envelope undergoing solid body rotation, the emergent radiative flux at any latitude varies in proportion to the centrifugally reduced effective gravity, $F(\theta) \sim g_{eff}$. Applying this equatorial "gravity darkening" for the flux, we obtain

$$\frac{\dot{m}(\theta)}{\dot{m}_o} = 1 - \Omega \sin^2 \theta \quad ; \quad F(\theta) \sim g_{eff}(\theta) \tag{7.4}$$

so that the mass flux now *decreases* towards the equator, with a maximum at the *pole* (see §7.1)!

Friend and Abbott (1986) likewise find that the terminal wind speed is decreased by rotation in the equator. We can also approximate this result within our 1-D concept of a centrifugally reduced gravity to predict a latitudinally varying wind terminal speed that scales with an effective escape speed, $v_\infty(\theta) \sim v_{esc}\sqrt{1 - \Omega \sin^2 \theta}$. The latitudinal variation of density is then obtained from $\rho \sim \dot{m}/v_\infty$.

7.2 2-D Dynamical Simulations of Rotating Winds

7.2.1 Equatorial Wind Compressed Disks

A major advance in modelling rotating hot-star winds was development of the elegantly simple "Wind Compressed Disk" (WCD) paradigm by Bjorkman & Cassinelli (1993). They noted that, like satellites launched into earth orbit, parcels of gas gradually driven radially outward from a rapidly rotating star should remain in a tilted 'orbital plane' that brings them over the equator. As wind parcels from opposite hemispheres collide over the equator, they form a disk of compressed gas. A key simplification here is to assume that, like gravity, the radiative driving is a radially directed, *central* force. As such, the total angular momentum of each individual wind fluid parcel is conserved, fixed by the rotation at its initial latitude at the wind base (i.e., at the subsonic stellar surface), and remaining in a fixed plane perpendicular to the angular momentum vector. The crucial criterion for the formation of a disk is that the near-star wind speed not be too much larger than the rotation speed.

To test this WCD paradigm, Owocki, Cranmer, and Blondin (1994) carried out 2-D hydrodynamical simulations of line-driven winds from rotating hot-stars. In keeping with the original WCD model, they assumed a purely radial driving force, though now computed dynamically using the finite-disk, spherical-star form of the usual CAK line-driving formalism (Friend & Abbott 1986; Pauldrach *et al.* 1986). The results, shown in figure 1a for typical model of B2 star with $V_{rot} = 350$ km/s, generally confirm the basic tenets of the WCD model, with certain detailed modifications (e.g., infall of inner disk material). The overall wind morphology consists

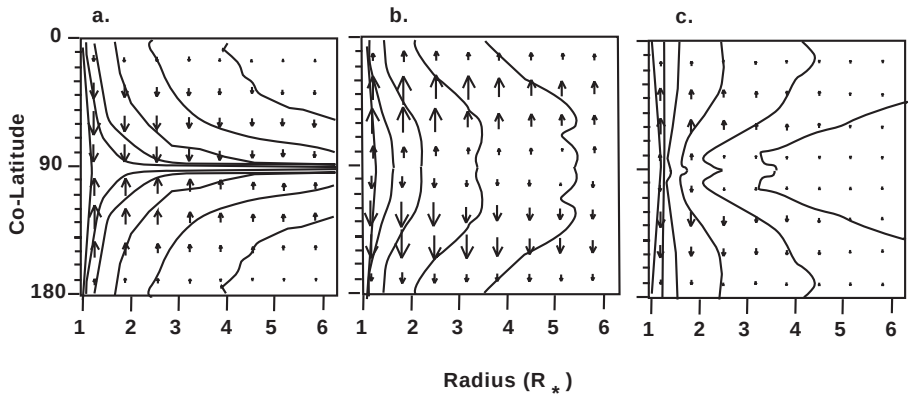

Fig. 22. Contours of stellar wind density plotted vs. colatitude θ and radius r, spaced logarithmically with two contours per decade, with label denoting the contour for $\rho = 10^{-16}$g/cm^3. The superposed vectors represent the latitudinal velocity, with the maximum length corresponding to a magnitude of v_θ =100 km/s. The three panels show the cases (a) without nonradial forces or gravity darkening, (b) with nonradial forces but no gravity darkening, and (c) with both nonradial forces and gravity darkening.

of a relatively fast, low-density polar wind, plus a dense equatorial disk with slow outflow in its outer part. Figure 1a shows density contours for this standard WCD case, plotted vs. radius and colatitude, with superposed vectors representing the magnitude and sense of the latitudinal velocity component $v_\theta(r,\theta)$. The WCD, manifest here by the strong equatorial extension of higher density contours, is the direct result of the flow compression associated with the equatorward sense of the latitudinal velocity from both the northern and southern hemispheres.

7.2.2 Inhibition of WCD by Poleward Line-Force Component

For rotating stars, the line acceleration can generally also have *nonradial* components. Within the CAK formalism of a fixed ensemble of lines with a power-law number distribution in opacity, its vector form is given by integration over solid angle Ω_* of the stellar core intensity I (cf. eqn. 4.24),

$$\mathbf{g}^{\rm rad}(\mathbf{r}) = \frac{K}{W^\delta \rho(\mathbf{r})^{\alpha-\delta} c} \int_{\Omega_*} d\Omega\, \mathbf{n}\, I(\mathbf{n},\mathbf{r})\, \{\mathbf{n}\cdot\nabla\,[\mathbf{n}\cdot\mathbf{v}(\mathbf{r})]\}^\alpha\ , \qquad (7.5)$$

where K is proportional to the CAK line normalization (k or $\bar{Q}$), and the exponent δ accounts for the ionization-state dependence on density ρ and dilution factor W (cf. eqn. 4.38). Note that the weighting for the force contribution of each ray along a direction $\mathbf{n}$ is proportional to the projected velocity gradient in that direction, $\mathbf{n}\cdot\nabla\,[\mathbf{n}\cdot\mathbf{v}(\mathbf{r})]$.

Owocki, Cranmer, and Gayley (1996) carried out simulations of rotating winds including these nonradial line-force components. Figure 1b shows the correspond-

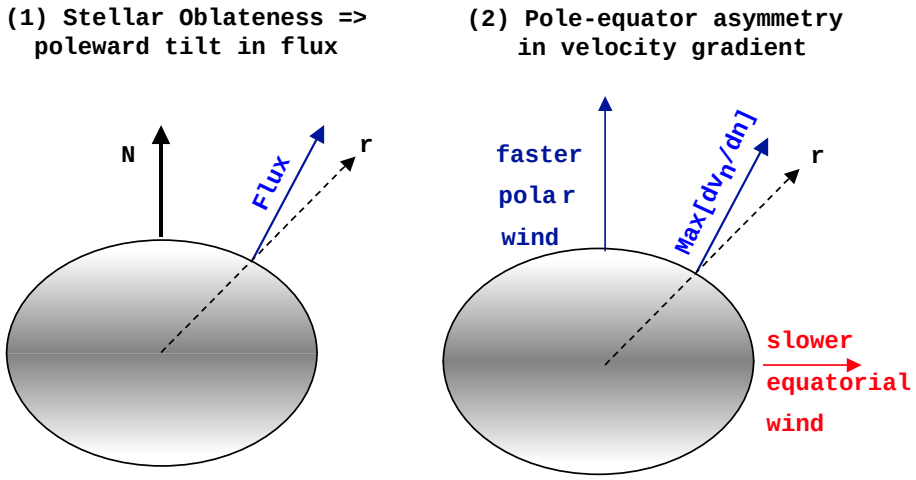

Fig. 23. Illustration of the origin of poleward component of the radiative force from a rotating star. Left: The poleward tilt of the radiative flux arising from the oblateness of the stellar surface contributes to a poleward component of the driving force. Right: Since the wind speed scales with surface escape speed, the lower effective gravity of the equator leads to a slower equatorial speed. The associated poleward increase in speed leads to a poleward tilt in the velocity gradient, and this again contributes to a poleward component of the line force.

ing wind density structure, still assuming a uniformly bright stellar core. As predicted in the above 1-D analysis, the reduced gravity, enhanced mass loss, and lower flow speed near the equator yield a broad, moderate density enhancement in the equatorial wind. But there is *no wind compressed disk*! Indeed, the sense of the superposed vectors is now reversed, indicating that the latitudinal velocity is now *away from the equator*. As such, there is no longer any wind compression effect, and so the tendency to form a WCD is completely inhibited.

This latitudinal flow reversal is a direct consequence of a *poleward* component of the line-force. As illustrated in figure 23, this poleward line-force stems from two effects. First, the centrifugally induced oblateness of the stellar surface means the surface flux has a non-zero poleward component, thus contributing to a poleward radiative driving force. The second effect is a bit more subtle, arising from asymmetries in the line-of-sight velocity gradient, which operatie through the velocity-gradient weighting of the angle integral in eqn. (7.5).

The lower effective gravity near the equator implies generally lower outflow speeds there, and thus from most midlatitude locations in the wind, the line-of-sight velocity gradient is stronger when looking toward the equator than toward the pole. Hence, photons from near the equator scatter at a higher rate and so impart a stronger impulse than those from near the pole, thus enhancing the net poleward component of the line-force. A simple expansion analysis shows that this

latitudinal force can be approximated by

$$g_\theta \approx \frac{R_*^2}{4r^2}\ \frac{v_r}{r}\frac{\partial v_r}{\partial \theta}. \tag{7.6}$$

The magnitude of this poleward force is small, generally not much more than 10% of the radial line-force; but the equatorward flow speeds are similarly small, i.e. less than 100 km/s in the WCD model, or only a few percent of the maximum radial speed. Thus, while the radial line-force must be strong enough to overcome the stellar gravity to drive an outflow to terminal speeds of more than 1000 km/s, the poleward latitudinal line-force is unopposed by any other body force, and need only overcome inertial terms characterized by a modest, < 100 km/s equatorward drift. From this perspective, it thus seems clear that the derived nonradial forces should indeed be dynamically quite significant in redirecting the equatorward drift needed for a WCD.

7.2.3 Spindown of Wind Rotation

Although these 2-D models have an assumed azimuthal symmetry, there is nonetheless also a nonzero *azimuthal* component of the line-force, which again results from asymmetries in the line-of-sight velocity gradient. Because wind rotation speed declines with increasing radius, the velocity gradient toward the receding stellar hemisphere is greater than that toward the approaching hemisphere. Through eqn. (7.5), this now implies a net line-force *against* the sense of rotation (Grinin 1978).

For this case of azimuthal symmetry in all variables, the ray-projected velocity gradient in eq. (7.5) simplifies to

$$\mathbf{n}\cdot\nabla\left[\mathbf{n}\cdot\mathbf{v}\right] = \mu^2\frac{\partial v_r}{\partial r} + \left(1-\mu^2\right)\frac{v_r}{r} + \mu\sqrt{1-\mu^2}\ r\sin\phi\frac{\partial(v_\phi/r)}{\partial r}. \tag{7.7}$$

Here $\mu \equiv \mathbf{n}\cdot\mathbf{r}/r$ is the radial direction cosine of the outward ray $\mathbf{n}$ from the star, while ϕ measures its orientation about this radial direction, with positive (negative) ϕ denoting prograde (retrograde) rays that track along (against) the wind rotation.

The first two terms in eq. (7.7), representing the effect of the wind acceleration, are both positive for the usual case of an outward radial velocity v_r that increases monotonically with radius r. However the last term, associated with the rotational shear, is *negative* whenever (as is typically the case) the radial variation of the azimuthal velocity v_ϕ does not keep up with a rigid rotation law, $v_\phi \sim r$. Overall, the total line-of-sight velocity gradient is thus reduced along prograde rays with $\sin\phi > 0$, but enhanced along retrograde rays with $\sin\phi < 0$. Integrated over the stellar disk, the resulting stronger impulse from the retrograde rays leads to a net azimuthal line-force acting *against* the rotation.

Figure 24 illustrates the flow for a simple rotating wind model with azimuthal velocity set according to angular momentum conservation. The left panel plots vectors for the velocity of the rotating wind in the fixed stellar frame. The two

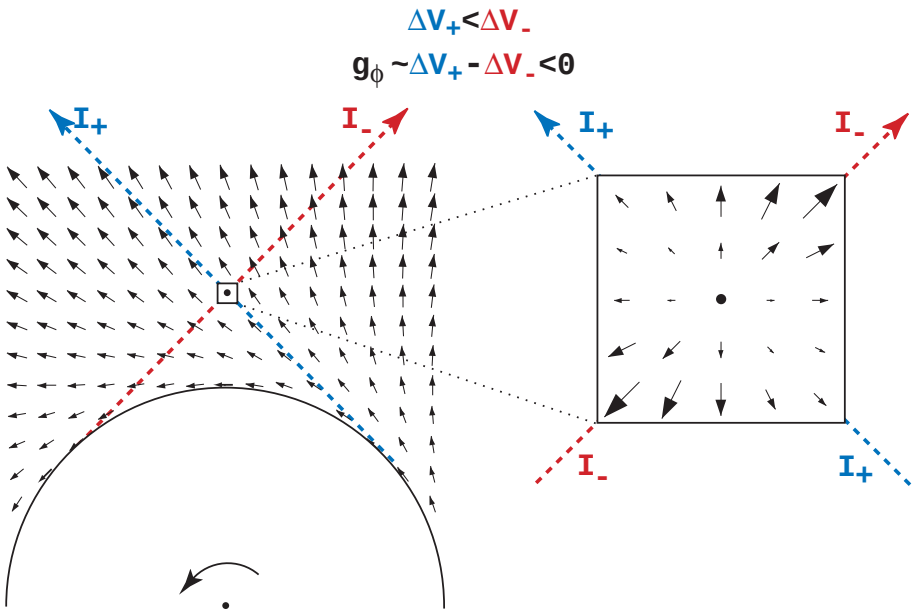

Fig. 24. Flow velocity vectors in the equatorial plane of a heuristic rotating wind model with radial velocity given by a 'beta=1' law, $v(r) = V_\infty(1-R_{eq}/r)$, and azimuthal velocity set by angular momentum conservation, $v_\phi(r) = V_{eq}R_{eq}/r$, here with $V_{eq} = V_\infty/3$. The zoom-in on the flow within the square box illustrates the local anisotropy of the wind expansion as viewed from a sample wind point (denoted by the bold dot), with the arrows now representing the component of *relative velocity along* a direction from the point. This shows how the intensity along a sample retrograde ray (I_-) traverses a stronger line-of-sight velocity change than a corresponding prograde ray (I_+), thus giving rise to a net retrograde line-force, $g_\phi < 0$.

dashed lines denote the stellar intensity along sample prograde (I_+) and retrograde (I_-) rays. Note that along the prograde ray, the vectors are more constantly aligned, whereas along the retrograde ray, they change rapidly from against to along the ray direction. The zoom-in box shows more explicitly the associated local anisotropy of the velocity gradient near a sample wind point. Here the arrows now represent the *relative* velocity component *along the direction* from the point. This makes quite clear that the intensity along a sample retrograde ray (I_-) traverses a stronger line-of-sight velocity change than a corresponding prograde ray (I_+), implying a net retrograde line-force, $g_\phi < 0$.

Its peak magnitude is roughly comparable to that for the poleward line-force, but this is sufficient to cause a modest wind spindown, characterized by about a 30% decrease in the specific angular momentum of the equatorial wind outflow beyond a few tenths of a stellar radius from the surface.

7.3 Effect of Gravity Darkening

7.3.1 Uniform Wind Driving Parameters

Fig. 1c shows results for the corresponding rotating wind model with both non-radial forces and a gravity-darkened surface flux $F(\theta) \sim g_{eff}(\theta)$ (von Zeipel 1924; see also Cranmer & Owocki 1999). In this case, not only is there no disk, but the overall density in the equatorial regions is actually *reduced* relative to that at higher latitudes. This picture is in marked contrast with previous analyses that envisioned an enhanced equatorial mass loss [e.g., eqn. (7.3); Friend and Abbott 1986], but it agrees well with the predictions of the gravity-darkened mass-flux scaling (7.4). Despite the reduced gravity near the equator, the wind mass flux there is now lower, owing to the reduced radiative flux associated with gravity darkening. The superposed vectors further show that the latitudinal velocity is again away from the equator, though with a somewhat lower magnitude than in Figure 1b, owing to the reduced poleward force associated with the reduced radiative flux from the equator.

7.3.2 Equatorial Bi-Stability Zone

The above calculations have assumed fixed values of the CAK parameters (α, k, and δ), but in general these can be expected to vary with variations in, e.g., effective temperature and density. A particularly important example of this is the Lamers and Pauldrach (1991) *Bi-Stability* model for equatorial enhanced winds in B[e] stars. At effective temperatures near 20,000 K, the increased recombination of hydrogen tends to make a wind become optically thick in the Lyman continuum, thus dramatically altering the wind ionization/excitation balance, and so leading to a marked shift of line-driving parameters. The effect can be most easily described in terms of a decreasing CAK exponent α, with a relatively constant line normalization parameter $\bar{Q} \approx 10^3$, related to the usual CAK k constant by $k = \bar{Q}^{1-\alpha}(v_{th}/c)^{\alpha}/(1-\alpha)$ (Gayley 1995). Within CAK theory, the mass flux varies as $\dot{m} \sim \bar{Q}^{-1+1/\alpha}$, and so adopting this into the scaling formulae in §7.1, we find for the latitudinal variation of density $\rho \sim \dot{m}/v$,

$$\frac{\rho(\theta)}{\rho_o} = \sqrt{1-\Omega\sin^2\theta}\left(\Gamma_e\bar{Q}\right)^{1/\alpha-1/\alpha_o}, \tag{7.8}$$

where $\Gamma_e = \kappa_e F/g_{eff}c$ is the surface Eddington factor, which is independent of latitude in the standard von Zeipel (1924) scaling $F \sim g_{eff}$ for gravity darkening. The exponent α is now assumed to vary in latitude, e.g. from a typical O-star value $\alpha_o \approx 2/3$ at the relatively high-temperature pole, to a lower, B-star value $\alpha \approx 1/2$ at lower latitudes, where the rotation brings the effective temperature near or below the critical bi-stability temperature of $\sim$ 20,000 K. For stars with Eddington factors Γ_e not much less than unity, the large intrinsic value of $\bar{Q}$ implies that this shift in α can cause a strong increase in mass flux, as signified by the second term in eqn. (7.8). For example, for the case $\Gamma_e = 0.5$, $\bar{Q} = 10^3$, $\alpha_o = 2/3$, and $\alpha = 1/2$, this bistability density jump represents a quite large

factor, $\sim \sqrt{500} \approx 22$. In principle, this could occur quite abruptly near and below the latitude of the critical temperature, and thus overwhelm the more gradual tendency for the mass flux to decline with the decreasing radiative flux near the equator. As such, this model remains a viable possibility for explaining moderate increases in equatorial density, such as inferred for B[e] stars.

7.4 Summary of Rotating Line-Driven Winds

- For rotating stars, the outward centrifugal acceleration near the stellar equator reduces the effective gravity. Since the outward wind acceleration tends to scale with the gravity, this leads to wind speeds that are slower in equatorial regions than near the pole.
- If a rotating star is taken to be uniformly bright, the lower effective gravity near the equator also leads to a higher equatorial mass flux; together with the lower wind speed, this implies a higher equatorial wind density.
- However, for a star with equatorial "gravity darkening" – in which the radiative flux scales in proportion to the effective gravity – the mass flux is strongest over the relative bright stellar poles.
- In stars with surface temperatures staddling 20,000 K, a "bi-stability" shift in ionization can increase the line-opacity near the relatively cool equator, and thus lead again to stronger equatorial mass flux and wind density.
- In 2D models in which the wind driving is assumed to be purely radial, conservation of angular momentum of tends to focus material from higher latitudes toward an equatorial "Wind Compressed Disk" (WCD).
- However, for line-driven winds, a net poleward component of the force is sufficient to reverse this equatorward flow, and thus inhibit formation of a WCD.
- This poleward line-force results from both the poleward tilt of radiative flux from the rotationally oblate surface, and from a poleward tilt in the velocity gradient associated with the equator-to-pole increase in the wind speed.
- Near the equatorial plane of a rotating wind, the stronger velocity gradient toward the receding vs. approaching limb gives line-driving a net azimuthal component that can act to "spin down" the wind rotation, typically by about 30%.

8 The Eddington Limit and Continuum-Driven Mass Loss

As developed in the previous sections, for the radiatively driven winds of hot stars with mass loss rates ranging up to $10^{-5} M_\odot/yr$, the central mechanism for coupling radiation to the outflowing gas is understood to be via *line* opacity, augmented through the systematic Doppler shift of the line-scattering by the velocity gradient associated with the flow acceleration. The inherently nonlinear feedback between the line driving and flow acceleration can be solved self-consistently via the CAK formalism and its modern extensions. In general, the resulting wind solutions are in remarkably good, quantitative agreement with observational inferences of key wind properties like the mass loss rate and wind flow speed, and with the scaling of these with stellar parameters like the luminosity and gravity.

However, at least some of the very most massive stars – observationally identified as the so-called Luminous Blue Variables (LBV's) – appear to undergo one or more phases of much stronger mass loss. Perhaps the most extreme example is the giant eruption of the massive LBV star Eta Carina, which is estimated to have cumulatively lost several $M_\odot$ between 1840-1860, representing a mass loss rate $> 0.1 M_\odot$/yr that is about a factor $10,000$ times greater than can be readily explained via the line-driven wind formalism. Instead, the observational association of these LBV's as being near an apparent upper limit in luminosity for observed stars has led to the general view that the strong mass loss may stem from the star approaching or exceeding the so-called "Eddington limit", at which even the *continuum* force associated with perhaps just electron scattering exceeds the inward force of gravity (see §4.2.1).

But a key difficulty in understanding how the approach or breach of the Eddington limit might lead to stellar mass loss lies in the fact that both the radiative acceleration and gravity have a similar inverse-square scaling with radius, implying that their ratio Γ_e (the so-called Eddington parameter – eqn. 4.4) has (in simple 1D models) a nearly spatially constant value throughout the star. As such, reaching or exceeding the Eddington limit $\Gamma_e \geq 1$ would appear to leave the entire star gravitationally unbound, and so does not constitute an appropriate description for steady-state, *surface* wind mass loss from an otherwise stably bound central star.

A promising solution to this difficulty lies in relaxing the usual assumption of strictly one-dimensional (1-D) spherically symmetric stratification, and considering how the lateral structuring – or "porosity"– of a medium could lead to an effective reduction in the coupling between the radiation and matter (Shaviv 1998, 2000). As we discuss in §8.3, this can, in principal, provide a way for quasi-stationary wind outflows to be maintained from objects that formally exceed the Eddington limit. But to provide a basis for this idea, let us first discuss some general consequences and issues in approaching or exceeding the Eddington limit.

8.1 "Photon Tiring" as a Fundamental Limit to Mass Loss

8.1.1 Line-Driven Winds near the Eddington Limit

As a star approaches the classical Eddington limit $\Gamma_e \to 1$, the standard CAK scalings predict the mass loss rate to diverge as $\dot{M} \sim 1/(1-\Gamma_e)^{(1-\alpha)/\alpha}$, but with a vanishing terminal flow speed $v_\infty \sim \sqrt{1-\Gamma_e}$. The former might appear to provide an explanation for the large mass losses inferred in LBV's, but the latter fails to explain the moderately high inferred ejection speeds, e.g. the 500-800 km/s kinematic expansion inferred for the Homonculus nebula of Eta Carina (Smith et al. 2003).

Moreover, of course, such a divergence of the mass loss rate is precluded by the finite energy available in the stellar luminosity L_*, which sets a so-called "photon-tiring" limit for lifting mass out of the gravitational potential of the stellar surface (Owocki and Gayley 1997)

$$\dot{M}_{tiring} = \frac{L_*}{v_{esc}^2/2} = \frac{L_*}{GM_*/R_*} = 0.032\ L_6\ \frac{R_*/M_*}{R_\odot/M_\odot}\,, \tag{8.1}$$

where $L_6 \equiv L_*/10^6 L_\odot$. Comparison with the CAK mass loss scaling of eqn. (4.31) shows that photon tiring would limit CAK winds whenever

$$1-\Gamma_e < \bar{Q}\Gamma_e \left[\frac{\alpha}{1-\alpha}\,\frac{2v_{esc}^2}{c^2}\right]^{\alpha/(1-\alpha)}\,. \tag{8.2}$$

For typical parameters $\bar{Q} \approx 2000$ and $2v_{esc}^2/c^2 \approx 10^{-5}$, we find that for $\alpha = 2/3$ photon tiring does not become important until the star is *very* close to the Eddington limit,

$$1-\Gamma_e < 2000\left[2\times 10^{-5}\right]^2 = 8\times 10^{-7}\ \ ;\ \ \alpha = 2/3\,. \tag{8.3}$$

However, for just a somewhat smaller CAK power index $\alpha = 1/2$, the condition is *much* less stringent,

$$1-\Gamma_e < 2000\left[10^{-5}\right] = 2\times 10^{-2}\ \ ;\ \ \alpha = 1/2\,. \tag{8.4}$$

This emphasizes that the CAK mass loss rate is extremely sensitive to the power index α, particularly near the Eddington limit, where the term within the square bracket in eqn. (4.31) has a large numerical value, which is then raised to a power that depends on α.

8.1.2 Photon Tiring in Continuum-Driven Mass Loss

Let us next examine photon tiring for continuum-driven flow, ignoring the effect of line-opacity, and simply considering that some outward increase in continuum opacity causes some layer to become super-Eddington. For simplicity, let us assume the Eddington parameter, $\Gamma(r)$, has a known, explicit spatial dependence, with

the initial radius $r = R_*$ at which Γ first exceeds unity corresponding to the sonic point of a supersonic mass outflow. The density ρ_* and sound speed a_* at this point set the mass loss rate $\dot{M} = 4\pi R_*^2 \rho_* a_*$, but otherwise gas pressure terms have negligible effect in the further supersonic acceleration of the outflow. The steady-state equation of motion thus reduces to

$$v\frac{dv}{dr} \approx -\frac{GM_*(1-\Gamma(r))}{r^2} \quad ; \quad r \geq R_*. \tag{8.5}$$

Note that in this form the mass loss rate itself has scaled out, so that the resulting velocity law would be entirely independent of the amount of mass accelerated. More realistically, as noted above, a given radiative luminosity can only accelerate a limited mass loss rate before the energy expended in accelerating the outflow against gravity would necessarily come at the expense of a notable reduction in the radiative energy flux itself. To take accout of this photon tiring, we simply reduce the radiative luminosity according to the gained kinetic and potential energy of the flow,

$$L(r) = L_* - \dot{M}\left[\frac{v^2}{2} + \frac{GM_*}{R_*} - \frac{GM_*}{r}\right]. \tag{8.6}$$

In terms of the scaled variables

$$w \equiv v^2 R_*/2GM_* \; ; \quad x \equiv 1 - R_*/r, \tag{8.7}$$

we find the equation of motion with photon tiring can be written in the dimensionless form,

$$\frac{dw}{dx} = -1 + \Gamma(x)[1 - m(w+x)], \tag{8.8}$$

where the photon "tiring number",

$$m \equiv \frac{\dot{M}}{\dot{M}_{tiring}} = \frac{\dot{M}GM_*}{L_* R_*} \approx 0.012\,\frac{\dot{M}_{-4} V_{1000}^2}{L_6}\,, \tag{8.9}$$

characterizes the fraction of radiative energy lost in lifting the wind out of the stellar gravitational potential from R_*. The last expression allows easy evaluation of the likely importance of photon tiring for characteristic scalings, where $\dot{M}_{-4} \equiv \dot{M}/10^{-4}\,M_\odot/yr$, $L_6 \equiv L_*/10^6\,L_\odot$, and $V_{1000} \equiv v_{esc}/1000\,km/s$.

Using integrating factors, it is possible to obtain an explicit solution to $w(x)$ in terms of the integral quantity $\bar{\Gamma}(x) \equiv \int_0^x dx'\Gamma(x')$,

$$w(x) = -x + \frac{1 - e^{-m\bar{\Gamma}(x)}}{m} + w_*, \tag{8.10}$$

where for typical hot-star atmospheres the sonic point boundary value is very small, $w(0) = w_* \equiv a_*^2 R_*/2GM_* < 10^{-3}$.

As a simple example, consider the case with $\Gamma(x) = 1 + \sqrt{x}$, for which $\bar{\Gamma} = x + 2x^{3/2}/3$. Figure 25 plots solutions $w(x)$ vs. x from eqn. (8.10) for various

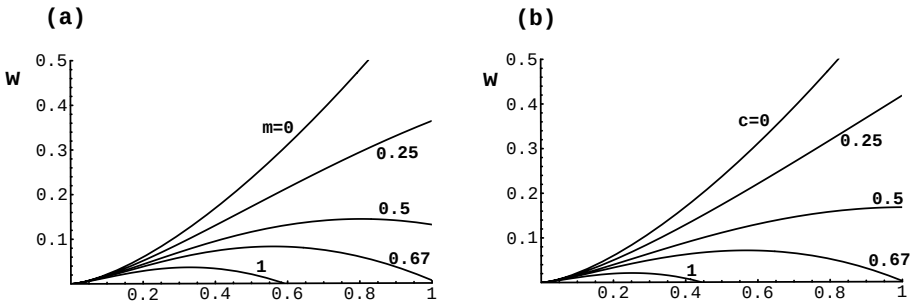

Fig. 25. a. Wind energy w vs. scaled inverse radius $x(\equiv 1-R_*/r)$, plotted for Eddington parameter $\Gamma(x) = 1 + \sqrt{x}$ with various photon tiring numbers m. b. Same as (a), except for weak tiring limit $m \ll 1$, and for various constants c in the Eddington parameter scaling $\Gamma(x) = 1 + \sqrt{x} - 2cx$.

m. For low m, the flow reaches a finite speed at large radii ($x = 1$), but for high m, it curves back, stopping at some finite *stagnation* point x_s, where $w(x_s) \equiv 0$. The latter solutions represent flows for which the mass loss rate is too high for the given stellar luminosity to be able to lift the material to full escape at large radii. By considering the critical case $w(x = 1) = 0$, we can define a maximum mass loss rate from m_{max}, given from eqn. (8.10) by the transcendental relation,

$$m_{max} = 1 - e^{-m_{max}\bar{\Gamma}(1)} \approx 1 - e^{2-2\bar{\Gamma}(1)}, \tag{8.11}$$

where the latter expression provides a good explicit approximation for any realistic $\bar{\Gamma}(1) > 1$. Note that regardless of how large $\bar{\Gamma}(1)$ becomes, it is always true that $m_{max} < 1$, simply reflecting the fact that the mass loss is always limited by the rate at which the radiative luminosity can lift material out of the gravitational potential from R_*.

Even without photon tiring, a similar stagnation can occur from an outward reduction in the radiative driving. In the limit of negligible tiring $m \ll 1$, the flow solution (8.10) simplifies to

$$w(x) \approx \bar{\Gamma}(x) - x. \tag{8.12}$$

For a limited super-Eddington domain, the critical case of marginal escape with zero terminal velocity, $w(1) = 0$, is now set in general by the condition $\bar{\Gamma}(1) = 1$. For example, consider the specific case of nonmonotonic $\Gamma(x) = 1 + \sqrt{x} - 2c\,x$, for which then $\bar{\Gamma}(x) = x + 2x^{3/2}/3 - cx^2$. Fig. 1b plots results for various c. For all $\bar{\Gamma}(1) < 1$ (i.e., $c > 2/3$), the material stagnates at the radius where $\bar{\Gamma}(x_s) = x_s = 4/9c^2$, and so cannot escape the system in a steady-state flow. In a time-dependent model, such material can be expected to accumulate at this stagnation radius, and possibly eventually fall back to the star.

8.2 Stellar Envelope Consequences of Breaching the Eddington Limit

8.2.1 Convective Instability of Deep Interior

It should be emphasized that locally exceeding the Eddington limit need *not* necessarily lead to initiation of a mass outflow. As first shown by Joss et al. (1973), in the deep stellar interior allowing $\Gamma \to 1$ generally implies that material becomes *convectively unstable*. Since convection in such deep layers is highly efficient, the radiative luminosity is reduced, thereby lowering the associated radiative Eddington factor away from unity. Indeed, even in the classical case of only electron scattering opacity, the Eddington parameter $\Gamma_e \sim L_*/M_*$ should increase inward because, while the luminosity is nearly constant outside a very compact nuclear generation core, the mass within the local radius $M(r)$ decreases inward. Thus, for example, if the luminosity and surface mass M_* imply a surface Eddington parameter $\Gamma_* \lesssim 1$, then the entire region interior to a mass fraction $M(r)/M_* = \Gamma_*$ should be convectively unstable!

Likewise, if an *outward* increase in the total effective opacity leads toward a super-Eddington condition in some region of the outer envelope, that region should also become convective. Again, as long as the convection is efficient, the net flux of radiative luminosity will be reduced so as to keep the total outward radiative force below the inward force of gravity. This suggests that a radiatively driven outflow should only be initiated *outside* the region where convection is efficient.

Using the simple "mixing length" formalism for convection, we can estimate an upper bound to the convective energy flux,

$$F_{conv} \approx v_{conv}\, l\, dU/dr \lesssim a\, H\, dP/dr \approx a^3 \rho, \tag{8.13}$$

where v_{conv}, l, and U are the convective velocity, mixing length, and internal energy density, and a, H, P, and ρ are the sound speed, pressure scale height, pressure, and mass density. Setting this maximum convective flux equal to the total stellar energy flux, $\rho a^3 = L_*/4\pi r^2$ yields an estimate for the maximum mass loss rate $\dot{M}_{max,conv} = 4\pi r^2 \rho a$ that could be initiated at the radius r where convection become inefficient,

$$\dot{M}_{max,conv} = \frac{L_*}{a^2} = \frac{v_{esc}^2}{2a^2}\dot{M}_{tiring}\,. \tag{8.14}$$

The latter equality emphasizes that, for the usual case of a sound speed much smaller than the local escape speed, $a \ll v_{esc}$, such a mass loss would generally be well in excess of the photon-tiring limit set by the energy available to lift the material out of the star's gravitational potential (see eqn. 8.1).

A central conclusion here is thus that, while convective transport provides an alternative to a super-Eddington condition in the deep interior, it by itself cannot be the regulation mechanism that would allow for a smooth transition to a steady wind mass loss of the near-surface layers.

8.2.2 Hydrostatic Pressure Inversion in a Super-Eddington Layer

Even above the efficient-convection radius, a *limited* super-Eddington domain could, instead of an outflow, merely induce a pressure inversion layer set by integrating the equation of hydrostatic equililbrium (cf. eqn. 2.1)

$$\frac{d\ln P}{dr} = \frac{\Gamma - 1}{H} \tag{8.15}$$

where $H \equiv a^2 r^2/GM_*$ is the usual gravitational scale height. As an example, for a narrow ($\Delta r \ll r$), isothermal, super-Eddington layer, the pressure would increase by a factor $\exp[(\Delta r/H)(\bar{\Gamma} - 1)]$, where $\bar{\Gamma}$ is the average of Γ over the layer. This exponential pressure increase implies, however, that such inversions are only possible over a limited domain, since eventually the star must match an outer boundary condition of negligible pressure.

Since more realistically the temperature should be expected to decline outward, such a pressure inversion would imply an even stronger outward increase in density. If the super-Eddington condition persists, then perhaps another switch to convective transport could again reduce the radiative flux, and bring the Eddington parameter back below unity. But again this should become inefficient at a layer that cannot maintain an outflow against photon tiring. This implies that any such outflow initiated from the region that convection becomes inefficient would necessarily stagnate at some finite radius. One can imagine that the subsequent infall of material would likely form a complex spatial pattern, consisting of a mixture of both downdrafts and upflows, perhaps even resembling the 3D cells of thermally driven convection. Overall, we thus see that a star that exceeds the Eddington limit is likely to develop a complex spatial structure, whether due to local instability to convection, or to global instability of flow stagnation.

8.2.3 Lateral Instability of Thomson Atmosphere

Dating back to early work by Spiegel (1976; 1977) there have speculations that atmosphere supported by radiation pressure would likely exhibit Rayleigh-Taylor-type instabilities associated with support of a heavy fluid by a lighter one, leading to formation of "photon bubbles". Recent quantitative stability analyses by Spiegel and Tao (1999) and by Shaviv (2001) do lead to the conclusion that even a simple case of a pure "Thomson atmosphere" – i.e. supported by Thomson scattering of radiation by free electron – would be subject to intrinsic instabilities for development of lateral inhomogeneities. The analysis by Shaviv (2001) suggests in particular that these instabilities share many similar properties to the excitation of strange mode pulsations (e.g., Glatzel 1994; Glatzel et al. 1999). For example, they are favored when radiation pressure dominates over gas pressure, in this case operating in an intermediate regime between purely adiabatic and isothermal limits for the energy transport, wherein radiation diffuses against the opacity that shields localized gas compressions. With the dominance of radiation pressure, there is a tendency for it to compress the gas further, leading to an

unstable growth of lateral structure. Shaviv (2001) identifies both stationary and propagating modes with maximum growth occurring at lateral scales comparable to the vertical scale height.

8.3 Super-Eddington Outflow Modulated by Porous Opacity

Shaviv (1998; 2000) has applied these notions of a laterally inhomogeneous radiatively supported atmosphere to suggest a new paradigm for how quasi-stationary wind outflows could be maintained from objects that formally exceed the Eddington limit. A key point regards the fact that, in a spatially inhomogeneous atmosphere, the radiative transport will selectively avoid regions of enhanced density in favor of relatively low-density, "porous" channels between them. This stands in contrast to the usual picture of simple 1D, gray-atmosphere models, wherein the requirements of radiative equilibrium ensure that the radiative flux must be maintained independent of the medium's optical thickness. In 2D or 3D porous media, even a gray opacity should lead to a flux avoidance of the most optically thick regions, much as in frequency-dependent radiative transfer in 1D atmosphere, wherein the flux avoids spectral lines or bound-free edges that represent a localized spectral regions of non-gray enhancement in opacity. The associated reduction in the effective opacity might thus provide a mechanism for the transition from an effectively sub-Eddington to super-Eddington condition, and perhaps thereby allow an appropriate regulation for steady wind mass loss of the outer layers.

8.3.1 A Simple Model for the Effective Opacity of a Porous/Clumped Medium

The radiative transport in such a complex, 3D medium is likely to be extremely complicated, but to model the basic elements of this porosity effect, let us consider the following simple picture of a medium consisting of an ensemble of localized "clumps" or "blobs". Assuming for now that the blobs all have the same characteristic length l and mass m_b, the characteristic blob density is roughly $\rho_b \approx m_b/l^3$. Then in a medium with opacity κ the characteristic blob optical depth is $\tau_b \approx \kappa\rho_b l$. If the blob is optically thick, $\tau_b \gg 1$, then the effective cross section of the blob to impingent radiation is just $\sigma_{eff} \approx l^2$. But more generally, since for arbitrary optical thickness the fraction of impingent radiation attenuated by the blob should scale as $1-\exp(-\tau_b)$, this effective cross section can be written as $\sigma_{eff} \approx l^2[1-\exp(-\tau_b)]$. From this, we can thus define an *effective opacity* of the blob as

$$\kappa_{eff} \equiv \frac{\sigma_{eff}}{m_b} \approx \frac{l^2}{m_b}[1-\exp(-\tau_b)] \approx \kappa\,\frac{1-\exp(-\tau_b)}{\tau_b}. \tag{8.16}$$

In the limit that the blob is optically thin, $\tau_b \ll 1$, this effective opacity recovers the microscopic value, $\kappa_{eff} \to \kappa$. However for an optically thick blob, $\tau_b \gg 1$, the opacity is effectively *reduced by a factor* $1/\tau_b$, i.e. $\kappa_{eff} \to \kappa/\tau_b \approx l^2/m_b$.

Let us now consider a medium that consists entirely of an ensemble of such blobs, with a characteristic separation scale $L \gg l$. Then the mean density of the

medium is given by $\rho \approx m_b/L^3 = (l/L)^3\rho_b$, and the blob optical thickness can be written as the ratio

$$\tau_b = \frac{\rho}{\rho_c} \tag{8.17}$$

where the critical medium density at which the blob has unit optical depth is given by

$$\rho_c \approx \frac{l^2}{\kappa L^3} \equiv \frac{1}{\kappa h}\,, \tag{8.18}$$

with the latter equality defining a characteristic "porosity length" $h \equiv L^3/l^2$.

As developed further below, this porosity length turns out to be a key parameter for determing the nature and consequences of the porosity in a structured medium. Physically, it represents the photon mean-free-path in the high-density limit $\rho \gg \rho_c$, for which the effective opacity of the medium κ_{eff} is reduced by a factor ρ_c/ρ. By contrast, in the low-density limit $\rho \ll \rho_c$, the effective opacity recovers its microscopic value $\kappa_{eff} \approx \kappa$.

8.3.2 A Porosity-Length Ansatz for Deriving Mass Loss Scaling

Let us now apply this simple picture of a porous medium to model the porosity-modulated mass loss of a super-Eddington atmosphere. Given a value of the Eddington parameter $\Gamma > 1$ derived from a microscopic continuum opacity κ, the reduced, effective Eddington parameter is simply given by

$$\Gamma_{eff} \approx \frac{\rho_c}{\rho}\Gamma\left(1 - e^{-\rho/\rho_c}\right)\,. \tag{8.19}$$

The reduction at large densities now allows a base hydrostatic region where $\Gamma_{eff} < 1$. Above this, a transonic wind can then be initiated at the point where $\Gamma_{eff} = 1$. When applied to eqn. (8.19), this can be used to solve implicitly for the sonic point density ρ_*.

For the highly superEddington limit $\Gamma \gg 1$, this sonic density solution takes the explicit form

$$\rho_* \approx \Gamma\rho_c = \frac{L_*}{4\pi G M_* c h} \quad ; \quad \Gamma \gg 1\,, \tag{8.20}$$

where the latter relation again uses the porosity length h. Given the atmospheric radius R_* and sound speed a_*, the associated mass loss rate is then

$$\dot{M}_{por} = 4\pi a_* R_*^2 \Gamma\rho_c = \frac{a_* L_*}{g_* c h} = \frac{L_*}{a_* c}\frac{H}{h} \quad : \quad \Gamma \gg 1\,, \tag{8.21}$$

where in the latter relations $g_* = GM_*/R_*$ is the surface gravity, and, as in eqn. (8.15), $H \equiv a_*^2/g_*$ represents a characteristic scale height for the atmosphere in the absence of any radiative forces.

To proceed, we must next define a scaling for the porosity length h. For this, let us consider an argument somewhat analogous to that traditionally given for representing convective energy transport in terms of a characteristic "mixing

length", which is generally assumed to scale in proportion the gravitional scale height H. Namely, let us assume that the atmospheric structure underlying the porosity arises (at least in part) from a failure to sustain the kind of pressure inversion described in eqn (8.15). On this basis, let us then make an analogous *ansatz* that the porosity length should scale with the *inverted* pressure scale length,

$$h \approx \frac{H}{\Gamma - 1} \,. \tag{8.22}$$

Application in eqn. (8.21) then yields for the highly[2] superEddington case $\Gamma \gg 1$.

$$\dot{M}_{por} \approx \frac{L_*}{a_* c} \, (\Gamma - 1) \approx 5.6 \times 10^{-4} \, \frac{M_\odot}{\rm yr} \, \frac{(\Gamma - 1) L_6}{\sqrt{T_5}} \,, \tag{8.23}$$

where $T_5 \equiv T_*/10^5 K$, and $L_6 \equiv L_*/10^6 L_\odot$.

It is of interest to contrast this with the CAK mass loss for line-driven winds, which from eqn. (4.31) has the scaling

$$\dot{M}_{CAK} = \frac{L_*}{c^2} \, \frac{\alpha}{1-\alpha} \left[\frac{\bar{Q} \Gamma_e}{1 - \Gamma_e} \right]^{\frac{1-\alpha}{\alpha}} = 1.6 \times 10^{-7} \, \frac{M_\odot}{\rm yr} \, L_6 \left[\frac{\bar{Q} \Gamma_e}{1 - \Gamma_e} \right]^{1/2} , \tag{8.24}$$

where the latter equality applies to the typical case that $\alpha = 2/3$. For the typical case $\bar{Q} \approx 2000$ and $\Gamma_e \approx 0.5$, we find $\dot{M}_{CAK} \approx 7.2 \times 10^{-6} L_6 M_\odot/{\rm yr}$.

Comparison with eqn. (8.23) shows that mass loss can be much larger for this continuum-driven model than for the line-driven case.

8.3.3 Photon Tiring of Porosity-Modulated Mass Loss

The porosity-modulated, continuum mass loss derived above can, in fact, readily approach the absolute upper limit associated with photon tiring. Dividing eqn. (8.23) by eqn. (8.1), we obtain the associated tiring number for the porosity-modulated mass loss rate

$$m_{por} \approx \frac{v_{esc}^2}{2 a_* c} \, (\Gamma - 1) \approx 0.018 \, \frac{M_*/R_*}{M_\odot/R_\odot} \, \frac{\Gamma - 1}{\sqrt{T_5}} \,. \tag{8.25}$$

This suggests that photon tiring should not have much effect for only moderately super-Eddington models, i.e. $\Gamma < 10$, but it should limit the effective mass loss in strongly super-Eddington cases, i.e. $\Gamma > 10$.

8.4 Gravity Darkening and the Shaping of LBV Nebulae

The most striking example of LBV giant outburst, the Homunculus nebula of eta Carina, exhibits a distinct *bipolar* form, with the polar flow having both a

[2]For the mildly superEddington case $\Gamma - 1 \ll 1$, the scaling in eqn. (8.23) is simply reduced by a factor $2(\Gamma - 1)/\Gamma$.

higher flow speed and greater density than the equatorial regions. Moreover, recent observations indicate that the present-day wind outflow, which is still estimated to have a very strong mass loss rate of order $10^{-3} M_\odot$/yr, is likewise faster and stronger over the poles. Direct VLT interferometric resolution of the optically thick wind shows that it too has a prolate shape, aligned along the same axis as the Homonculus (van Boekel et al. 2003). In HST slit spectra placed across the Homonculus nebula, the reflection from nebula dust shows that the stellar spectrum viewed from over the poles has stronger and broader wind absorption, indicating a denser, faster polar outflow (Smith et al. 2003). The reasons for this bipolar form in both the giant outburst and the present-day wind are unclear, but one possibility is that both are a consequence of a rapid, near-critical rotation of the source star.

As discussed in §7, in a rapidly rotating star, the outward centrifugal acceleration reduces the effective gravity near the equator. Since for a broad range of stellar wind driving mechanisms, the wind flow speed scales as the effective escape speed, this implies a slower wind from the equator, and a faster wind over the poles. Thus rapid rotation would explain the broader polar wind absorption seen in the HST slit spectra of the present day star. In addition, if the star had been likewise rapidly rotating during the 1840-60 epoch of the giant outburst, this would explain both the greater polar extension seen in the nebula, as well as the greater present-day nebula expansion speeds inferred from Doppler-shifted, nebular line-emission.

The inferred higher polar density can be likewise explained in terms of rapid rotation and radiative driving, if, as discussed in §7, one assumes the von Zeipel (1924) gravity-darkening law in which the stellar surface flux scales with the effective gravity (cf. eqn. 7.1)

$$F(\theta) \sim g_{eff}(\theta) \sim 1 - \Omega \sin^2 \theta \,, \tag{8.26}$$

where θ is the co-latitude and $\Omega = V_{rot}^2 R_*/GM_*$. For such a scaling, the effective Eddington parameter $\Gamma_{eff} \sim F(\theta)/g_{eff}(\theta)$ is *independent* of latitude. But as discussed in §7 and shown in eqn. (7.4), for line-driven winds, the additional dependence of the mass flux with radiative flux means the surface mass flux likewise scales as

$$\dot{m}(\theta) \sim F(\theta) \sim 1 - \Omega \sin^2 \theta \,. \tag{8.27}$$

This line-driven scaling for mass loss loss has indeed been invoked as a way to explain the high polar density of the Homonculus nebula (Owocki and Gayley 1997; Maeder and Meynet 2000; Dwarkadas and Owocki 2002). But, as noted above, it doubtful that line-driving could explain even the strong ($10^{-3} M_\odot$/yr) mass loss of the present-day wind, let alone the huge mass loss ($> 0.1 M_\odot$/yr) associated with the giant outburst.

Fortunately, the above analysis for porosity-modulated *continuum* driving shows that the resulting mass loss should again scale with the stellar luminosity (eqn. 8.23). For a rotating star, this again implies a surface mass flux that scales with local radiative flux, as given in eqn. (8.27).

Thus, if the source star both today and during the giant eruption were rapidly rotating with a von Zeipel (1924) distribution of surface flux with effective gravity, then a model based on porosity-modulated, continuum-driven mass loss seems capable of explaining the faster, denser polar outflow inferred for the both the giant eruption and the present-day wind.

8.5 Summary for super-Eddington, Continuum-Driven Mass Loss

- The formal divergence of CAK mass loss as a star approaches the Eddington limit would in fact be limited by the "photon tiring" effect by which the energy required to lift this mass loss out of the gravitational potential reduces the radiative luminosity. For CAK exponent $\alpha = 1/2$, this limit would apply already within a couple percent of the Eddington limit ($\Gamma - 1 < 0.02$).

- Simple 1D, steady analyses of continuum driven mass loss shows that including photon tiring can slow or even stagnate the wind outflow if the wind mass loss approaches the tiring limit. For stagnated flows, time-dependent reaccretion seems likely.

- In the deep stellar interior, approaching the Eddington limit should lead to convective instability, with convection then carrying a sufficient fraction of the total energy flux to keep the radiative flux below the local Eddinton limit.

- In the near-surface layers where convection first becomes inefficient, the density is still so high that initiating a radiatively driven outflow would imply a mass loss rate that exceeds the tiring limit by a large factor ($v_{esc}^2/2a^2$).

- A super-Eddington domain could instead lead to a pressure or density inversion, but unless the domain has a limited range, this inversion must break down, since it can't match the outer boundary requirement of low density and pressure.

- This and other instabilities seem likely to induce complex, 3D density and velocity structure in the atmosphere of a star that approaches or exceeds the Eddington limit.

- Such complex structure can lead to a relative "porosity" of the medium that reduces the effective radiative force in regions where individual clumps become optically thick.

- In a super-Eddington case, the effective Eddington factor thus can now go from below unity in a dense, quasi-static base atmosphere, to exceeding unity in some outflowing layer where the clumps have become optically thin and thus are subject to the full driving.

- A key parameter for this effect is the "porosity length" h, representing the scale of the clumps divided their volume filling factor.

- In lieu of detailed modelling of the 3D structure, a possible ansatz – somewhat analogous to the "mixing length" formalism for convective energy transpor – is to presume this porosity length to be given by the inverse pressure scale height of a hydrostatic, super-Eddington layer [$h = H/(\Gamma - 1)$].

- Within this "porosity-length-ansatz", the porosity-modulated mass loss is found to scale as $\dot{M} \approx (L_*/ac)(\Gamma - 1)$, which substantially exceeds the CAK mass loss for line-driving, and can be a few percent or higher of the tiring limit value.

- The direct scaling of mass flux with radiative flux implies that, as in line-driving, porosity-modulated continuum driving leads to a higher polar mass flux from rapidly rotating stars with von Zeipel gravity darkening.

- Together with the generally expected scaling of the wind flow speed with the effective (centrifugally reduced) gravitational escape speed, this rotational scaling of mass flux provides an attractive explanation for the inferred bipolar form of both the present-day wind and the giant eruption of the LBV star eta Carina, for which the density and flow speed are inferred to be higher along the apparent polar axis.

References

Abbott, D.C. 1980, ApJ, 242, 1183.

Abbott, D.C. 1982, ApJ, 259, 282.

Bjorkman, J.E., and Cassinelli, J. 1993, ApJ, 409, 429.

Carlberg, R.G. ApJ, 241, 1131.

Castor, J.I., Abbott, D.C., and Klein, R. 1975, ApJ, 195, 157.

Cox, D.P. and Tucker, W.H. 1969, ApJ, 157, 1157.

Cranmer, S.R. *et al.* 1999, ApJ, 511, 481.

Cranmer, S.R. 2000, ApJ, 532, 1197.

Cranmer, S.R. and Owocki, S.P., ApJ, 440, 308.

Dessart, L. and Owocki, S.P. 2003, ApJ, 406, 1.

Dwarkadas, V., and Owocki, S.P. 2002, ApJ, 581, 1337.

Feldmeier, A. 1995, A&A, 299, 523.

Feldmeier, A. and Shlosman, I. 2000, ApJ, 532, 125.

Feldmeier, A. and Shlosman, I. 2002, ApJ, 564, 385.

Feldmeier, A., Puls, J., and Pauldrach, A. 1997, A&A, 322, 878.

Friend, D.B. and Abbott, D.C. 1986, 311, 701.

Friend, D.B. and Castor, J.C. 1983, 272, 259.

Gayley, K.G. 1995, ApJ, 454, 410.

Gayley, K.G., Owocki, S.P., and Cranmer, S.R. 1995, ApJ, 442, 296.

Glatzel, W. 1994, MNRAS, 271, 66.

Glatzel, W. 1999, MNRAS, 303, 116.

Grinin, A. 1978, Soviet Astron., 14, 113.

Hamman, W.R., Koesterke, L., and Wessolowski, U. 1995, A&A, 299, 151.

Joss, P.C., Salpeter, E.E., and Ostriker, J.E. 1973, ApJ, 181, 429.

Kohl, J.L., Esser, R., Cranmer, S.R., Fineschi, S., Gardner, L.D., Panasyuk, A.V., Strachan, L., Suleman, R.M., Frazin, R.A., and Noci, G. 1999, ApJ, 510, L59.

Lamers, H.J.G.L.M., and Cassinelli, J. 1999, *Introduction to Stellar Winds*, Cambridge University Press: Cambridge, New York.

Lamers,H.J.G.L.M., and Pauldrach,A.W.A. 1991, A&A, 244, L5.

Leer, E., Hansteen, V., and Holzer, T.E. 1998, in "Cyclical Variability in Stellar Winds", L. Kaper and A. Fullerton, eds., Springer-Berlin.

Leer, E. and Holzer, T.E. 1979, Solar Phys., 63, 143.

Lucy, L.B., and Solomon, P.M. 1970, ApJ, 159, 879.

Lucy, L.B. 1984, 284, 351.

MacGregor, K.B., Hartmann, L., and Raymond, J.C. 1979, ApJ, 231, 514.

Maeder, A. and Meynet, G. 2000, ARA&A, 38, 143.

Mihalas, D. 1978, *Stellar Atmospheres*, Freeman.

Owocki, S.P., , Cranmer, S.R, Gayley, K.G., 1996, ApJ, 472, L115.

Owocki, S.P. and Gayley, K.G. 1997, in *Luminous Blue Variables: Massive Stars in Transition*, ASP Conf. Ser. Vol. 120, A. Nota and H. Lamers, eds.

Owocki, S.P., Cranmer, S.R., and Blondin, J. 1994, ApJ, 424, 887.

Owocki, S.P. and Rybicki, G.B. 1984, ApJ, 284, 337.

Owocki, S.P. and Rybicki, G.B. 1985, ApJ, 299, 265.

Pauldrach, A.W.A., Puls, J., and Kudritzki, R.P. 1986, A&A, 164, 86.

Puls, J., Kudritzki, R.P., Herrero, A., Pauldrach, A.W.A., Haser, S.M., Lennon, D.J., Gabler, R., Voels, S., Vilchez, J.M., and Feldmeier, A. 1996, A&A, 305, 171.

Raymond, J.C., Cox, D.P., and Smith, B.W. 1976, ApJ, 204, 290.

Runacres, M.C. and Owocki, S.P. 2002, A&A, 381, 1015.

Rybicki, G.B., Owocki, S.P., and Castor, J.I. 1990, ApJ, 349, 274.

Shaviv, N. 1998, ApJ, 494, 193.

Shaviv, N. 2000, ApJ, 531, L137.

Shaviv, N. 2001, MNRAS, 326, 126.

Smith, N., Davidson, K., Gull, T.R., Ishibashi, K., Hillier, D.J. 2003, ApJ, 586, 432.

Sobolev, V.V. 1960, *Moving Envelopes of Stars*, Cambridge: Harvard Univ. Press.

Spiegel, E. 1976, in *Physique des Mouvement dans les Atmospheres Stellaires*, (Paris: CNRS), R. Cayrel & M. Steinberg, eds., p. 267.

Spiegel, E. 1976, in *Problems in Stellar Convection*, (Berlin: Springer), E. Spiegel & J.-P. Zahn, eds., p. 19.

Spiegel, E., and Tao, L. 1999, Phys. Rep. 311, 163.

vanBoekel,R., Kervella,P., Schoeller,M., Herbst,T., Brandner,W., deKoter,A., Waters,L., Hillier,D.J., Paresce,F., Lenzen,R., Lagrange,A.-M. 2003, A & A, 410, L37.

Vishniac, E.T. 1994, ApJ, 428, 186.

von Zeipel, H. 1924, MNRAS, 84, 665.